universität wien

MASTERARBEIT / MASTER'S THESIS

Titel der Masterarbeit / Title of the Master's Thesis

Comparative investigations on superconducting order parameter fluctuations in superconducting thin films and superconductor/ferromagnet bilayers

verfasst von / submitted by

Bernd Aichner, BSc

angestrebter akademischer Grad / in partial fulfilment of the requirements for the degree of

Master of Science (MSc)

Wien, 2016 / Vienna, 2016

Studienkennzahl lt. Studienblatt / degree programme code as it appears on the student record sheet:	A 066 876
Studienrichtung lt. Studienblatt / degree programme as it appears on the student record sheet:	Masterstudium Physik
Betreut von / Supervisor:	ao. Univ.-Prof. Dr. Wolfgang Lang

Abstract

In this thesis thin superconducting films and bilayers consisting of a superconducting and a ferromagnetic film were examined. The aim was to determine the influence of the ferromagnetic layer on the electronic transport properties of the superconducting films. Samples were fabricated of the superconducting materials NbN and NbTiN and the weak ferromagnetic alloy NiCu. The preparation of these samples was not part of the current work, but was done by the group around Wojciech Słysz at the Institute of Electron Technology (*Instytut Technologii Elektronowej*) at Warszawa, Poland.
For determining the electronic transport properties, measurements of the electrical resistance were carried out at various temperatures between 4.2 K and room temperature and at magnetic fields up to 1 T. With these measurements an analysis of the superconducting order-parameter fluctuations above the superconducting transition temperature was performed. Moreover current-voltage-characteristics of the samples were registered, which were then used to determine the superconducting critical current density. The sample geometry was measured in the scanning electron microscope.
The measurement results show distinct differences between the behaviour of superconductor/ferromagnet bilayers and that of superconducting films. The most prominent feature is a significant deviation of the fluctuations in NbTiN/NiCu bilayers from the common theory for fluctuation analysis. Furthermore, for NbN an enhanced critical current density was observed in superconductor/ferromagnet bilayers relative to plain superconducting films. This effect was also reported from other groups and can be important for the application of this material in superconducting single photon detectors.

Zusammenfassung

In der vorliegenden Masterarbeit wurden dünne Filme aus Supraleitern und Doppelschichten von supraleitenden und ferromagnetischen Filmen untersucht. Es ging dabei in erster Linie darum, den Einfluss der ferromagnetischen Schicht auf die elektronischen Transporteigenschaften der supraleitenden Filme zu analysieren. Als supraleitende Materialien wurden NbN und NbTiN, als Ferromagnet wurde eine NiCu-Legierung verwendet. Die Herstellung der Proben war nicht Teil dieser Arbeit, sondern wurde von der Gruppe um Wojciech Słysz am *Instytut Technologii Elektronowej* in Warschau übernommen.
Zur Untersuchung der elektronischen Transporteigenschaften wurden Messungen des elektrischen Widerstands bei verschiedenen Temperaturen im Bereich zwischen 4.2 K und Raumtemperatur und in Magnetfeldern bis zu 1 T durchgeführt. Anhand der so gewonenen Messdaten wurde eine Analyse der supraleitenden Fluktuationen oberhalb der Sprungtemperatur durchgeführt. Außerdem wurden Strom-Spannungs-Kennlinien der Proben aufgenommen, aus denen dann die kritische Stromdichte ermittelt wurde. Die Bestimmung der Probengeometrie erfolgte anhand von Aufnahmen mit dem Raster-Elektronenmikroskop.
Die Messergebnisse zeigen deutliche Unterschiede im Verhalten der Supraleiter/Ferromagnet-Heterostrukturen im Vergleich zu dem supraleitender Filme auf. Dabei sticht ein Abweichen der Fluktuationen in NbTiN/NiCu von der gängigen Theorie zur Fluktuationsanalyse hervor. Außerdem wurde für NbN beobachtet, dass die Proben, die mit einer ferromagnetischen NiCu Schicht bedeckt sind, eine höhere kritische Stromdichte aufweisen. Dieser Effekt ist auch von anderen Gruppen beobachtet worden und kann wichtig für die Anwendung dieses Materials in supraleitenden Einzel-Photon-Detektoren sein.

Danksagung

In erster Linie möchte ich Prof. Wolfgang Lang danken, dass er mir die Möglichkeit gegeben hat in seiner Gruppe mitzuarbeiten und so die vorliegende Masterarbeit zu verfassen, vor allem aber für seine Geduld und die gute Betreuung. Überdies auch dafür, dass er es mir ermöglicht hat, meine Ergebnisse beim Workshop "Novel materials and superconductors" in Obertraun zu präsentieren.
Dr. Wojciech Słysz und seinen Mitarbeitern am *Instytut Technologii Elektronowej* in Warschau danke ich für die Herstellung der Proben, Prof. Roman Sobolewski (University of Rochester) für seine Organisationstätigkeit und Unterstützung.
Prof. A. Bouzdine (Universié de Bordeaux) und Prof. A. Varlamov (Università di Roma "Tor Vergata") möchte ich für ihre Ideen danken, die bei der Auswertung der Messdaten sehr geholfen haben.
Meinen Labor-KollegInnen Georg Zechner, Johannes Kampmüller und Rita Mühlgassner gilt ein großes Dankeschön für die gute Zusammenarbeit. Allen voran möchte ich mich bei Georg Zechner bedanken, der mich in die Arbeit im Labor eingeführt hat und mir immer mit Rat und Tat zur Seite gestanden ist. Das gute Klima im Labor und die große Hilfsbereitschaft meiner Kollegen haben wesentlich zum Gelingen der Arbeit beigetragen.
Dr. Stephan Puchegger danke ich dafür, dass er Bilder meiner Proben im Raster-Elektronenmikroskop aufgenommen hat.
Ein besonderer Dank gilt Alexander Müllner, der seine Freizeit geopfert hat, um meine Masterarbeit Korrektur zu lesen. Er und Christoph Tietz haben es immer wieder geschafft, mit interessanten Gesprächen Abwechslung in den Uni-Alltag zu bringen.
Last, but not least möchte ich meinen Eltern ein großes Dankeschön aussprechen, dafür, dass sie mein Studium ermöglicht und mich immer in allen meinen Vorhaben unterstützt haben.

Contents

1 Superconductivity

1.1 Superconductivity - general considerations

Superconductivity is a phenomenon which is characterized by two main properties: Zero-resistance (1) and the expulsion of magnetic fields (2).

(1) **Zero-resistance:** The phenomenon of zero-resistance was first discovered by Heike Kamerlingh Onnes in mercury in 1911 [1].
When a superconducting material is cooled down, there is a sharp drop in resistivity at a certain temperature, called the critical temperature (T_c), which is specific for the superconducting material. At this temperature the material shows a phase transition into the superconducting state. In this state the superconductor is an ideal conductor, which means that it can transport current without losses (on condition that the current and the surrounding magnetic field is low).

(2) **Expulsion of magnetic fields:** An ideal (type I-) superconductor expels all magnetic fields. There is no field inside the superconductor, therefore a superconductor shows ideal diamagnetism and has a magnetic susceptibility $\chi = -1$. When the superconductor is in the normal state, it has no special properties regarding the magnetic field, it only expels it when it becomes superconducting. The expulsion of the magnetic field is independent on whether the superconductor is field-cooled (it changes into the superconducting state while it is penetrated by a magnetic field) or if the field is applied when it is already superconducting. The field-expulsion is not a consequence of the infinite conductivity but is a separate effect. This effect was discovered by Walther Meissner and Robert Ochsenfeld [2] and is therefore called the Meissner-Ochsenfeld-effect.

A material has to show both effects (1 and 2) to be considered a superconductor. Superconductivity is not a rare phenomenon; many elements become superconducting at low temperatures, so do a lot of alloys. The transition temperature of the elements is mostly quite low, from sub-Kelvin range to some Kelvin (for further information see for example reference [3], page 7).

1.2 Theories describing superconductivity

- **London theory:** Fritz and Heinz London developed a mathematical description of the superconducting state based on classical electrodynamic theory [4]. Two equations are used to phenomenologically characterize the superconducting state:

$$\frac{\partial}{\partial t}\vec{j} = \frac{1}{\mu_0 \lambda_L^2}\vec{E} \quad 1^{\text{st}} \text{ London equation} \tag{1}$$

$$\text{rot}(\vec{j}) = -\frac{1}{\mu_0 \lambda_L^2}\vec{B} \quad 2^{\text{nd}} \text{ London equation} \tag{2}$$

$\vec{j}$ is the current density, $\vec{E}$ is the electric and $\vec{B}$ the magnetic field, μ_0 denotes the vacuum permeability and λ_L the London penetration depth.
These two equations allow to calculate properties of superconducting systems, but they do not describe correctly all phenomena and they do not give an explanation for superconductivity. The parameter

$$\lambda_L = \sqrt{\frac{m_s}{\mu_0 n_s q_s^2}} \tag{3}$$

was introduced. m_s and q_s are the mass and the charge of a superconducting carrier, respectively, and n_s is the density of superconducting carriers. Only after the development of BCS theory it was clear that one superconducting carrier consists of two

electrons and thus $m_s = 2m$, $q_s = 2e$ and $n_s = n/2$ with m and e the free electron mass and charge and n_e the number of electrons. Note that the factor 2 cancels out in the London penetration depth.
λ_L is a material-specific parameter, which depends on the temperature. A physical interpretation of the London penetration depth can be given concerning a bulk superconductor in an external magnetic field. As described in the previous section, the superconductor is field-free deep inside, but the field does not stop abruptly at the surface of the superconductor, but it decays in a small region under it's surface. The London penetration depth now denotes the depth, at which the magnetic field $B(x)$ has dropped to $1/e$ (with Euler's constant e) of it's value at the surface $B(x = 0)$.

$$B(x = \lambda_L) = \frac{1}{e} B(x = 0) \tag{4}$$

In this region under the surface superconductivity is not fully established and the density of superconducting charge carriers n_s grows with the depth. Moreover this is the only region where a super-current can flow; inside the superconductor the existence of a current is prohibited because a current (according to Maxwell's equations) always causes magnetic fields.

- **Ginzburg-Landau (GL) theory:** GL theory gives a macroscopic description of superconductivity by energetic considerations. It can be seen in the way that at certain conditions the transition into the superconducting state leads to a energetically favourable state. A complex wave-function $\Psi(x)$ is introduced, which describes the density of superconducting carriers $n_s = \|\Psi\|^2$ [5]).
In contrast to London theory it allows to consider boundaries between superconductors and other materials. This leads to the second characteristic length-scale of GL theory (the first one is the London penetration depth λ_L): the GL coherence length ξ_{GL}.

$$\xi_{GL} = \sqrt{\frac{\hbar^2}{2m_s|\alpha|}} \tag{5}$$

It gives the minimal length-scale at which the carrier density n_s can change and thus prevents a discontinuity in Ψ caused by a sudden drop of n_s at the surface of a superconductor. Like λ_L it depends on the material and on the temperature. α denotes the condensation-energy per Cooper-pair.
However GL theory is only valid near T_c. It can be deduced from the microscopic BCS theory for this range in the vicinity of the transition temperature [6].

- **BCS-theory:** The abbreviation BCS stands for the names Bardeen, Cooper and Shrieffer, the three scientists, who developed this microscopic theory of superconductivity [7, 8]. In BCS theory the superconducting charge transport is explained by the existence of a new type of charge carriers, the so called Cooper-pairs. A Cooper-pair is built by the pairing of two electrons with opposite spin by electron-phonon interaction. It therefore has twice the mass and twice the charge of an electron. Since Cooper-pairs are bosons they are not subject to the Pauli exclusion principle.
BCS theory gives a microscopic explanation of superconductivity in classical superconductors and has many experimental proofs.

1.3 Critical temperature, critical field and critical current

In a superconductor, superconductivity can be destroyed by rising one of the three parameters temperatur T, magnetic field B or current I beyond it's critical value T_c, B_c or I_c, respectively.

1.3.1 The critical temperature T_c

The critical temperature is the temperature, below which the material becomes superconducting. It does not only depend on the elements, of which the superconducting material is constituted, but also on the crystal structure. A wide range of alloys with transition temperatures of some Kelvin exists.
A special group of superconductors, the high-temperature superconductors, were found by Bednorz and Müller in 1986 [9]. As high temperatures in this context we denote temperatures above the boiling point of liquid nitrogen at ambient pressure.

1.3.2 The critical (magnetic) field B_c

As mentioned in section 1.1, bulk materials in the superconducting state are field-free deep inside, but the field can enter a certain distance below the surface, which is characterized by the London penetration depth λ_L. However, this is only true for some materials, for most of them the situation is more complex. Using the two superconducting material's parameters λ_L and ξ_{GL}, it is possible to define the GL parameter $\kappa = \lambda_L/\xi_{GL}$ and to differentiate between two classes of superconducting materials:

$$\begin{aligned} \kappa = \frac{\lambda_L}{\xi_{GL}} < \frac{1}{\sqrt{2}} \quad &\Longleftrightarrow \quad \text{Type I superconductor} \\ \kappa = \frac{\lambda_L}{\xi_{GL}} > \frac{1}{\sqrt{2}} \quad &\Longleftrightarrow \quad \text{Type II superconductor} \end{aligned} \tag{6}$$

This differentiation can be deduced in the framework of GL theory and is based on deliberations concerning energy. For a motivation of the factor $1/\sqrt{2}$ see chapter 13.4.4 of reference [10]. Type I- and type II superconductors show a fundamentally different behaviour in magnetic fields.

- As mentioned in section 1.1, a **type I superconductor** expels the magnetic field. In order to do this a boundary layer under the superconductor's surface has to be established. Naturally energy is needed to expel the field. At a specific field B_c superconductivity breaks down, the material becomes normal-conducting and the magnetic field goes through it.

- The situation in **type II superconductors** is totally different. The magnetic field is expelled in the so-called Meissner-phase up to a critical field B_{c1}, then the field penetrates into the superconductor in quantized form, in the form of flux-tubes, the so called vortices. This state with vortices in the superconductor is called the Shubnikov-phase. Each vortex carries the same magnetic flux, one flux-quantum

  $$\Phi_0 = \frac{h}{2e} \tag{7}$$

  with h the Planck-constant and e the electron charge. Inside these vortices the magnetic flux exists and the material is normal-conducting. The single vortices repel each other and are therefore arranged in a pattern, which provides the maximum possible distance between them (in clean superconductors). Since each vortex carries the same flux, with rising magnetic field the number of vortices increases and the fraction of superconducting area decreases. At a second specific field B_{c2} the entire volume is occupied by

vortices and superconductivity is destroyed in the whole specimen. Therefore in type II superconductors we have an additional state in respect to type I superconductors, which is characterized by the existence of magnetic vortices in the superconducting material.
If current flows through the superconductor, when it is in the Shubnikov-phase, Lorentz-force acts on the vortices and accelerates them. If the vortices move through the superconducting material, superconductivity has to be destroyed before and re-established behind them. Vortex-motion thus leads to energy dissipation and can cause the loss of superconductivity. Therefore it is a main goal for the development of superconducting materials to prohibit vortex-motion. This can be done by inserting defects as so-called pinning-centres into the superconducting material. Then the vortices can be bound at these pinning-centres and energy is needed to unbind them. This leads to the possibility that type-II superconductors in the Shubnikov-phase can carry a supercurrent without losses. Superconducting materials with defects for vortex-pinning are called hard superconductors.

1.3.3 The critical current

The critical current in type-I superconductors is the current at which superconductivity is destroyed. Thanks to Maxwell's equations each current can be associated with a magnetic field. Silbee's rule states that the critical current I_c is exactly the current which generates the critical field B_c. For type-II superconductors the situation is more complicated: There exists a critical current for vortex-entry, a critical current for the de-pinning of vortices (which leads to losses because of vortex-motion) and a depairing critical current (at which the Cooper-pairs are broken apart).

Furthermore, the three critical quantities depend on each other. One can imagine that each of them contributes to the superconductor's free energy and when this energy exceeds some specific value, superconductivity is destroyed. For example T_c for a given material is lower if a magnetic field is applied. The other way round, B_c and I_c are lower, the higher the temperature is and reach zero at $T = T_c$. The temperature-dependence of the magnetic field can be calculated by the empiric formula 8 (formula 13.1.9 at page 771 of [10]) with $B(0)$ the magnetic field at zero temperature.

$$B(T) = B(0)\left[1 - \left(\frac{T}{T_c}\right)^2\right] \tag{8}$$

The temperature dependence of the depairing critical current density in the vicinity of T_c is given by GL theory. Moreover two phenomenological functions for the critical current density found by Bardeen [11] shall be given here (equations 9).

$$\begin{aligned} j_{C-GL}(T) &= j_{c,0}\left(1 - \frac{T}{T_c}\right)^{3/2} && \text{(GL-theory)} \\ j_{C-B1}(T) &= j_{c,0}\left[1 - \left(\frac{T}{T_c}\right)^2\right]^{3/2} && \text{(Bardeen I)} \\ j_{C-B2}(T) &= j_{c,0}\left[1 - \left(\frac{T}{T_c}\right)^2\right]^{3/2}\left[1 + \left(\frac{T}{T_c}\right)^2\right]^{1/2} && \text{(Bardeen II)} \end{aligned} \tag{9}$$

All three equations have been taken from [12], for simplicity reasons the pre-factors of all three equations have been replaced by $j_{c,0}$. Note that in reality there can be different pre-factors. For a profound discussion of the temperature dependence of the depairing critical current, see the mentioned article.

1.4 The proximity effect

The proximity effect occours when a superconducting film is brought in contact with a normal conductor. The contact leads to a diffusion of superconducting carriers into the normal conductor, where they are then transformed into normal conducting electrons at a certain action depth. This causes a reduction of the superconducting transition temperature. An experimental evidence was found for example by P. Hilsch in Pb/Cu sandwiches, for which he showed that T_c decreases with increasing thickness of the metal layer up to a certain value [13].

1.5 The superconducting materials NbN and NbTiN

NbN and NbTiN are both classical superconductors. For NbN single-crystal films (thickness: 120 nm) transition temperatures above 16 K, normal-state resistivities (at 20 K) from 12.2 to 14.3 $\mu\Omega$cm and values of the superconducting coherence length $\xi_{GL}(0)$ of ≈ 7 nm have been reported [14]. For NbTiN, T. Matsunaga et al. found for example T_c as high as 15 K and a resistivity of about 100 $\mu\Omega$cm at 20 K for 200 nm thick films [15].
From a structural point of view, NbN and NbTiN are very similar, both have a NaCl structure, which is a face-centred-cubic (fcc) structure with a two-atomic base (see figure 1). The basis consists of one atom with the coordinates (0,0,0) and one with the coordinates $(\frac{1}{2},\frac{1}{2},\frac{1}{2})$.
For both materials the N atoms are at the position $(\frac{1}{2},\frac{1}{2},\frac{1}{2})$. For NbN the atoms with the coordinates (0,0,0) are Nb atoms and for NbTiN 80% of (0,0,0) locations are occupied by Nb and to 20 % by Ti atoms. All the structural data (also for creating figure 1) have been taken from *Springer Materials*' website (reference [16] for NbN and [17] for NbTiN).

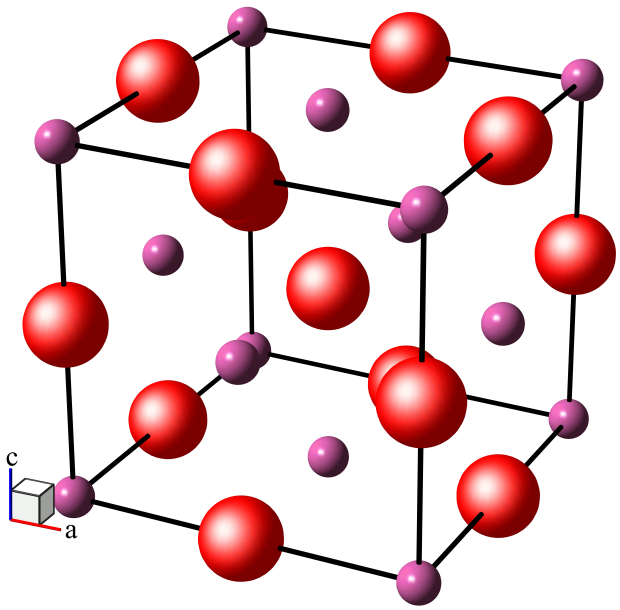

Figure 1: Crystal structure of NbN and NbTiN. It is a face-centered cubic structure with a two-atomic basis where one atom has the coordinates (0,0,0) (purple) and the other has the coordinates $(\frac{1}{2},\frac{1}{2},\frac{1}{2})$ (red). The image was created with the program *Balls & Sticks*[18].

2 Fluctuations

In chapter 1.1 the superconducting transition temperature T_c was introduced as the temperature, at which the phase-transition into the superconducting phase occurs. In the simplest model the material is normal-conducting above and superconducting below T_c. In reality the situation is more complex. To understand this, one has to consider that temperature is defined as a medium value in a big ensemble of particles. In this ensemble some regions with higher and others with lower temperature exist. If the temperature (the medium value) is chosen right above the superconducting transition temperature, for short time-spans there exist regions which have lower temperature and thus become superconducting. On the other hand there also exist normal-conducting regions below T_c [19].
These superconducting regions above T_c, which cannot be described in the frame of equilibrium physics, are called fluctuations[1]. Although they disappear after a short time-span, they have a contribution to the conductivity, the so-called paraconductivity and they increase the magnetic susceptibility above T_c.
Since fluctuations provide superconducting regions above and normal-conducting ones below T_c, they lead to a broadening of the superconducting transition.
The role of fluctuations is small in bulk metallic superconductors, but paraconductivity can be seen in superconducting samples with reduced dimensionality [21]. Fluctuation effects are more pronounced in high-temperature-superconductors than in classical superconductors, because these materials have a layered structure and a small GL-coherence-length ξ_{GL}.
Since fluctuations do not depend on the absolute temperature, but on the temperature relative to T_c, it is common to use the reduced temperature ϵ.

$$\epsilon = \ln\left(\frac{T}{T_c}\right) \approx \frac{T - T_c}{T_c} \tag{10}$$

2.1 Paraconductivity

Paraconductivity is the excess conductivity, caused by fluctuations above the superconducting transition temperature. The conductivity σ of a superconductor above T_c can therefore be expressed as

$$\sigma = \sigma_n + \Delta\sigma \tag{11}$$

where σ_n denotes the normal-state-conductivity and $\Delta\sigma$ is the fluctuation paraconductivity. In the following, theories, which describe this fluctuation contribution, are presented.

The Aslamazov-Larkin (AL) contribution: In 1968 L. G. Aslamazov and A. I. Larkin found a theory, which describes the contribution of the fluctuation pairs in thin films [22]. They derived their formula in the framework of BCS theory, but the same result was obtained with the GL approach [23]. The fluctuation paraconductivity for one-, two- and three-dimensional structures is given by the following formulae:

$$\Delta\sigma^{AL}_{1\mathrm{D}} = \frac{\pi e^2 \xi}{16\hbar d w \epsilon^{3/2}} \tag{12}$$

$$\Delta\sigma^{AL}_{2\mathrm{D}} = \frac{e^2}{16 d \hbar \epsilon} \tag{13}$$

$$\Delta\sigma^{AL}_{3\mathrm{D}} = \frac{e^2}{32\hbar\xi\epsilon^{1/2}} \tag{14}$$

e denotes the elementary charge and $\hbar$ the reduced Planck-constant, ξ is the GL coherence length at zero temperature, d and w are thickness and width of the film.
It is interesting to note that the coherence length ξ is the only material's constant in these

[1] For a detailed discussion of fluctuations in superconductors see for example reference [20].

equations and that the equation for the 2D-case is totally parameter-free. Moreover one can see that for 2D the film thickness and for 1D thickness and width do not have any influence on evaluation of measurement data because d and b in the formulae cancel out with the parameters used to calculate the resistivity or the specific conductance. Figure 2 shows a comparison of the three formulae given in equation 13 for arbitrary values of d, w and ξ. One can see that the additional conductivity provided by superconducting fluctuations is dominant only near T_c (which corresponds to $\epsilon = 0$). Moreover the raise is much more pronounced in one- and two-dimensional structures than in three-dimensional ones, which points out that fluctuations are more important for low-dimensional structures.

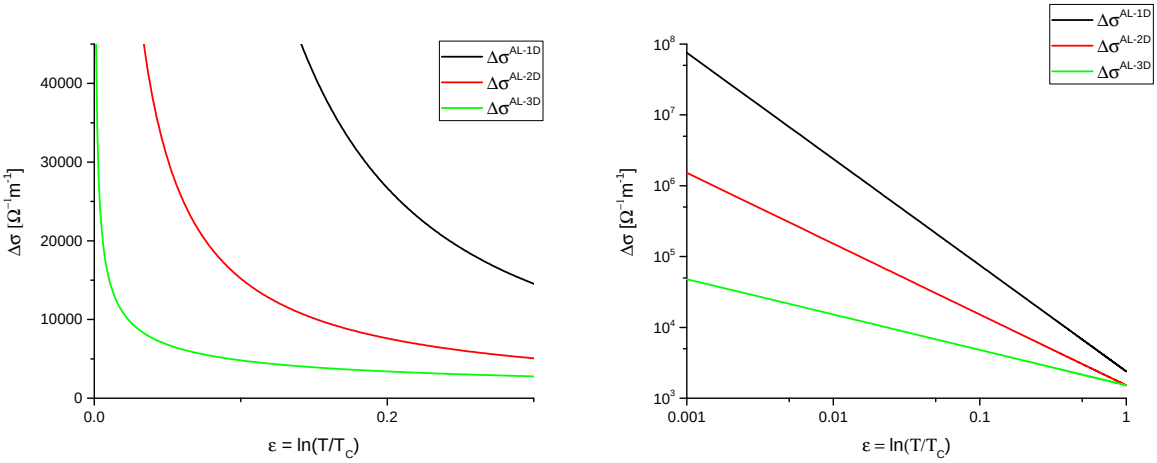

(a) Paraconductivity: linear plot

(b) Paraconductivity: logarithmic plot

Figure 2: Comparison of the three AL formulae for the paraconductivity (12, 13 and 14) for a typical range of ϵ. To create this graph, the following parameters have been chosen: $d = w = 10$ nm and $\xi = 5$ nm.

The Maki-Thompson (MT) contribution: An additional, so-called indirect contribution to the paraconductivity is the Maki-Thompson (MT) contribution, derived by Kazumi Maki [24] and Richard Thompson [25]. It takes into account that a Cooper-pair, which has been produced in a fluctuation, can live longer than the fluctuation itself, until it is broken apart [26]. The MT contribution for a two-dimensional sample is given by the following equation (adapted from [27], by setting $\alpha = 0$):

$$\Delta\sigma_{2\mathrm{D}}^{MT} = \frac{e^2}{8\hbar d(\epsilon - \delta)} \ln\left(\frac{\epsilon}{\delta}\right) \tag{15}$$

This equation has one additional parameter, compared to AL theory: the pair-breaking parameter δ. The MT contribution is only important in clean superconductors, or in other words, in materials with a large inelastic scattering length. But as the AL contribution has a stronger temperature-dependence in 2D-materials, in the range around T_c the AL process dominates in these materials [27].
Figure 3 shows a plot of the AL and the MT contribution in a two-dimensional structure. The parameters for the AL-plot are the same as in figure 2b and for the pair-breaking parameter $\delta = 0.35$ has been used.

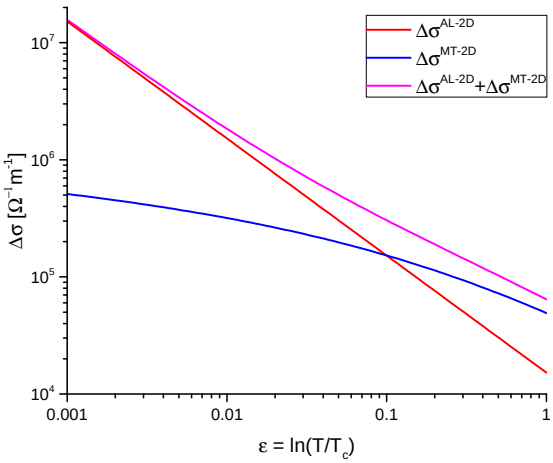

Figure 3: Plot of the AL and the MT contribution for the two-dimensional case. The parameters $d = 10$ nm and $\delta = 0.35$ have been used.

2.2 Magnetoresistance/Magnetoconductivity

The magnetoresistance describes the influence of an applied magnetic field to the resistance of a superconductor above T_c. The magnetic field results in pair-breaking and thus in a suppression of the critical temperature and a reduction of the fluctuation conductivity. Therefore the resistance of a superconducting film near it's transition temperature T_c can be strongly increased by applying a magnetic field because superconducting fluctuations are suppressed by the magnetic field. This gives us the possibility to investigate fluctuations by determining the magnetoresistance. A common quantity to compare samples is the relative magnetoresistance

$$\frac{\Delta\rho}{\rho_0} = \frac{\rho(B) - \rho(0)}{\rho(0)}$$

where $\rho(B)$ denotes the resistivity with and $\rho_0 = \rho(0)$ the resistivity without magnetic field. This quantity results straightforward from measurements.
A theoretical discussion of the influence of a magnetic field on the superconducting fluctuations above T_c was given by E. Abrahams et al. [28]. There, a formula for the excess conductivity by fluctuations $\Delta\sigma^{Abra}$ in a magnetic field was developed, which allowed a reasonable fit of fluctuation magnetoconductivity in thin lead films [29]. It describes the transport in a two-dimensional superconducting film above T_c as a function of the reduced temperature $\epsilon = \ln(T/T_c)$ for a magnetic field B perpendicular to the film. The formula is the following:

$$\Delta\sigma^{Abra} = \Delta\sigma^{AL} \cdot 2\left(\frac{\epsilon}{h}\right)^2 \cdot \left[\Psi\left(\frac{1}{2} + \frac{\epsilon}{2h}\right) - \Psi\left(1 + \frac{\epsilon}{2h}\right) + \frac{h}{\epsilon}\right] \tag{16}$$

$\Delta\sigma^{AL} = e^2/(16\hbar d\epsilon)$ is the AL paraconductivity without magnetic field ($B = 0$) described in equation 13, $h = \frac{2e\xi^2 B}{\hbar}$ and $\Psi(x)$ denotes the digamma function.
A comparison between the fluctuation conductivity in different magnetic fields (perpendicular to the film), described by equation 16, and the paraconductivity (described by AL-theory) can be seen in figure 4.

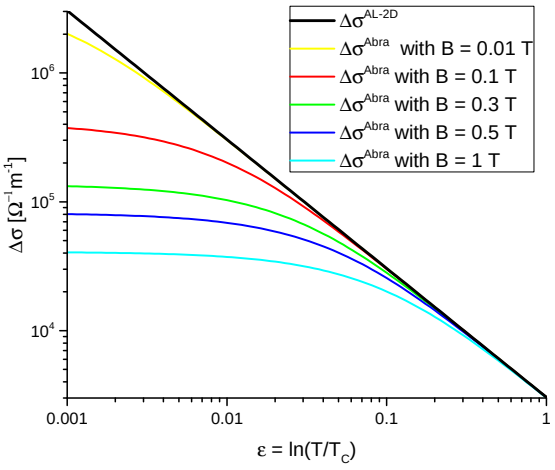

Figure 4: Fluctuation conductivity $\Delta\sigma$ for different magnetic fields (coloured lines) and for the field-free case (black line). The graph for $B = 0$ was plotted with the AL function (equation 13 for 2D), while the coloured graphs were plotted according to Abrahams' formula (equation 16). The parameters $\xi = 7$ nm and $d = 5$ nm were used.

One can see from figure 4 that the curves coincide for high temperatures ($T \gg T_c$), but the magnetic field gains more influence in the vicinity of the transition temperature and there it leads to a suppression of the fluctuation conductivity. As one would expect, for small magnetic fields, the curves plotted by Abrahams' formula come closer to the AL curve.

For the fluctuation analysis it is common to use the magnetoconductivity $\Delta\sigma_B$.

$$\Delta\sigma_B = \sigma(0) - \sigma(B) = \left(\frac{1}{\rho(0)} - \frac{1}{\rho(B)}\right) \tag{17}$$

For this method a measurement with and one without magnetic field is needed. In both measurements the sum of the normal conductivity and the fluctuation conductivity is determined. In many materials the influence of a magnetic field on the normal resistance is small ($\sigma_N(B) \approx \sigma_N(0)$), therefore it cancels out and one can concentrate on the difference of the fluctuation conductivity.

$$\begin{aligned} \Delta\sigma_B &= \sigma(0) - \sigma(B) \\ &= [\sigma_N(0) + \Delta\sigma(0)] - [\sigma_N(B) + \Delta\sigma(B)] \\ &\approx \Delta\sigma(0) - \Delta\sigma(B) \end{aligned} \tag{18}$$

The fluctuations for the measurement in the B-field can be described be Abrahams' formula (16), while those at zero-field follow the equation of Aslamazov and Larkin (13) (presuming that the MT-contribution can be neglected). The difference of these two formulae therefore gives the equation for $\Delta\sigma_B$:

$$\begin{aligned} \Delta\sigma_B &= \Delta\sigma(0) - \Delta\sigma(B) \\ &= \Delta\sigma^{AL} - \Delta\sigma^{Abra} \\ &= \frac{e^2}{16\hbar d\epsilon} - \frac{e^2}{16\hbar d\epsilon} \cdot 2\left(\frac{\epsilon}{h}\right)^2 \cdot \left[\Psi\left(\frac{1}{2} + \frac{\epsilon}{2h}\right) - \Psi\left(1 + \frac{\epsilon}{2h}\right) + \frac{h}{\epsilon}\right] \end{aligned} \tag{19}$$

Note, that for deriving equation 19 the assumption, that the magnetic field has no influence on the normal state conductivity, has been used.

The advantage of magnetoconductivity-measurements, compared to an analysis of the paraconductivity is that the normal-state-conductivity cancels out and it's temperature-dependence does not need to be considered (as long as the magnetoconductivity due to the orbital motion of the normal-state quasiparticles is small compared to the fluctuation effect [30]).
Since the two-dimensional AL equation is parameter-free and Abrahams' formula only contains ξ as parameter, it is possible to determine the coherence length ξ of a material by measuring it's magnetoconductivity and fitting the data with equation 19.

3 Superconducting Single Photon Detectors (SSPD)

Superconducting Single Photon Detectors (SSPDs) are devices, which can register single photons and provide an electrical signal. They mostly consist of a narrow wire of a superconducting thin film and are operated at low temperatures (lower than the superconducting transition temperature of the applied material).
The following chapter contains an explanation of the operation principles, then a brief overview of the main quality features of SSPDs shall be given. Finally some aspects of superconductor/ferromagnet-bilayers for SSPD-devices will be presented. In this thesis no attention will be given to practical aspects e.g. optical coupling and readout electronics.

3.1 Operation principles

The operation principle is the breaking of Cooper-pairs by incident light and the formation of a small resistive region, which can be motivated by the two-temperature-model. The hotspot-model then describes how this small resistive region can lead to a measurable voltage signal.

Experimental discovery of the phenomenon: The perturbation of the superconducting state of lead films by incident light was examined by L. Testardi in 1971 [31]. In his experiments he studied the variation of the film resistance by the illumination with laser light. In the measurements above T_c he observed a rise in the film resistance in all samples, which was caused by the illumination but appeared delayed relative to it. This rise was attributed to heating by the incoming light. Far below the transition temperature in the thin samples (thickness of 275 Å which is of the same order as the optical penetration depth) the rise was much more rapid and the form of the laser pulse was almost perfectly reproduced. This implicates that the response-time has to be less than 5 μs, which indicates that it is an electronic effect because thermal response would be slower by a factor of ten. The fact that the effect is only seen in the thin samples is a further hint that the electronic change in resistance is directly caused by the incident light and not by the light-induced heat.
The effect is phenomenologically described "by a 'bottleneck' in the conversion of optical energy, absorbed by the electrons, to phonons ultimately sent to the heat sink."[31] A considerable amount of carriers therefore is excited by 2Δ and leads to the destruction of superconductivity.

Two-fluid-model: One may ask how it is possible that superconductivity is destroyed below T_c. An approach to explain the phenomenon is to consider a mixture of superconducting carriers and quasiparticles in thermal equilibrium. A requirement for this case is that the time for recombination is much longer than the time for thermal alignment. In theoretical considerations C. S. Owen and D. J. Scalpino found that in such a system at a certain amount of quasiparticles also at zero temperature superconductivity is destroyed by interference of the quasiparticles with the pairing process. This interference gives a negative contribution to the binding energy and leads to a decrease of the superconducting gap. It works most efficient at zero temperature (freely adapted from [32]).

Hotspot detection: The function of a SSPD can be described by the hotspot model. Kadin and Johnson predicted a hotspot-based photodetector in 1996 [33]. Calculations have been done by Semenov et al. in 2001 [34] and Yang et al. showed the effectiveness of this model in simulations (by modeling the superconducting stripe by a inductor in series with a resistor)[35]. An experimental realisation was reported by Gol'tsman et al. [36]. Here a qualitative explanation based on [34], [35] and [36] will be given.
A narrow stripe of a superconducting thin film (deposited on a substrate) is kept at a tem-

perature well below T_c and current-biased with a current I_B little smaller than the critical current I_c at this temperature (for example $T = T_c/2$ and $I_B = 0.9I_c$). The supercurrent passes through the stripe and no voltage can be measured (see figure 5 a). When a photon with an energy $h\nu \gg 2\Delta$ is absorbed by the film, it dissipates it's energy to the electron system and thus it causes the appearance of excited hot electrons and the formation of a resistive hotspot (see figure 5 b). The supercurrent through the stripe is forced to flow outside the hotspot, because otherwise the Cooper-pairs would have to break apart. As a consequence the current density in this region is enhanced (figure 5 c) and if I_B has been chosen sufficiently close to I_c, the current density exceeds the critical current density. This leads to a breakdown of superconductivity at the whole width of the stripe (scenario d in figure 5). Joule heating caused by the current flowing through the resistive region leads to a faster growth of a normal-conducting segment along the wire. In this way a measurable voltage pulse is generated.

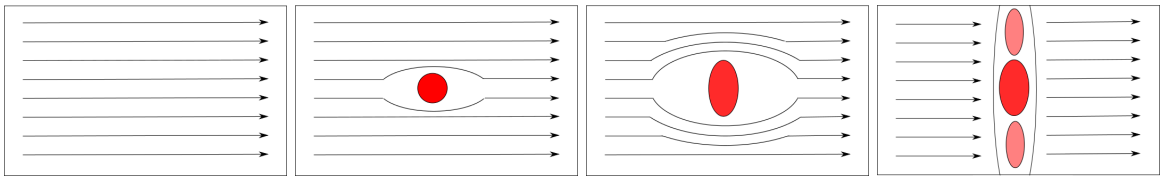

(a) (b) (c) (d)

Figure 5: Schematic picture of hotspot formation in a narrow superconducting stripe: Current passing through the stripe (a), a small resistive hotspot caused by an incoming photon (b), enhanced current in the superconducting region (c) and the formation of a resistive barrier over the full width of the stripe because of current density exceeding the critical current density (d). After [37].

The requirements for the function of a SSPD according to this model are the following: The stripe has to be so narrow that the size of the resistive hotspot relative to the size of the wire is large enough to cause a notable change in the current density and the bias current has to be big enough to exceed the critical current when it has to pass the hotspot. Moreover the energy of the incoming photon has to be high enough to break up Cooper pairs.
The minimal hotspot-size r is given by a simple relation (the deduction of this simple formula is shown in appendix B):

$$r \geq \frac{w}{2}\left(1 - \frac{I_B}{I_c}\right) \tag{20}$$

where w denotes the stripe's width. In 2014, J. Renema et al. claimed that only high-energetic particles really cause a cylindrical resistive hotspot as depicted in figure 5b, whereas for low-energy-photons a model that predicts vortex-unbinding and weakening of superconductivity by diffusion of quasiparticles in an extended region of the nanowire is more appropriate to explain the experimental results [38]. The hotspot model predicts a minimal photon energy to create a hot-spot, which is big enough to trigger a voltage pulse. Experiments indeed show that also low-energetic photons can be detected, a fact which cannot be explained by this model. A model that is able to describe the process for low-energetic photons is the model of fluctuation-assisted detection.

Fluctuation-assisted detection: Fluctuations of the Cooper-pair density, thermal activation of magnetic vortices and phase-slips randomly occur in the superconducting nanowires and are thus responsible for the dark counts. Incoming photons, even with low energies, enhance the probability of such fluctuations (for example the "jump" of a vortex) to appear, and to trigger thus a counting event. The most important process, which causes dark counts

in superconducting meander lines is the unbinding of vortex-antivortex-pairs [39]. The bigger the superconducting energy gap 2Δ, the higher the smallest binding energy U of such a pair gets. The probability for the excitation across this energy barrier is proportional to $\exp(-\frac{U}{k_B T})$. The absorption of a photon can lead to a local reduction of the superconducting energy gap and thus to a higher probability for the unbinding of a vortex-antivortex-pair, which causes a count. This model is used to explain the detection of infraread-photons. For further informations see [40] and [41].

The kinetic-inductance model: An altenative process, which can be responsible for photon detection, is based on the change of the SSPD's kinetic inductance. The kinetic inductance based photoresponse is faster and less sensitive at the bias current than the resistive photoresponse. It is most pronounced in the vicinity of the transition temperature, whereas, according to [42], at temperatures far below T_c, the resistive response makes the main contribution.
The kinetic inductance is the inductance resulting from the kinetic energy of the charge carriers and is described by formula 21.

$$L_k = \frac{l}{wd}\frac{2m}{(2e)^2 n} \tag{21}$$

l denotes the nanowire length, wd the cross section, n the Cooper-pair-density, m the electron mass and e the electron charge. Since L_k scales with $l/(wd)$ it has a crucial influence on nanowires with small cross-section. Furthermore the kinetic inductance is an important parameter for superconductors because in these materials - in difference to normal metals - the charge carriers do not lose their kinetic energy because of collisions.
The derivation of formula 21 and further information on the kinetic inductance are given in appendix A.
The main idea of this model is, that an incoming photon breaks Cooper-pairs and therefore leads to a reduction of n, which causes a rise of the kinetic inductance. By this change of L_k a measurable voltage-pulse

$$V_k = I_b \frac{dL_k}{dt} \tag{22}$$

is produced. One can easily imagine: As Cooper-pairs are destroyed, the remaining Cooper-pairs have to accelerate in order to carry the bias current and thus L_k grows, which causes the photo-response signal [43].

A simple circuit as model for an SSPD: To explain the electrical response, the detector can be modelled by a circuit as shown in figure 6. The part in the dashed rectangle represents the nanowire with it's normal-state-resistance R_n and the kinetic inductance L_k. R_L denotes the load impedance of the signal output line.
The appearance of the photon-induced resistive hotspot corresponds to opening the switch in the circuit. Then the current has to pass through the resistor R_n, which represents the normal resistance of the superconducting nanowire. As a consequence the bias current decays with a time constant $\tau_1 = \frac{L_k}{R_L + R_n}$. The lowering of the current leads to a reduction of Joule-heating and thus to the reappearance of superconductivity. Then the bias current recovers to it's initial value with a time constant $\tau_2 = \frac{L_k}{R_L}$. Since in general R_n is much bigger than R_L, we have $\tau_2 \gg \tau_1$. After this time the detector is in the initial state again and the next photon can be detected. For further information see [44].

After the description of the principles for device operation, now the required qualities of an SSPD will be discussed.

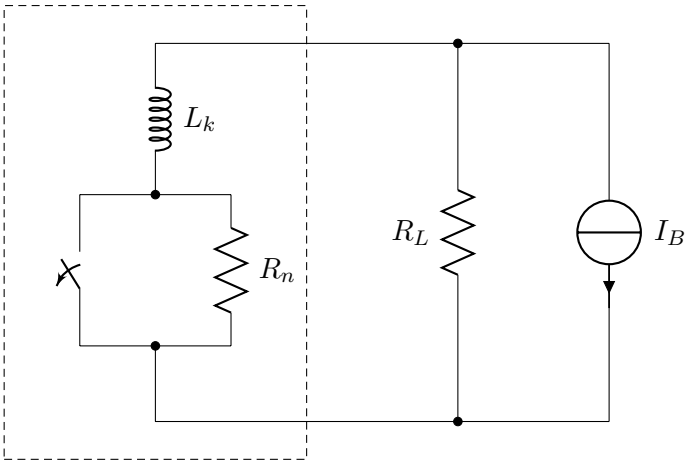

Figure 6: Circuit to model an SSPD by it's normal resistance R_n and it's kinetic inductance L_k. The SSPD is current-biased with I_B. R_L represents the load impedance of the signal output line.

3.2 Quality features of SSPDs

There are several properties we expect of an SSPD: It should be fast and count a high percentage of the photons, which hit the detector and it should not give a signal when no photon comes in. Therefore we can find a list of quality features:

- **Detection efficiency:** The system detection efficiency denotes the percentage of incoming photons that are registered by the detector. In the ideal case each photon reaches the detector, is absorbed and registered. In the real case there is a certain probability η_{coupling} that the photon reaches the detector (which depends on the optical coupling), a probability $\eta_{absorption}$ that it is absorbed and finally a probability $\eta_{\text{registering}}$ that the photon is registered. The system detection efficiency is then given by

  $$SDE = \eta_{\text{coupling}} \cdot \eta_{\text{absorption}} \cdot \eta_{\text{registering}}$$

  while the quantum efficiency or device detection efficiency (DDE) is described by the following term:

  $$DDE = \eta_{\text{absorption}} \cdot \eta_{\text{registering}}$$

  The difference is that the SDE takes into account that not all photons reach the detector. Therefore the SDE is the experimentally accessible quantity, whereas the DDE is the quantity which really describes the quality of the detector. This description of SDE and DDE is taken from [37]; be aware that a different notation than in the article is used .

- **Dark count rate (DCR):** The dark count rate is the number of signals, which are produced by the detector although no photon hits it's surface. A reliable detector must have a low DCR. The DCR strongly depends on the bias current and the operation temperature. Fluctuations have often been discussed as the source of dark counts in SSPDs. There are various mechanisms for fluctuations:

  - **Fluctuations of the number of quasiparticles:** Thermodynamic fluctuations can cause a change in the number of quasiparticles in a small volume, which can lead to a detection event. Since the number of fluctuating Cooper-pairs to trigger a voltage pulse is dependent on the bias current, these events only have a reasonable probability as I_B is near I_c. Engel et al. received good fits by combining the

fluctuation model with a model based on the unbinding of vortex-antivortex-pairs (explained below) [45, 39].

- **Phase-slips:** Phase-slips are a typical phenomenon for 1D-materials. By thermal fluctuations wire-segments in the size of the coherence length become normal-conducting for a short period (typically some picoseconds). Whenever such a resistive segment appears, the superconducting phase "slips" by 2π. In this process the energy of $I\Phi_0$ (where I denotes the current and Φ_0 is the flux quantum) is dissipated. [46, 47].
  According to [48] the probability for the appearance of a phase-slip in an SSPD is by two orders of magnitude less than for vortex-hopping or the unbinding of vortex-antivortex-pairs.
- **Unbinding of vortex-antivortex-pairs (VAPs):** In 2D-materials a phase transition, the so-called "Berezinsky-Kosterlitz-Thouless" (BKT) transition can occur at a specific temperature T_{BKT}. Below this temperature it is energetically favourable for vortices to align in pairs, the VAPs. (The term vortex-antivortex denominates two vortices with their supercurrents circulating in the opposite direction.) The bias current in the superconductor induces a Lorentz-force acting in the opposite direction for the two vortices, which causes the VAP to align perpendicular to the current. In this position the VAP-binding energy is minimal.
  This energy $U_{VAP}(I_B, T)$ is now the energy barrier which has to be exceeded to cause decoupling of a VAP. The probability for thermal decoupling or rather the DCR depends on Boltzmann's factor

$$DCR(I_B, T) = \Omega \cdot \exp\left(-\frac{U(I_B, T)}{k_B T}\right) \tag{23}$$

  with Ω the attempt frequency and U the energy barrier. When the VAP is broken apart, the single vortices move - driven by the Lorentz-force - to the opposite edges of the superconducting stripe. When a vortex moves, energy is dissipated in the superconducting film, which leads to the appearance of a normal-conducting domain and the generation of a voltage-pulse.
- **Vortex hopping (VH):** Under VH we understand the process that a vortex enters the superconducting stripe at it's edge and - due to Lorentz-force - passes through it, thus leading to the appearance of a normal-conducting domain. The entrance of vortices is possible in most of the cases in SSPDs because, if I_B is near the depairing I_c, the magnetic field at the edges is higher than the critical field for vortex-entry.
  The probability for such an event is given by Boltzmann's factor 23, but with a energy barrier $U_{VH}(I_B, T)$ characteristic for the VH process.

- **Single-photon-sensitivity:** We demand that each photon is registered, so even one single photon must be able to generate a signal. This quality strongly depends on the photon energy and the bias current. For low-energetic photons it can depend on the bias current if one photon is enough to trigger a counting event or if two or more photons are needed [36] (See the discussion of the bias current in the next chapter.)

- **Speed/recovery time:** When a photon hits the superconducting nanowire of the SSPD, it lasts some time τ_1 until the detector segment becomes normal-conducting and thus generates the voltage pulse. After this event a much longer time τ_2 is needed until the nanowire becomes again fully superconducting, the bias current recovers and the detector is able to register the next photon. In the meantime the detector is insensitive to incoming photons. For practical applications it is desirable that this time-span of

insensitivity, the recovery time $\tau_{recovery}$ of the SSPD, is short.
The recovery time is determined by both, thermal and electrical properties of the device. On the one hand it is desirable to have a short electrical recovery time (the time until the supercurrent is restored after a detection event), which can be achieved by lowering the kinetic inductance L_k and increasing the load impedance R_L since $\tau_2 = L_k/R_L$ (see previous chapter). On the other hand the thermal recovery time has to be lower than the electrical one, which means that the heat has to be transferred to the substrate before the current returns, because otherwise Joule-heating causes a resistive hotspot and the wire remains resistive, it falls into a so-called "latched"-state.
In general, the thermal recovery time is much shorter than the electrical recovery time and efforts are made to hold the electrical recovery time as short as possible.

- **Jitter:** The term jitter denotes the temporal misalignment of the detection events. Mathematically it is defined as the full width at half maximum of the Gaussian curve, which describes the distribution of photon detection events. The jitter in an NbN-nanowire-SSPD consists of an SSPD-intrinsic component and a component proportional to the signal-to-noise-ratio (SNR) of the detector. Extremely small values (a total of 18 ps with estimated 15 ps of intrinsic jitter) have been reported for NbN-nanowires [49].

- **Wavelength sensitivity:** The small energy gap of superconductors makes it possible that even low-energetic photons can lead to an output signal by breaking up Cooper-pairs and triggering fluctuations. This makes SSPDs interesting for wavelengths in the visible and infrared range of the electromagnetic spectrum.
The photon energy decides which bias current has to be applied; x-ray dectors working at $I_B = 0.4\%I_c$ have been reported [50], whereas for for photons in the visible and infrared range typical bias currents are much higher. Figure 7, taken from [41], shows the wavelength-dependence of the DDE. We see a constant DDE in the region below 700 nm (corresponding to energies higher than 1.77 eV) and then a decrease with the increase of the photon wavelength. The area of constant DDE (at relatively high energies) is attributed to the hot-spot based photo-response, whereas for the low-energy regime another explanation (than the fluctuation-based detection) has to be given. The solid lines in the graph represent fits of the data with the VAP-model. This graph also illustrates the dependence of the DDE on the bias current.

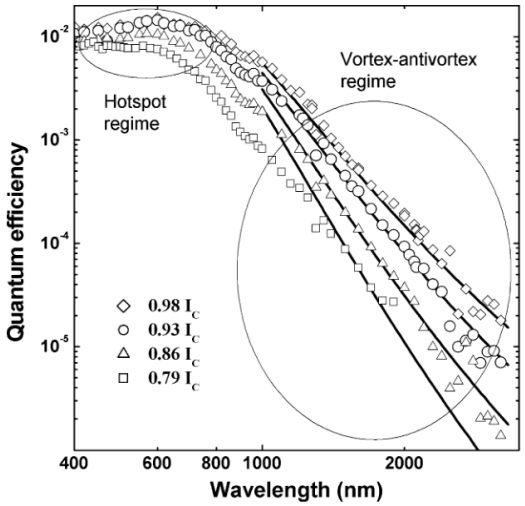

Figure 7: Dependence of the quantum efficiency on the photon wavelength and the applied bias current. Experiments were performed on a 4 nm thick NbN sample at $T_c/2 \approx 5.75K$. Symbols represent experimental data, solid lines show fits with the VAP-model. Reprinted from [41], Copyright 2008, with permission from Elsevier.

3.3 Tuning parameters

- **The bias current I_B:** The bias current is the most important parameter to tune an SSPD. The ideal bias current for an SSPD depends on the photon energy; the lower the photon energy the higher the bias current has to be. Gol'tsman et al. reported that experiments performed at $I_B = 0.92I_c$ showed single-photon-sensitivity and a low dark-count rate, whereas higher bias currents led to a high DCR and lower values for I_B caused two-photon- (for $I_B = 0.8I_c$) or three-photon-operation with low DDE [36]. The detection efficiency grows exponentially with the bias current [51] and jitter of a detector device is lower for higher values of I_B, but the DCR strongly grows with I_B especially when I_B approaches the critical current. In [34] it is reported that the difference between I_B and I_c should be a few times the root mean square fluctuation of the critical current $\delta j_c = (dj_c/dT)\delta T$ with $\delta T = \sqrt{4k_B T^2/(cV)}$ and $c = c_e \cdot \exp(-\frac{\Delta}{k_B T_c})$. c_e is the electron specific heat at T_c and $V = wd\xi$ with w the width, d the thickness of the stripe and ξ the superconducting coherence length. Therefore one goal in the development of SSPDs is to find materials with high critical current density in order to use high I_B without reaching I_c.

- **The nanowire thickness:** Nanowires for SSPDs typically have a thickness of about 5 nm. In [40] the device detection efficiency is determined for devices with thickness between 4 nm and 12 nm. It is shown that the above-mentioned decrease of the DDE with decreasing photon energies is shifted to lower energies for thinner wires. Therefore the thinner the wire the lower the photon energy can be. On the other hand for radiation with higher photon energies (such as X-rays) thicker detector arrangements are favourable, because the absorbance in thin-film SSPDs is very low for high-energy radiation [50].

- **Form of the SSPD:** The first SSPD consisted of a simple superconducting straight wire. It is required that the nanowires are narrow to allow the hotspot detection, on the other hand they should cover a large area. Recent SSPDs mostly use a long thin wire in a meander structure to have a big surface where photons can be absorbed. As discussed before, the kinetic inductance is proportional to the wire length and a high value of L_k leads to long recovery times. Therefore efforts have been made to find alternative structures. One approach is to use an array of parallel wires, which is biased near the critical current of the whole array. When one wire is hit by a photon it becomes resistive and the current is spread to the other wires, exceeding here the critical current density. Therefore the whole array is driven into the normal state. SSPDs of this type have been reported to be faster and generate a higher output signal than meander SSPDs [52].

- **Material:** The standard material for the construction of SSPDs is NbN, but SSPDs based on other materials such as for example Nb, NbTiN, TaN or the high-T_c superconductor $YBa_2Cu_3O_7$ have been reported [37].
  It is important that the superconductor's transition temperature is possibly high and that the nanowires made of this material show a high critical current density j_c. Some other crucial material's parameters are the density of states at the Fermi energy, the superconducting gap and the kinetic inductance [53].

3.4 Superconductor/Ferromagnet-bilayers for SSPDs

Recently superconductor/ferromagnet (S/F) bilayers have been proposed for SSPDs. According to [43] the superconducting and the ferromagnetic layer interact with each other due to the proximity-effect. The specific lengths for this interaction are given by the material's coherence-lengths ξ_S and ξ_F for the superconductor and the ferromagnet, respectively. In the mentioned article reduced (kinetic-inductive) response-times relative to pure Nb films have been reported for Nb/NiCu-bilayers. Pump-probe experiments, in which the transient reflectivity of the sample was measured, showed that Nb/NiCu bilayers exhibit a much faster relaxation than the pure Nb films (see figure 8a).
The most important task for the ferromagnetic layer is to enhance the critical current density j_c of the superconductor. Marrocco et al. found strongly enhanced critical current densities for the S/F bilayers, which led to higher voltage pulses and a lower noise level (see figure 8b). As can be seen in the normalized plot of the peaks in the inset of this figure, no difference in the shape of the photo-response signal could be observed.
A possible explanation for the enhancement of j_c is that the ferromagnetic layer improves the pinning of vortices by diffusion of ferromagnetic particles into the superconducting layer and by the presence of magnetic domain walls [54].
The presence of the ferromagnetic layer also deeply influences the dark-count dynamics. Nasti et al. found lower DCR in superconductor-ferromagnet (namely NbN/NiCu) bilayers in comparison to pure superconducting layers. By fitting their experimental data with the fluctuation models (see section 3.2) they revealed that in NbN/NiCu-bilayers the needed excitation energys both for the breaking of VAPs and for VH are higher than in pure Nb films. Moreover they pointed out that in NbN/NiCu-bilayers VH is a more probable process than the breaking of VAPs, while for pure NbN films the opposite is the case [55].

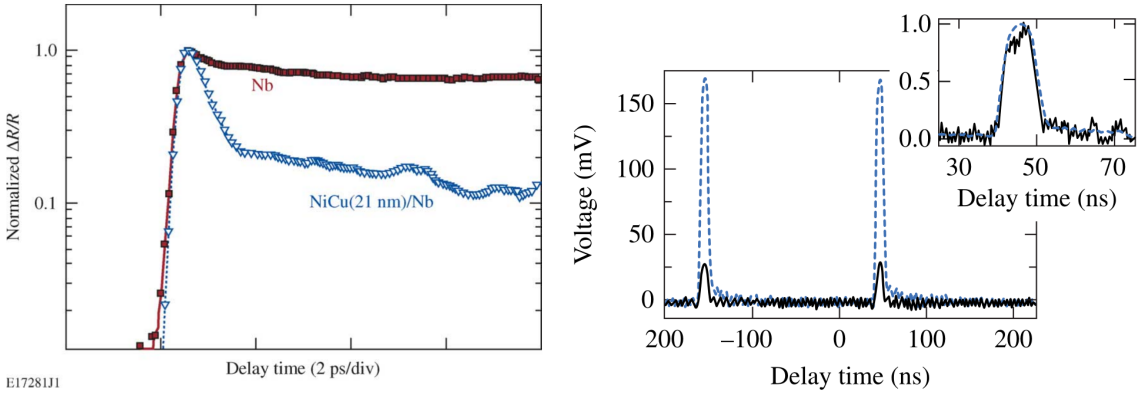

(a) Pump-probe experiment of Nb films and Nb/NiCu bilayers

(b) Photoresponse transient voltage for NbN (solid line) and NbN/NiCu (dashed line)

Figure 8: Comparison of the photoresponse of S thin films and S/F bilayers. The left image shows measurements of the transient differential reflectivity $\Delta R/R$ of a 70 nm thick Nb film and a Nb (70 nm)/NiCu (21 nm) bilayer at a temperature of 6 K. Image taken from [43], copyright ©2009 IEEE.
The right graph shows the photoresponse transients for a NbN film and a NbN/NiCu bilayer measured at a temperature of 4.7 K and a bias current of 84% I_c for the NbN strip and 60% I_c for the NbN/NiCu bilayer. Reprinted with permission from [54]. Copyright 2010, AIP Publishing LLC.

4 The measurement devices

4.1 The closed-cycle cryostat

The closed-cycle cryostat is an apparatus, which allows to do measurements at temperatures between 300 K and 9 K and in magnetic fields up to about 1 T. An image of the measurement apparatus is shown in figure 9.

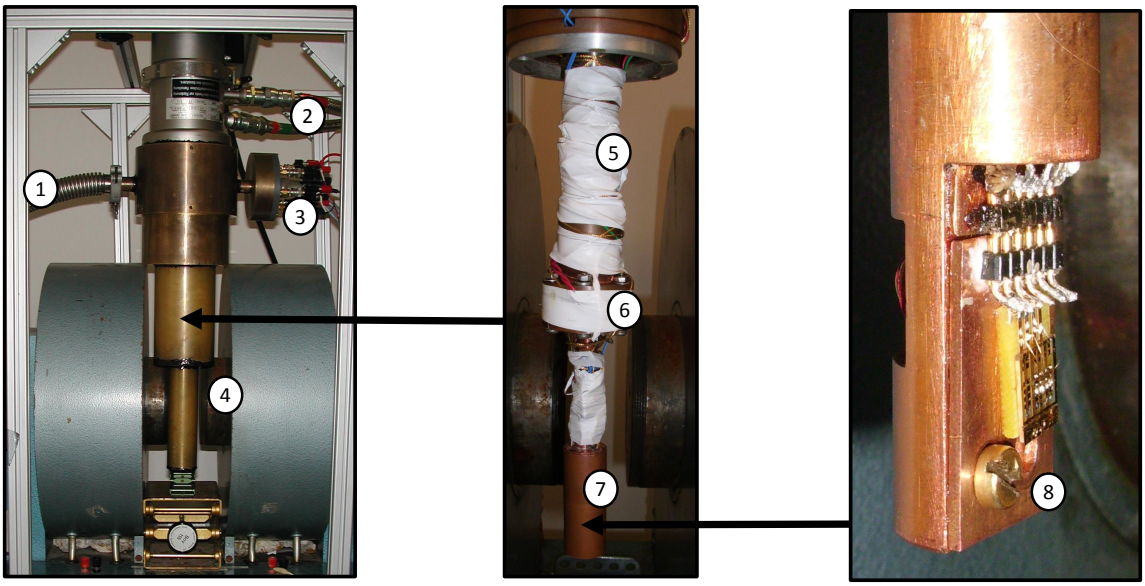

Figure 9: Photographs of the closed-cycle cryostat. In the left picture one can see the cryostat and it's connections, in the middle the apparatus is open and it's components are marked. The right image shows the copper-block with the sampleholder with the NbTiN/NiCu sample on it. The numbers of the marked parts are explained in table 1.

1	Connection to the vacuum pump
2	Connection of the cold-head to the compressor unit
3	Connection to the electronic measurement devices (to the current-source, the voltmeter and the temperature-controller).
4	The electromagnet
5	The cold-head (wrapped with Teflon-tape to fixate the wires, which go down)
6	Position of the temperature-sensor B and the heating element number 2 (see text)
7	Copper-cylinder, covered by a copper-cap. Inside this cap there are the temperature sensors A and D and the heating element number 1. Sample-holder and sample are mounted on the copper block in the cylinder, too. A detailed view of this copper block is given in the right image.
8	The sample-holder with the sample on it

Table 1: Explanation of the numbers in figure 9.

Figure 9 gives an overview of the closed-cycle cryostat and it's components. The outside of the apparatus is made from brass and the inner part from copper because of it's good thermal conductivity.

Cooling and temperature control: For cooling a closed-cycle refrigerator of Leybold was used. It consists of a *Coolpack 6000 D* compressor unit and a *COOLPOWER RGD 5/100T* cold-head. The apparatus works with He gas, which is compressed by the compressor unit and expands in the cold-head, where the coldness is produced according to the Gifford-McMahon process (for further informations to the cooling process see for example reference [56]). The compressor itself has to be water-cooled, which is realized by a cooling loop connected to the in-house air conditioning.
The cooling power of the cold head is transmitted to the sample by a copper stick. To provide effective cooling, it must be prevented that heat from outside the cryostat comes in. This is managed by evacuating the measurement chamber, which prevents heat conduction by the air. Additionally a cooled aluminum shield between the cold copper block and the brass cover of the cryostat, which is at room temperature, reduces the heat transfer by radiation.
The refrigerator can only be switched on or off, but it is not possible to control it's cooling power. To keep the sample at a constant temperature, it is heated. There are three temperature sensors and two heating elements. One sensor (B) and one heating element (number 2) are situated at the upper end of the copper-rod, near the cold head, the other two sensors (A and D) and the heater number 1 are built into the copper-block near the sample. This gives the possibility to regulate the temperature at two points. Experience showed that the regulation process works best, if the temperature at the cold-head is 3.5 K lower than that desired at the sample[2].
The temperature is regulated by a *LakeShore 340 temperature controller*. This device reads out all three sensors and regulates the heating power for both heating elements (an additional power-supply *HP 6291A* is used for the heating element number 2). It is possible to manually set a temperature setpoint, at which the temperature will be held until the setpoint is changed. Moreover a ramp can be set. Then the temperature controller changes the temperature at a constant rate (for example a ramp with a rate of 0.3 K/min was used for resistance measurements). The temperature controller can communicate to the computer, which gives the possibility to automatically set new setpoints and to read out the sample's temperature during measurements.
One of the three temperature sensors (sensor A) is a rhodium-iron (RhFe) sensor, which is calibrated to the absolute temperature. This sensor is situated in the copper block near the sample and is therefore used to determine the sample's temperature. The sensor was tested by a reference sensor, which was mounted like a sample (for details see appendix D). The other two sensors (B and D) are Cernox^{TM} sensors of LakeShore. They have the advantage that - in contrast to the RhFe sensor - they are only weakly influenced by magnetic fields[3]. Therefore they are used for temperature regulation during measurements in magnetic fields.

The vacuum system: The chamber inside the cryostat is evacuated during measurements. This has two reasons: On one hand the vacuum lowers the heat conductance from the walls to the sample because no particles are available, which could transfer the heat. On the other hand it is important that no air is in the chamber, because air contains water in form of vapour, which would form ice crystals at low temperatures.
The vacuum is provided by a *HiCube 80, Eco turbomolecular pump* of Pfeiffer. The maximal pressure at the beginning of the cooling process is about 1×10^{-3} mbar, a typical pressure during measurements in the cooled state is 3×10^{-7} mbar.

[2] At the beginning of the measurements the optimal temperature difference was 3 K. But in the time-span, in which the measurements were performed the copper rod, which connects the sample to the cold head, broke several times and had to be glued. This influenced the thermal conductance and therefore actually a temperature difference of 3.5 K between the two heating elements is ideal.

[3] We tested the Cernox-sensor D and saw that at 9 K the measured temperature changes about 0.1 K when the magnet is switched on. At higher temperatures the change caused by the magnetic field is smaller than 0.02 K.

Electrical connections and measurement devices: Six coaxial cables are used for the electrical signals; two transport the measurement current to the sample, two are used for voltage measurement and two for Hall-voltage. Additionally there is a cable with two wires, which has the task to bring power to a pre-amplifier, which can be built in into the cryostat. All cables except the current-supply-leads go to a plug connection and from there further coaxial cables proceed, which end in a pin socket, where the sample-holder can be plugged in. The connections are shown in figure 56 in appendix E[4].
The sample holder consists of a copper plate with six pins on the top side (see right image in figure 9). The samples were fixated on the sample-holder by Apiezon vacuum grease. The electrical connections were realised by 50 μm thick gold wires, which were connected to the gold pads on the sample and to the pins on the sample-holder by silver-paste. For the current measurements only four of the six pins were used.
For the transport measurements two measurement devices of Keithley were used. The DC measurement current was provided by a Keithley *6221 DC and AC current source*. For the voltage measurements a Keithley *2182A nanovoltmeter* was used. Both devices can be controlled by the computer via a GPIB interface.

The magnet: The closed-cycle measurement device is equipped with an electric magnet (*B-E 15 S8*, produced by Bruker). It is operated with a *fug NTN 2 800-65* power supply. A custom-made controlling-unit is used to adjust the current produced by the power-supply. The controlling unit can be settled manually or automatically. To control it from the computer a digital to analogue converter (DAC) is needed. Since it was necessary to renew this device during the measurements for this thesis, a detailed description of the new control system is given in appendix F. The current through the coils of the magnet can be varied between 0 A and 30 A and the polarity of the field can be changed. The controlling unit also has the task to protect the magnet of overheating. Since the magnet is water-cooled, not only the temperature of the coils but also the water flux through the magnet is measured. If the water-cooling is stopped or the magnet becomes too hot, the current through it is switched off.
It is also possible to rotate the magnet around the cryostat, which gives the possibility to orientate the field parallel or perpendicular to the sample. Also the gap between the two coils of the magnet can be varied. At a gap sized 50 mm and with the maximal current of 30 A the magnet provides a field of $B = 0.92\ T$. A measurement of the magnetic field, dependent on the current through the coils, was performed. It can be seen in appendix G.
During all measurements for this thesis the magnetic field was oriented perpendicular to the superconducting film and the gap had the constant value of 50 mm.

[4]The circuit shown in figure 56 does not represent the actual state, because during the measurements a change was made: The connection between the outer wires of the coaxial cables was removed and now the outer wires are used instead of the inner wires for the voltage- and Hall-voltage contacts.

4.2 Dip-stick and He-dewar

The dipstick is used to perform measurements in the He-dewar. Thus, temperatures down to 4.2 K can be reached. The temperature is varied by moving the stick up and down in the dewar in the space above the liquid. The disadvantage of this method is that it is not possible to hold the specimen at a constant temperature (except 4.2 K) for a longer time-span.
The stick is constructed in a simple way. It consists of a hollow tube with a copper cylinder at it's end. In the copper block there is a notch, where the sample can be placed. Moreover a RhFe temperature sensor is mounted in a hole of the copper block. The whole cylinder can be covered by a cylindrical copper cup. The tube goes through a blank flange and can be fixated there with a screw. During measurements the blank flange is mounted on the helium dewar and the stick can be pushed down and up through it. An image of the stick can be seen in figure 10.

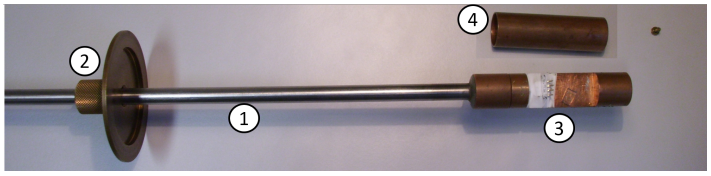

Figure 10: Photograph of the dipstick, used for measurements in the He-dewar. The metallic tube (1) contains the wires for the electrical connection. It goes through the flange (2), at which it can be fixated. The sample is mounted in the notch of the copper cylinder (3), which is then closed by the copper cup (4).

Eight wires are used for electrical connection, four of them are used for the temperature sensor, the other four can be connected to the sample. At the upper end the wires end in a male 10-pin connector.
A cable connects the 10-pin-connector to a distribution box, where it is connected to the measurement devices. During my thesis it was necessary to build a new distribution box, but most of the measurements were done with the old one. Both exemplars are shown in figure 11. A detailed description of the new one is given in appendix H.
For the transport measurements the same devices as in the closed cycle cryostat were used, namely a Keithley 6221 DC and AC current source and a Keithley 2182A Nanovoltmeter. The resistance of the temperature sensor was measured by a Keithley 2000 multimeter in four-probe operation. The temperature was then calculated from the resistance in the measurement program by interpolation with a calibration file.

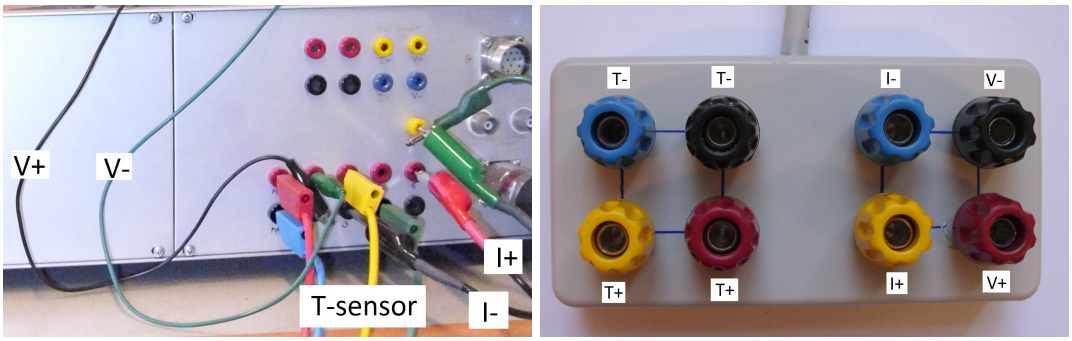

Figure 11: Pictures of the distribution box. The old one at left and the new one at the right side. The letters explain the connections: $I+$ and $I-$ are the current contacts, $V+$ and $V-$ the voltage contacts. The temperature sensor has two positive ($T+$) and two negative contacts $T-$. It does not matter, which of them is used as current and which as voltage contact.

5 The measurement routines

This chapter is dedicated to the measurements and the measurement programs.
In all measurements voltages are measured. For a proper measurement two points have to be taken in consideration:

- Four-probe measurements avoid that the resistance of the measurement leads and the connections is added to the sample's resistance. In four-probe technique two wires are only used to supply the current and the voltage is measured at the other two wires. Thus only a negligible small current flows through the voltage leads and therefore their resistance is not measured.

- There may be a thermal voltage V_{therm} caused by the contacts, which is measured in addition to the voltage drop at the resistance. Since the thermal voltage does not depend on the current, which flows through the sample, it is possible to get a corrected result by making two measurements with the current in the opposite directions. In the first measurement $Vp = V_{sample} + V_{therm}$ and in the second one $Vn = -V_{sample} + V_{therm}$ is determined. Then $V_{sample} = (Vp - Vn)/2$ gives the correct value.

All measurement programs are written in the programming environment *TestPoint*. The programs for the resistance versus temperature measurement (see figures 12 and 13) and for the determination of the magnetoresistance (see figure 14) were programmed by other group members and had already been used for previous measurements. Only small changes were made to these three programs during the measurements for this thesis. The programs for the IV-characteristics and the temperature dependence of the critical current were developed in the framework of this thesis.

5.1 Resistance versus temperature (RT)

5.1.1 RT measurement performed in the closed cycle cryostat

For this measurement a temperature sweep with a cooling rate of 0.3 K/min was set directly at the temperature controller. The measurement was controlled by the computer with the program shown in figure 12.

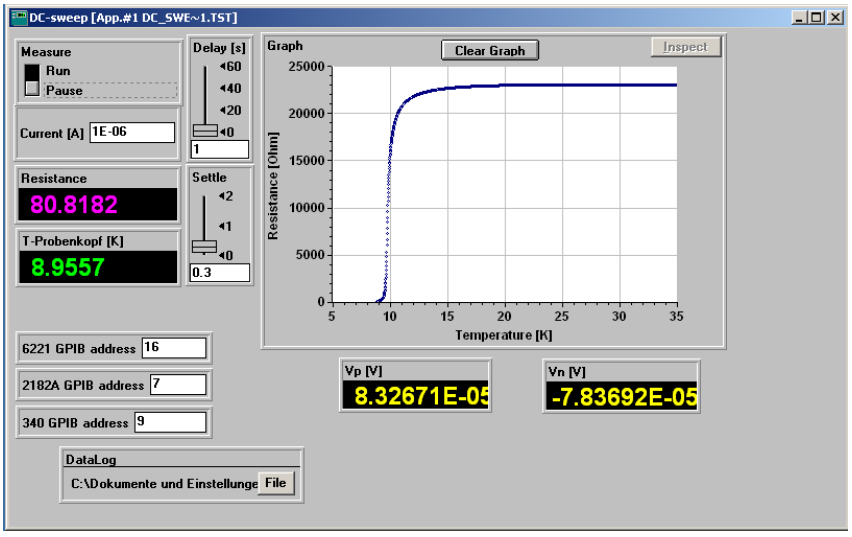

Figure 12: Screenshot of the measurement program used for resistance versus temperature measurements in the closed cycle cryostat.

Function of the program

(1) For the measurement the measurement *current* is switched on.

(2) The routine pauses for the time-span set by the *settle* menu.

(3) Then the voltage *Vp* is measured, the current is switched off.

(4) The temperature *T-Probenkopf* is requested from the temperature controller (sensor A).

(5) Afterwards the current is switched on in the opposite direction.

(6) The routine pauses again for the time-span set by the *settle* menu.

(7) Then the voltage *Vn* is measured, the current is switched off.

(8) The values are saved to the *DataLog* file and the *Resistance* is calculated. A point is set to the graph.

(9) This process is followed by a *delay*.

The steps 1 - 9 are repeated until the program is switched off.

There are three parameters to set in this program:

- *Current [A]:* gives the measurement current, which is sent through the sample.
- *Settle [s]:* gives the delay time between switching on the current and measuring the voltage.
- *Delay [s]:* gives the delay between the single measurements.

The typical values used in the measurements for this thesis are: *Current* = 1 μA, *Settle* = 0.3 s and *Delay* = 1 s.

5.1.2 RT measurement performed in the He dewar

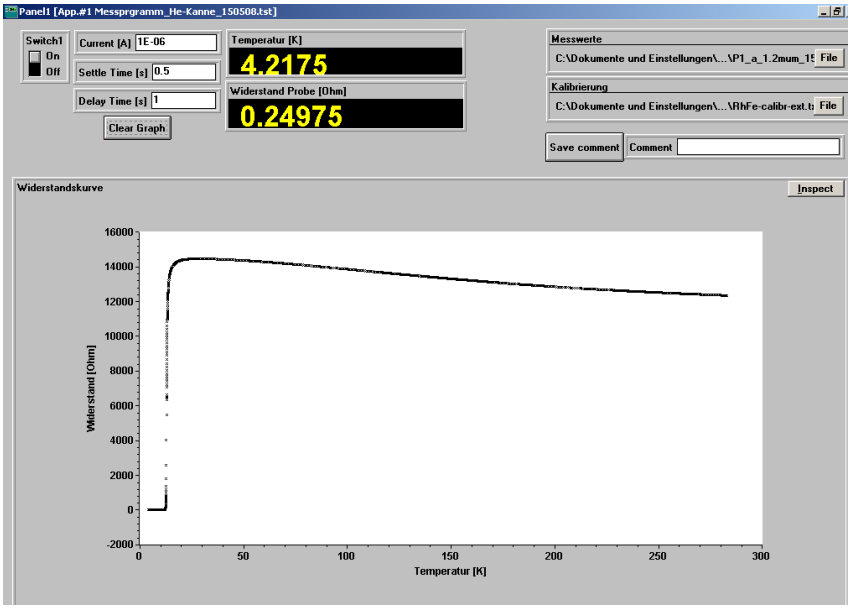

Figure 13: Screenshot of the measurement program used for resistance versus temperature measurements in the He-dewar.

The measurement in the He-dewar is performed in an analogous way. The main difference is that there is no temperature controller. Therefore the temperature has to be changed manually by pushing in the dip-stick and in step four (see previous page) instead of the temperature the resistance of the RhFe sensor (see section 4) is requested and the temperature is calculated in the program. A screenshot of the program used for these measurements is shown in figure 13. In this program an additional file is needed, which contains the calibration curve of the RhFe sensor. Moreover the measurement file is called *Messwerte* instead of *DataLog* and there is a possibility to write comments to the file.

5.2 Magnetoresistance

Magnetoresistance measurements were performed in the closed cycle cryostat. For this purpose the program shown in figure 14 was used, which controls the electronic measurement devices, the temperature controller and the magnet.

Description of the program:

- *Initiate:* When this button is pressed, the values set in the other menus are transmitted to the measurement devices.
- *Start:* When this button is switched on, the measurement is running.
- *NPLC-Speed* gives the integration time of the nanovoltmeter. If the option "medium" is chosen, it integrates over one power-line-cycle (which is 0.02 s), if "slow" is chosen, over five (which corresponds to a measurement time of 0.1 s).
- *TempDiff* sets the temperature difference between sensor B at the cold head and sensor D near the sample.
- *TempStab [s]:* When a new temperature is set to the temperature controller, the measurement routine stops for the time-span given by *TempStab* before starting the measurement.
- *FieldCurr [A]* sets the current, which is passed through the magnet.
- *NpC* is the number of measurements, which are made for each magnetic field. All values are saved to the *CompleteFile*, but only the medium value is stored in the measurement *File*.
- *CpM* is a relict of previous programming work. It must be set to 1, otherwise the program does not work.
- *Current [A]* gives the measurement current, which is sent through the sample.
- *Umpolungen* gives the number of measurement cycles at each temperature. A cycle consists of one measurement at positive, one at negative magnetic field and one without field.
- *Settle [s]:* gives the delay time between switching on the current and measuring the voltage.
- *ScaleCH1* sets the range of the nanovoltmeter.
- The program needs a file (*TempFile*), which contains a list of temperatures. The data used for the analysis of the magnetoresistance are stored in the *File*; the *CompleteFile* contains more details.

- It is possible to write a comment to the file.
- *Control Heater Range:* There is an option that allows the program to control the power range of the heater number one. For low temperatures the range is normally set to a power of 250 mW. If more than 80 % (*Heater-Output*) of the 250 W are needed to hold the temperature at a constant level, the heater range is changed automatically to a power of 2.5 W (*Heater-Range* 4).
- *SetTemp* gives the temperature setpoint (from *TempFile*), *Temp. A [K]* shows the temperature at the sample (RhFe sensor) and *Temp. B [K]* that at the cold head. *Field [A]* shows the current passing through the magnet and *SetField[V]* the voltage, which is used to control the magnet.
- *Graph_p* shows the resistance measured in the positive magnetic field, *Graph_n* that with the field in the opposite direction and *Graph_z* the resistance without field. *Graph_MR* shows the magnetoresistance $R(B) - R(0)$ in Ohms (with $R(B)$ the resistance with and $R(0)$ that without magnetic field).

Function of the program
When the *Start* button is switched on, the following routine is executed:

(1) The temperature is set to the first value in the *TempFile*. The temperature at the cold head is set to a temperature lower by *TempDiff* K.

(2) The program pauses for the time set by *TempStab*.

(3) The current through the magnet is ramped to the value given by *FieldCurrent*. This action is followed by a delay of three minutes.

(4) The resistance is measured *NpC* times (as described in section 5.1). The medium value is calculated and plotted to *Graph_p*.

(5) The current through the magnet is ramped down to zero. This action is followed by a delay of three minutes.

(6) The temperature of the sensors A and B is requested from the temperature controller.

(7) The resistance is measured *NpC* times. The medium value is calculated and plotted to *Graph_z*.

(8) The current through the magnet is ramped to the negative value of *FieldCurrent*. This action is followed by a delay of three minutes.

(9) The resistance is measured *NpC* times. The medium value is calculated and plotted to *Graph_n*.

(10) The current through the magnet is ramped down to zero.

(11) The magnetoresistance is calculated and plotted to *Graph_MR*. The measured values are stored in the *File*.

The steps 3 - 11 are repeated n times with n the parameter given for *Umpolungen*. Then the setpoint of the temperature controller is set to the next temperature of the *TempFile* and the process starts again from step 1.
The measurement stops when all values in the *TempFile* have been used or the *Start* button is switched off.

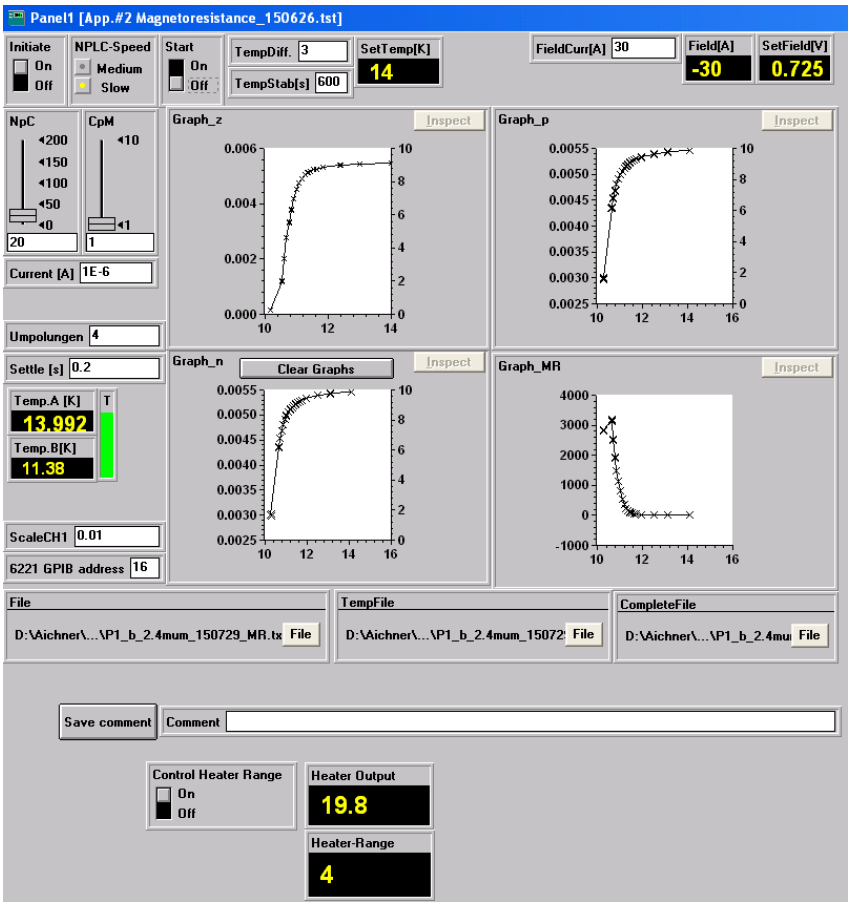

Figure 14: Screenshot of the measurement program used for measurements of the magnetoresistance.

5.3 Current-voltage-characteristics

For these measurements the samples were cooled by liquid helium and the stick was pushed in that much that the sample was totally covered by liquid helium. Thus the voltage was measured as a function of the current at the constant temperature of 4.2 K. The current is raised by multiplication with a constant factor and for each current the voltage at the sample is determined. The program used for this measurement is shown in figure 15.

Description of the program

- *Show T:* If this switch is ON, the resistance of the RhFe sensor is measured every second and the temperature is calculated. This is only used before the measurement is started to check if the sample is in the liquid helium.
- *Measure* starts the measurement routine.
- *I-Start [A]* sets the start current.
- *I-max [A]* sets a current limit; when this current is reached, the measurement is interrupted and the current source is switched off.
- *U-max [V]* sets a voltage limit, at which the measurement is stopped.
- *Multiplication-Factor:* The new current is calculated by multiplying the previous current with this Multiplication-Factor.

- *Settle-Time:* Time span between sending the current and measuring the voltage.
- *Average V readings:* determines how many voltage readings are used to find an average value for each current.
- *Waiting time:* Delay between the measurements at one current and that at the next one.

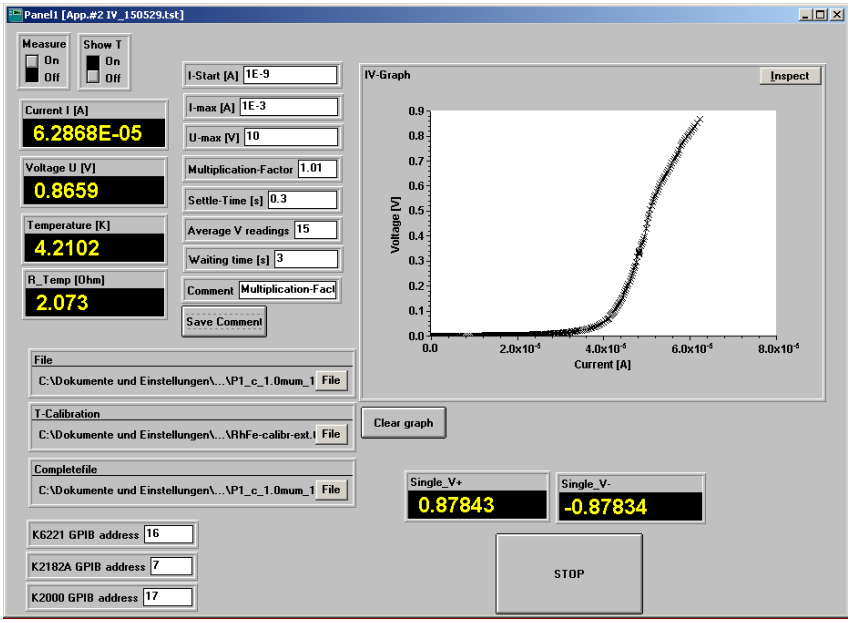

Figure 15: Screenshot of the measurement program used for determining the IV-characteristics.

Function of the program

When the *Measure* switch is set to ON, the following routine is executed.

(1) The calibration data for the RhFe sensor are loaded from the *T-Calibration* file.

(2) The current *I-Start* is sent through the specimen. Then the routine pauses for the time-span set as *Settle-Time*.

(3) The voltage *Single_V+* and the resistance of the RhFe sensor are measured; the values are saved to the *Completefile*.

(4) The same current is sent through the sample in the opposite direction, the routine is paused for the time-span set as *Settle-Time*.

(5) The voltage *Single_V-* and the resistance of the RhFe sensor are measured; the values are saved to the *Completefile*.

(6) The steps 2 - 5 are repeated n times with n the parameter given in *Average V readings*. Then the mean value of the voltage and of the temperature are calculated, plotted to the graph and stored in the *File*.

(7) The routine pauses for the time-span set as *Waiting time*.

(8) The new current is calculated as the previous used current times the *Multiplication-Factor*. If this new current is higher than the highest allowed current set by *I-max* or the voltage calculated in step 7 is higher than *U-max*, the routine is stopped. Otherwise it begins at step 1 with the new current instead of *Start-I*.

5.4 Critical current versus temperature

In these measurements the critical current I_c shall be determined as a function of temperature. Therefore it is necessary to register IV-curves as described in the previous section at different temperatures. The critical current is then defined as the current, at which a voltage- or resistance-criterion is fulfilled, which means that the measured voltage or resistance (at this current) is higher than that fixed in the criterion. Since in the helium dewar it is not possible to hold the sample at a constant temperature for more than some seconds, it is important to make the measurement as fast as possible. Therefore the current source is connected to the voltmeter via a *TriggerLink* cable and operated in the sweep-mode, which means that a sweep is programmed at the beginning of each measurement and each time after the voltmeter has done a measurement the current source automatically sends the next current without help of the computer. The temperature is varied by slowly pulling the stick out of the liquid helium. The temperature is measured at each point of the IV-curve. Thus also if temperature changes during the registration of one IV-curve, it's value at the point, where the sweep is interrupted, is exact.
The program used for this measurement is shown in figure 16.

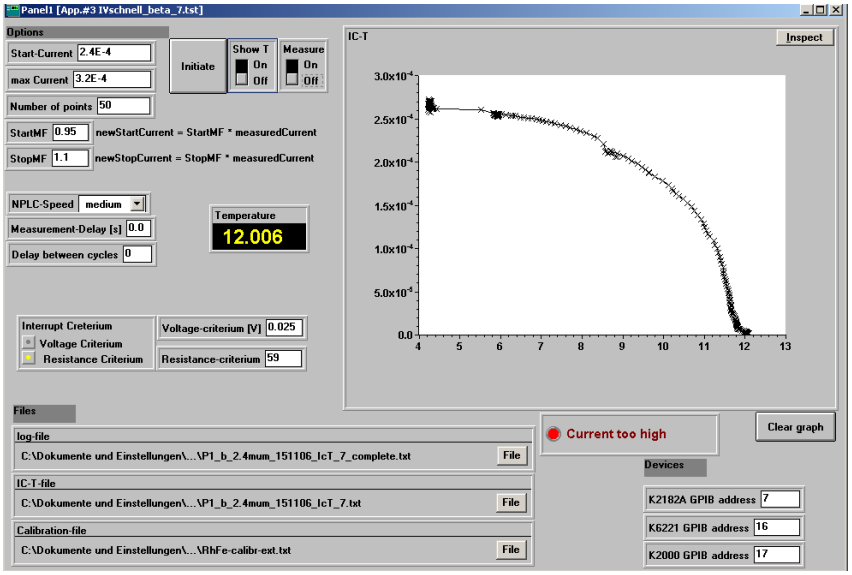

Figure 16: Screenshot of the measurement program used for determining the temperature-dependence of the critical current.

Function of the program

When the *Initiate*-button is pressed, the calibration-data for the RhFe sensor are loaded from the *Calibration-file*.
When *Measure* is switched on, the following routine is executed:

(1) The settings for the integration time (NPLC-speed) are transferred to the voltmeter. The current source is configured for being triggered by the *TriggerLink* cable.

(2) The current source is configured for a logarithmic sweep. The *Start-Current*, the stop-current (*Start-Current* times *StopMF*) and the *Number of points* between start- and stop-current are transferred to the current source. If the stop-current is higher than the *max Current*, the measurement is interrupted, otherwise the current is switched on.

(3) The voltage is measured. The current source automatically rises the current. The sample resistance is calculated.

(4) The resistance of the RhFe sensor is measured and the temperature is calculated. The values are stored in the *log-file*.

(5) The routine pauses for the time-span specified as *Measurement-Delay*.

(6) The steps 3 and 4 are repeated until the measured voltage or the resistance fulfils the voltage- or resistance-criterion, respectively. When the criterion is fulfilled, current and temperature are stored in the *IC-T-file* and plotted to the graph.

(7) A new start current is calculated by multiplying the old value by *StartMF*. After the *Delay between cycles* the steps 2 - 5 are repeated with the new start current.

This routine is repeated until the *Measure* switch is set to OFF.

The **parameters** to set in this program are:

- *Start-Current:* The first current, which is sent through the sample at the start of the measurement.
- *max Current* gives an upper limit for the current, which should prevent that samples are destroyed during the measurements.
- *Number of points* sets the number of points in the logarithmic staircase sweep between the selected start current and the stop current. A high number of points makes the measurement more precise, but it slows it down, which leads to problems of the temperature stability.
- *StartMF:* The new start current for each sweep is calculated by multiplying the previous start current by *StartMF*.
- *StopMF:* The stop current for each sweep is calculated by multiplying the start current by *StopMF*.
- *NPLC-speed* determines the integration time of the nanovoltmeter.
- *Measurement-delay:* Delay between the single measurements.
- *Deley between cycles:* Delay between the interruption and the beginning of the next sweep.
- *Interrupt-criterion:* The user must choose if he wants to use a voltage or a resistance as interrupt criterion and give a value for this criterion.

6 The samples

The samples used for the measurements presented in this thesis were prepared by the group around Wojciech Słysz at the Institute of Electron Technology in Warsaw, Poland.
Two types of samples were used, thin superconducting (S) films and superconductor/ferromagnet (S/F) bilayers. Two different superconducting alloys, NbTiN and NbN, were used. The ferromagnetic layer is constituted by a NiCu alloy (54% Ni and 46 % Cu)[57]. Two sets of samples with different geometries were used in this thesis.

(1) The first set consisted of four samples:

- NbTiN (with RTA[5])
- NbTiN/NiCu (with RTA)
- NbN (with RTA)
- NbN/NiCu (with RTA)

(2) The second set consisted of four samples, too:

- NbN (without RTA)
- NbN/NiCu (without RTA)
- NbN (with RTA)
- NbN/NiCu (with RTA)

Since the samples were prepared by another group, only a brief description of the preparation process will be given here, following the references [58], [59] and [55].

6.1 The sample preparation process

The NbN and NbTiN samples were produced by high-temperature reactive RF sputtering. For this purpose metallic Nb and Ti targets were used and the sputtering process was done in a $N_2 - Ar$ atmosphere at a pressure of 8 μbar. The sapphire substrates were kept at a temperature of 850 $^\circ$C during the sputtering process. The film thickness was controlled via the deposition time. To enhance the superconducting properties the samples were annealed in Ar atmosphere at 1000 $^\circ$C for ten minutes (except two samples of the second set). After annealing a NiCu layer was deposited on some samples by dc magnetron sputtering in Ar atmosphere at room-temperature. The overall process took place in the same system without breaking vacuum to avoid oxidation.
For the transport measurements the superconducting films were patterned into stripes by photolitography. For electrical contact four gold pads were deposited on top of each stripe, which means that for the S/F bilayers the contacts are on the F layer and not directly on the superconductor. For the first set of samples the substrates were glued onto epoxy plates. The thickness was controlled by the deposition time, length and width by the mask used for photo-etching.

[5] Rapid Thermal Annealing, see text

6.2 The first set of samples

6.2.1 Sample geometry

Overview pictures of all samples can be found in appendix C. The pictures were taken with the optical microscope. In the appendix also schematic pictures of the samples are given.
The nominal length of all stripes is $l = 30\ \mu$m, while stripes with different width were prepared. The nominal dimensions of the stripes are listed in table 2. The thickness was controlled by the deposition time, length and width by the mask used for photo-etching. The numbers near the single stripes (see photographs in the appendix) denote their nominal width.
One superconducting stripe of the first set of samples is shown in figure 17.

Figure 17: Photograph and scheme of one superconducting stripe of the first set of samples.

This photograph is dominated by the gold contacts. The bigger ones are the current-contacts, the smaller ones are used to measure voltage. Between the contacts one can see the superconductor, which has a narrow part at it's center. This narrow stripe, which is the interesting part of the sample, is shown in detail in figure 18a. This image, taken by a scanning electron microscope (for further information see section 6.2.2) shows the narrow superconducting stripe and it's broadening at the ends. The black spots are caused by dirt on the sample, probably by vacuum grease, which was used to provide thermal contact of the sample during transport measurements. A schematic picture of this central part of the samples is shown in figure 18b.

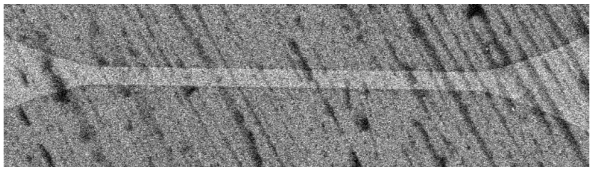

(a) SEM image of the NbN stripe with nominal width $w_N = 1.6\ \mu$m.

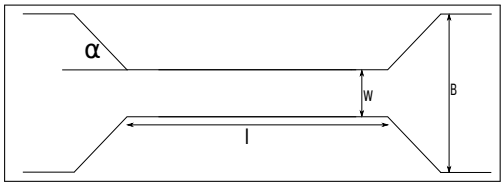

(b) Geometry of the central part of one single stripe.

Figure 18: The central part of the superconducting stripe: photograph and schematic picture

SEM images were used to determine the real length and width (values in chapter 6.2.2). Note that not all stripes have electrical contact, therefore in table 2 only the working stripes are listed.

Sample	**Label from IET**	w_N	l_N	t_S	t_F
		μm	μm	nm	nm
NbTiN	NbTiN14w	0.6, 1.2, 1.6, 2.4	30	3.9	-
NbTiN/NiCu	NTN17w_NC3	0.8, 1, 1.6	30	7	6
NbN	NbN27w	0.6, 0.8, 1.2, 1.6, 2.4	30	4.8	-
NbN/NiCu	NbN30w_NC3	0.8, 2.4	30	6	6

Table 2: Nominal data, name and geometries as reported from the *Institute of Electron Technology* (IET). w_N and l_N denote the strip's nominal width and length, respectively, t_S is the thickness of the superconducting and t_F the thickness of the ferromagnetic layer.

6.2.2 Scanning electron microscopy (SEM)

The four samples were examined in a scanning electron microscope (SEM) at the Faculty Center for Nanostructure Research of the University of Vienna by Mag. Dr. Stephan Puchegger. An image of every working stripe of the samples was taken, the image for the stripe with nominal width $w_N = 1.6$ μm of the NbN sample is shown in figure 18a.
Figure 19 shows SEM images of the NbTiN sample; in figure 19b the 0.8 μm stripe is shown. One can clearly see that at the right end of the stripe there is an imperfection, which was probably produced in the etching process. The stripe could not be used for transport measurements because there is no electrical contact across the sample. Probably this is caused by the above-mentioned imperfection.

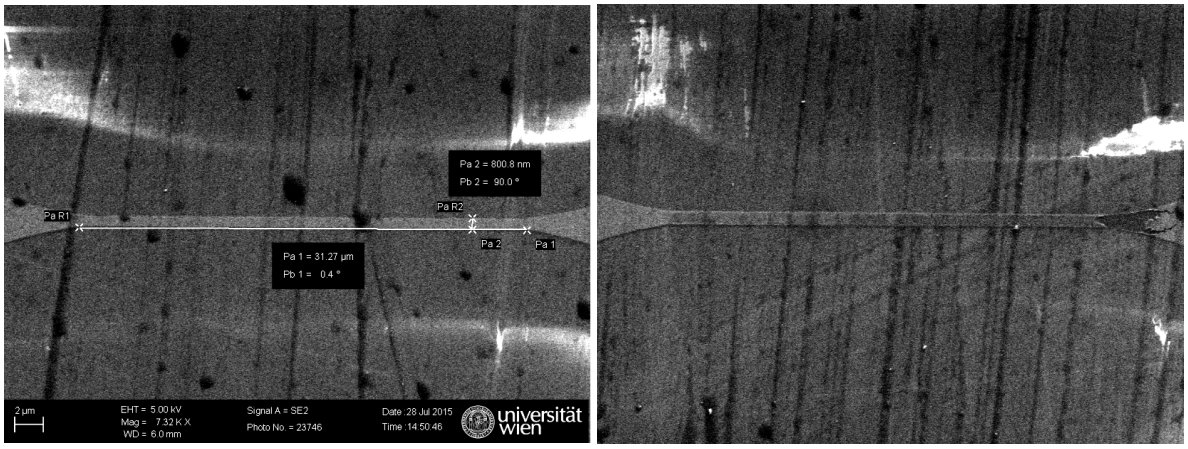

(a) SEM image: NbTiN, $w_N = 0.6$ μm. (b) SEM image: NbTiN, $w_N = 0.8$ μm.

Figure 19: SEM images of the NbTiN sample. At left a working stripe is shown, the right stripe has no electrical contact and was therefore not used for transport measurements.

The SEM images gave us the possibility to measure the real sample geometry, which varies essentially from the nominal geometry for many samples. The sample geometries measured by SEM are listed in table 3. For the measurements only the length of the thin stripe without the trapezoid-shaped ends was considered (see figure 19a), because the thin parts have the biggest contribution to the resistance. The angle is defined in figure 18b. It was very difficult to determine values for the angle because all stripes have a different form.

For the analysis of the transport measurements it is often necessary to calculate a sample's resistivity $\rho = R \cdot wd/l = R \cdot \mathrm{GF}$ (with R the resistance, w the width and l the length of the sample). Therefore a geometry factor

$$\mathrm{GF} = \frac{wd}{l} \tag{24}$$

is defined. The last column of table 3 shows the fraction of the geometry factors calculated from SEM data and from nominal data. This factor shows, how much influence the deviation of the nominal data has on the measurement results. In the further analysis all data are scaled with the geometry factor calculated from SEM data.

	Nominal values			Measured by SEM		
Material	**Length**	**Width**	**Thickness**	**Length**	**Width**	$\mathbf{GF}_{SEM}/\mathbf{GF}_N$
	[μm]	[μm]	[nm]	[μm]	[μm]	
NbTiN	30	0.6	3.9	31.3	0.708	1.13
	30	1.2	3.9	34.9	1.5	1.07
	30	1.6	3.9	36.7	2	1.02
	30	2.4	3.9	40	2.7	0.84
NbTiN/NiCu	30	0.8	7+6	31.7	0.25	0.3
	30	1	7+6	33	0.5	0.46
	30	1.6	7+6	37	1.2	0.61
NbN	30	0.6	4.8	31	0.411	0.66
	30	0.8	4.8	33.16	0.715	0.81
	30	1.2	4.8	35	1.24	0.89
	30	1.6	4.8	38.44	1.7	0.83
	30	2.4	4.8	40	2.6	0.81
NbN/NiCu	30	0.8	6+6	31.43	0.15	0.18
	30	2.4	6+6	40.47	1.8	0.56

Table 3: Sample geometries, nominal data and SEM-measurements. Two values are given for the thickness for S/F bilayers; the first corresponds to the superconductor, the second to the ferromagnet. Length and width have been determined as is shown in figure 19a. The relation of the geometry factors GF= wd/l, calculated from nominal and from SEM data, is given in the last column.

6.2.3 Estimation of further geometric influences

In figure 17 we see the geometry of one single stripe of the NbN sample. It consists of two broad stripes at the sides and a narrow one in the middle. Since the resistance scales inverse with the width, the central part, which consists of the narrow stripe, will give the main contribution. An additional influence is given by the trapezoid-shaped parts, which constitute the transition of the narrow to the broad part. This influence shall be estimated here. For the calculation the abbreviations shown in the figures 18b and 20 are used.
For this estimation the trapezoid-shaped parts are divided in slices of length Δl and approximated by rectangles (see figure 20). From geometrical considerations we get $h_1 = \Delta l/2 \cdot \tan(\alpha)$. The width H_1 of the first slice is therefore given by $H_1 = w + 2h = w + \Delta l \cdot \tan(\alpha)$. The width of all further slices is calculated analogously, we only have to replace $1/2\Delta l$ by $3/2\Delta l$ for H_2, by $5/2\Delta l$ for H_3 and so on.

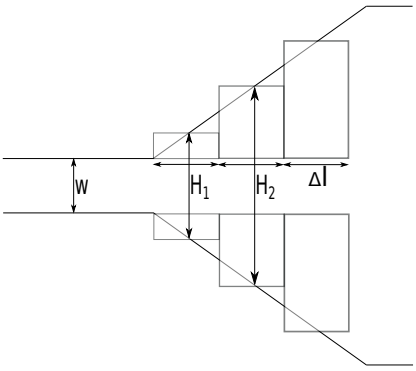

Figure 20: Scheme of the approximation.

Thus a generalized form of the slice hight H_n can be found:

$$\begin{aligned} H_0 &= w && (n = 0) \\ H_n &= w + (2n-1)\Delta l \tan(\alpha) && (n > 0) \end{aligned} \tag{25}$$

With the formula for the resistivity $R = \frac{\rho l}{wd}$ the resistance R_{ges} can be calculated:

$$\begin{aligned} R_{ges} &= \frac{\rho l}{wd} + 2\frac{\rho \Delta l}{d(w + \Delta l \tan(\alpha))} + 2\frac{\rho \Delta l}{d(w + 3\Delta l \tan(\alpha))} + ... \\ &= \frac{\rho}{d}\left[\frac{l}{w} + 2\frac{1}{w/\Delta l + \tan(\alpha))} + 2\frac{1}{w/\Delta l + 3\tan(\alpha))} + ...\right] \\ &= \frac{\rho}{d}\left[\frac{l}{w} + \sum_{k=1,3,5...} \frac{1}{w/\Delta l + k\tan(\alpha)}\right] \\ &= \frac{\rho}{d}\left[\frac{l}{w} + \sum_{n} \frac{1}{w/\Delta l + (2n-1)\tan(\alpha)}\right] \end{aligned} \tag{26}$$

The factor 2 stems from the fact that there is such a trapezoid-shaped part on both ends of the narrow superconducting stripe.

Now we want to calculate an effective length l_{eff}, which includes this additional resistance. We can calculate $l_{eff} = \frac{wdR_{ges}}{\rho}$ from equation 26 (keep in mind that $R = \frac{\rho l}{wd}$):

$$l_{eff} = l + 2w \sum_{n} \frac{1}{w/\Delta l + (2n-1)\tan(\alpha)} \tag{27}$$

A calculation was performed with the following data, which seem realistic for the samples.
$\alpha = 15^\circ$
$l = 30\ \mu$m
$w = 1.5\ \mu$m
$\Delta l = 500$ nm
The angle α was measured in the SEM images, but it had a big variation. Therefore for this simple approximation the value of $\alpha = 15^\circ$ was chosen. d and ρ are not needed for the calculation of the effective length. To get values for the resistance, they were set to $d = \rho = 1$ for simplicity reasons. The results of this calculation are listed in table 4. It seems reasonable to take the contributions up to $H_n \approx 10\mu m$ in consideration, which corresponds to $n = 16$. Therefore we get a correction term $l_{eff}/l \approx 1.17$.
Surprisingly the fits in the further analysis are much better if we do not take this effect in consideration. Therefore for the further analysis the value derived from SEM measurements is used for the length l and not l_{eff}.

n	H_n [nm]	l_n [nm]	R_{ges} [a.u.]	l_{eff} [nm]	l_{eff}/l
0	1500	30000	20.00	30000	1.00
1	1789	31000	20.56	30839	1.03
2	2366	32000	20.98	31473	1.05
3	2943	33000	21.32	31982	1.07
4	3521	34000	21.61	32408	1.08
5	4098	35000	21.85	32774	1.09
6	4675	36000	22.06	33095	1.10
7	5253	37000	22.25	33381	1.11
8	5830	38000	22.43	33638	1.12
9	6407	39000	22.58	33872	1.13
10	6985	40000	22.72	34087	1.14
11	7562	41000	22.86	34285	1.14
12	8140	42000	22.98	34469	1.15
13	8717	43000	23.09	34642	1.15
14	9294	44000	23.20	34803	1.16
15	9872	45000	23.30	34955	1.17
16	10449	46000	23.40	35098	1.17
17	11026	47000	23.49	35234	1.17
18	11604	48000	23.58	35364	1.18
19	12181	49000	23.66	35487	1.18
20	12758	50000	23.74	35604	1.19

Table 4: Estimation of the influence of the trapezoid-shaped parts on the sample resistance. n is the summation index, $l_n = l + 2n\Delta l$ denotes the length taken in consideration after the n-th step and H_n the height of the n-th rectangle. Note that R_{ges} has no physical meaning, because for the calculation $\rho = d = 1$ has been used. l_{eff} has been calculated by equation 27.

6.3 The second set of samples

The second set of samples was used to determine the influence of the RTA process. For two of the samples the RTA step in the preparation process was skipped.
For the preparation of this set of samples a different mask was used. The shape can be seen in figure 21.
The nominal length of the stripes is $l_N = 2.8$ mm. Measurements with a *Zeiss Axioplan* optical microscope pointed out that in reality the stripes are shorter. Five stripes on different samples were measured and the stripe length was calculated as $w_{measured} = (2.769 \pm 0.004)$ mm. Two different strip widths were used, namely $w_N = 4$ μm and w_N =12 μm. As far as it is possible to determine the width by optical microscopy, the real strip width corresponds to the nominal width. The thickness of the superconducting layer is $t_S = 4.2$ nm, the ferromagnetic layer is $t_F = 3.5$ nm thick.
Analogously to the other set, the bigger contacts were used as current contacts, the smaller ones to measure voltage. Photographs and schematic pictures of the samples can be seen in appendix C.

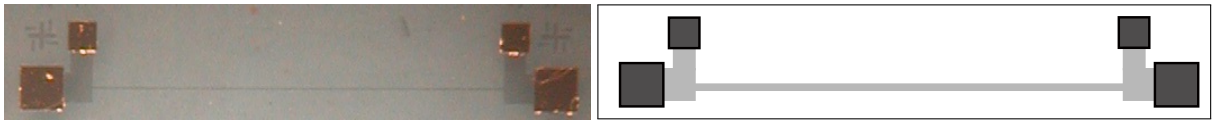

Figure 21: Photograph and scheme of one superconducting stripe of the second set of samples.

Sample	**Label from IET**	w_N	l_N	t_S	t_F
		μm	μm	nm	nm
NbN	Nb32w	4, 12	2800	4.2	-
NbN/NiCu	Nb32wNC	4, 12	2800	4.2	3.5
NbN (without RTA)	Nb32	4, 12	2800	4.2	-
NbN/NiCu (without RTA)	Nb32NC	4, 12	2800	4.2	3.5

Table 5: Nominal data of the sample geometry and label from IET. w_N and l_N denote the strip's nominal width and length, respectively, t_S is the thickness of the superconducting and t_F the thickness of the ferromagnetic layer.

7 Results

7.1 Temperature-dependence of the resistance

The temperature dependence of the resistance has been investigated. For this purpose measurements in the He-dewar were performed. The temperature was varied by altering the distance of the dip-stick to the surface of the liquid helium. Although this is quite a simple arrangement, we got good results.
However there is an uncertainty in the temperature-measurement. Figure 22a shows that it makes a difference if one measures from high to low or from low to high temperatures (which corresponds to lowering the stick in the He-dewar or pulling it out). This shows that the sample and the temperature sensor are not in thermal equilibrium, which leads to a shift of the temperature between the two measurements (stick down and up) of about 0.2 K. It does not seem to make sense to determine an exact value for this shift, because the thermal equilibrium of sample and sensor may depend on multiple parameters: First of all on the thermal conductance of the specimen, but further on how fast the temperature is varied and on the helium pressure in the dewar. Therefore it can be different for every measurement. To avoid this systematic error, all measurements except the $I_c(T)$-measurements were performed at falling temperatures.
For determining the critical temperature T_c the midpoint of the transition was chosen. Therefore the medium resistance $R_{med} = R_S + (R_N - R_S)/2$ (with R_N the resistance above the superconducting transition and R_S the resistance in the superconducting region) was calculated and the temperature, at which the sample showed this resistance R_{med} was chosen as T_c (see figure 22b). For an ideal superconductor R_S would be zero, however for some of the samples a residual resistance in the "superconducting" region was observed.

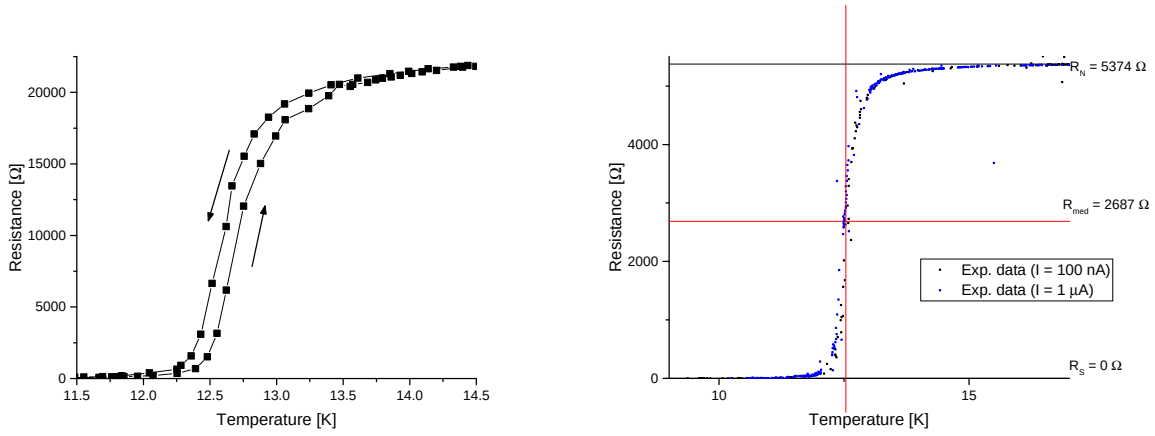

(a) Shift in T

(b) Determination of T_c

Figure 22: Figure a) shows the shift of the temperature between the measurement with lowering and with rising the stick. It resulted to be in the range of 0.2 K. The 0.6 μm stripe of the NbTiN sample was examined. Figure b) illustrates how the critical temperature T_c was determined. The measurement data are that of the 2.4 μm stripe of NbN/NiCu. Two measurements with two different currents ($I = 100$nA and $I = 1$ μA) were used.

The temperature-dependence of the resistance for all annealed samples is shown in figure 24. The measurement data are normalized to the resistance at $T = 20$ K. The values for the resistance at 20 K of each sample were determined from the measurement data (obtained in the He-dewar) by linear interpolation. They are given in table 6. For most of them the experimental data are quite good, which allowed to determine the resistance with an accuracy of ± 30 Ω, for the NbN 2.4 μm stripe and the NbTiN/NiCu 0.8 μm stripe a much

higher uncertainty of estimative ±150 Ω has been received. For the NbN sample without RTA the uncertainty is about 5 kΩ for the 4 μm stripe and about 200 Ω for that with $w_N = 12$ μm.

Regarding the results for NbTiN (figure 24a) one can see that the S/F bilayers have a broader transition than the pure S samples. Furthermore the transition temperature (defined as described before) is lower for the bilayers, but the onset of the transition of the NbTiN 2.4 μm stripe is in the range of that of the bilayers. The NbTiN/NiCu bilayers with nominal width $w_N = 0.8$ μm and $w_N = 1.0$ μm show a residual resistance R_S in the "superconducting" region, which is most pronounced for the narrowest stripe (with about 4 kΩ at T = 5 K).

The NbN sample of the first set exhibits a very low T_c, which is much lower than that of the NbN/NiCu bilayers. The thinnest stripe of this NbN sample shows an even lower transition temperature than the other ones, therefore in this stripe superconductivity is not fully established at the lowest measurement-temperature of $T = 4.2$ K. The NbN/NiCu bilayer with nominal width $w_N = 0.8$ μm shows a residual resistance of about 100 Ω at 5 K, whereas no residual resistance could be observed for the broad stripe. All samples of the second set become fully superconducting, the 4 μm strip of the NbN sample without RTA is the only measured strip, which has a residual resistance of about 20 Ω at 4.2 K.
Figure 23a shows a comparison of the specimens of the second set of samples. It is remarkable that the samples, which were produced without RTA, have a much lower transition temperature than these with RTA.
For the NbN sample, which was prepared without RTA, two stripes with different width have been measured (see figure 23b) and surprisingly the broader (12 μm) stripe has a lower transition temperature than the 4 μm stripe.

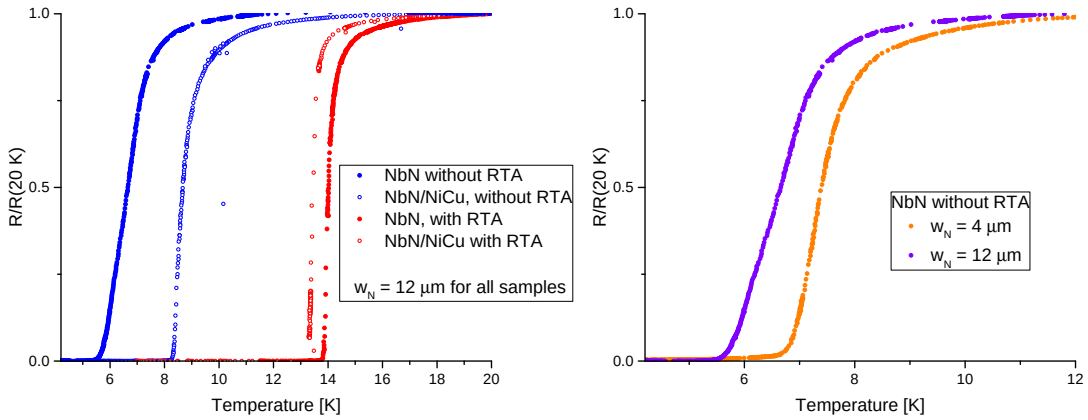

(a) Comparison of the samples (b) Comparison of two stripes with different width

Figure 23: Temperature-dependence of the resistance: Open symbols represent the measurements for the S/F bilayers. w_N denotes the nominal stripe width. All measurements were performed in the He-dewar at falling temperatures. The measurement current was $I = 1$ μA.

Additional to the measurements in the helium dewar, measurements in the closed-cycle cryostat were performed. The samples were cooled down from 300 K to about 9 K at a rate of 0.3 K/min. During the cooling process the resistance was measured in intervals of about 1.5 seconds. The measurements in the closed-cycle cryostat showed a shift in the temperature of up to 3 K relative to the measurements in the He-dewar. This big shift in temperature may be caused by the bad heat conductance from the measurement device in the closed-cycle cryostat to the sample. In the closed cycle cryostat the copper-block is cooled and the temperature in this block is measured. However the sample is situated on

an additional copper-layer (the sample-holder), which is thermally connected to the copper block by a cryogenic high-vacuum grease (*Apiezon*). Between the temperature sensor and the superconducting material therefore there is a sandwich consisting of the cooper-block, a layer of Apiezon, the sample-holder, an other layer of Apiezon, the epoxy-layer, on which the sample is glued, and the substrate. Even though cryogenic high-vacuum grease was used for better thermal conductivity, each transition is a barrier for heat conductance. Especially the epoxy-layer, which has a thickness of nearly 1 mm is thought to constitute a relevant barrier for heat conductance. Therefore it seems plausible that the sample temperature is by some Kelvin higher than the temperature of the sensor.
In contrast to this arrangement, in the He-dewar the specimen is fixated directly on the copper-block with the temperature sensor in it and it is not in vacuum, but in He atmosphere, which can lead to a much better heat conductance directly to the superconducting strip.
Since the lowest reachable temperature in the closed-cycle apparatus is about 9 K in some of the samples (concerning the shift in temperature of up to 3 K) superconductivity was not fully established.

	Set	**Nominal width**	**R(20 K)**	$\boldsymbol{T_c}$ (He-dewar)
		[μm]	[Ω]	[K]
NbTiN	1	0.6	23004.9	12.7
	1	1.2	14371.9	12.87
	1	1.6	11870.4	12.5
	1	2.4	1755.3	12.45
NbTiN/NiCu	1	0.8	118003	12
	1	1	18107.4	11.85
	1	1.6	8828.8	11.9
NbN (without RTA)	2	4	1037780	7.4
	2	12	343742	6.7
NbN	1	0.6	216401	6.45
	1	0.8	77609.3	8.33
	1	1.2	51616.2	8.4
	1	1.6	41805.0	8.46
	1	2.4	31943	8.55
	2	12	65496.5	14
NbN/NiCu (without RTA)	2	12	185704.3	8.7
NbN/NiCu	1	0.8	40290.1	12.88
	1	2.4	5374.4	12.5
	2	12	3146.4	13.4

Table 6: Parameters determined from resistance versus temperature measurements performed in the He-dewar. Since the two sets of samples have different geometries, it is listed to which set the measured strip belongs.

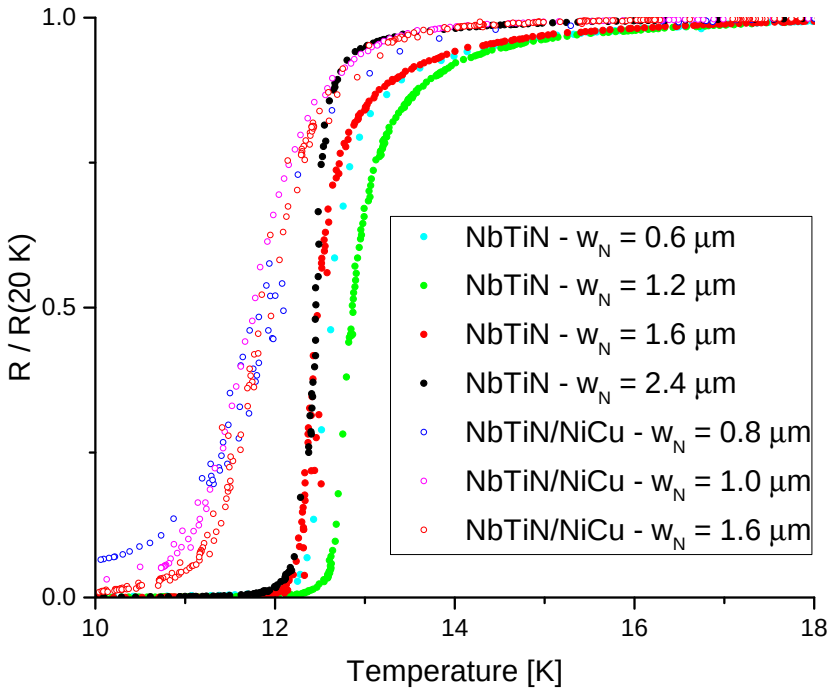

(a) Resistance versus temperature curves of NbTiN

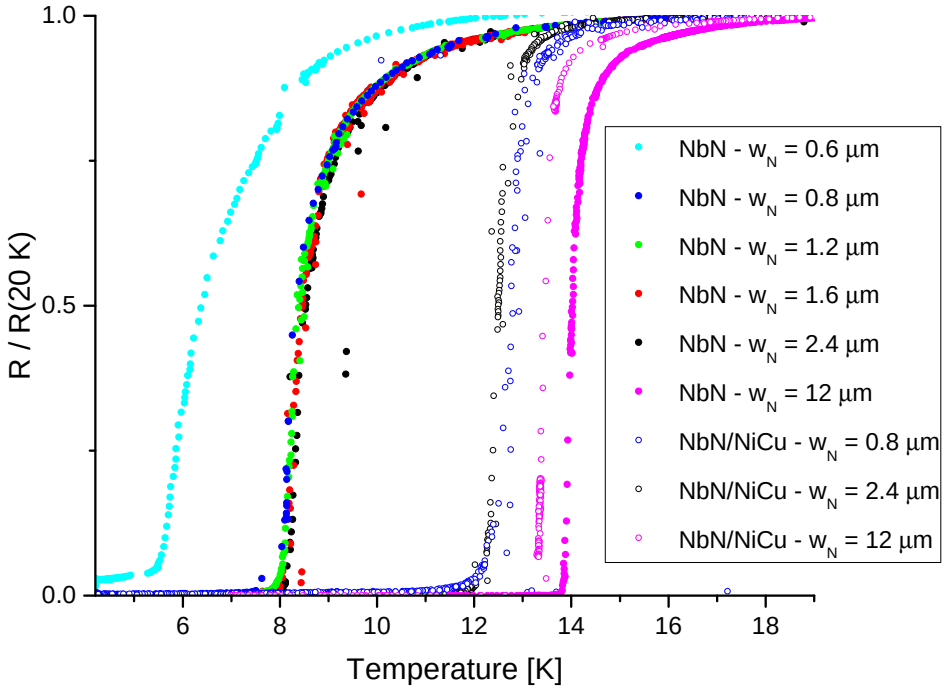

(b) Resistance versus temperature curves of NbN

Figure 24: Temperature-dependence of the resistance. Open symbols represent the measurements for the S/F bilayers. w_N denotes the nominal stripe width. All measurements were performed in the He-dewar at falling temperatures. A measurement current of $I = 100$ nA was used for NbTiN/NiCu 1.6 μm, NbN 1.6 μm, NbN 2.4 μm and NbN/NiCu 0.8 μm and $I = 1$ μA was used for all other measurements.

7.2 Paraconductivity and Magnetoconductivity

Only the first set of samples was used for paraconductivity and magnetoconductivity analysis. For this analysis the measurement data collected in the closed-cycle cryostat were used, except for the NbN sample (because of it's low T_c). The lowest accessible temperature in the closed-cycle apparatus is about 9 K. Therefore in some of the samples (concerning the shift in temperature of up to 3 K) superconductivity was not fully established. Since for the fluctuation analysis the upper part of the transition is the interesting range, this is not a big problem. Also the fact that the absolute temperature measured in the closed-cycle cryostat is not exact should not have an influence on the results of the fluctuation analysis, because only the reduced temperature, thus the ratio of the measured temperature to the critical temperature is of importance for this analysis. Therefore for the analysis of paraconductivity and magnetoconductivity other values for the transition temperature than shown in table 6 were used.
To determine the fluctuation paraconductivity $\Delta\sigma$ the normal resistance was estimated from a plot of the measurement data. The resistivity $\rho = wd/l \cdot R$ and the conductivity $\sigma = 1/\rho$ were calculated from the resistance using the values for the width w and the length l determined by SEM measurements. For the thickness the nominal value was used. Then the paraconductivity was calculated as shown in equation 28.

$$\Delta\sigma = \sigma - \sigma_N = \frac{1}{\rho} - \frac{1}{\rho_N} = \frac{l}{wd}\frac{1}{KF}\left(\frac{1}{R} - \frac{1}{R_N}\right) \tag{28}$$

The factor KF is a correction factor, which normally should be $KF = 1$. During the fitting process for some samples a $KF \neq 1$ was chosen to get a better matching with the theory. Moreover the critical temperature was treated as fitting parameter and varied slightly.
In the graphs shown on the following pages the data plotted with black dots is that with $KF = 1$. For some samples a second plot with an other KF is shown (blue points). The theoretical curves in the graphs show the two-dimensional Aslamazov-Larkin function $\Delta\sigma_{2D}^{AL}$ (equation 13), scaled to the nominal sample thickness.

Magnetoresistance was determined from the measurements in the closed-cycle cryostat at a magnetic field of $B = 0.91$ T or $B = 0.92$ T. The sample's resistance was measured at different temperatures and at each temperature a value for the resistance in the magnetic field $R(B)$ and a value for the resistance without field $R(0)$ was determined. The relative magnetoresistance $\frac{\Delta\rho}{\rho_0} = \frac{\rho(B)-\rho(0)}{\rho(0)}$ was determined from the measurement data. It is shown in figure 25.

The magnetoconductivity was calculated as described in equation 17. It was assumed that no magnetic field was present, when the magnet was switched off. The results of these measurements are plotted in the graphs on the following pages. As for paraconductivity the black dots show the measured data, the blue dots the data multiplied by the correction factor KF. Theoretical curves (Abrahams function) as described in equation 19 are plotted. For the thickness the nominal value was used and the coherence length at zero temperature was adjusted in the way that the curves fit the experimental data.
In all graphs full symbols represent data of S layers and empty symbols that of S/F bilayers.

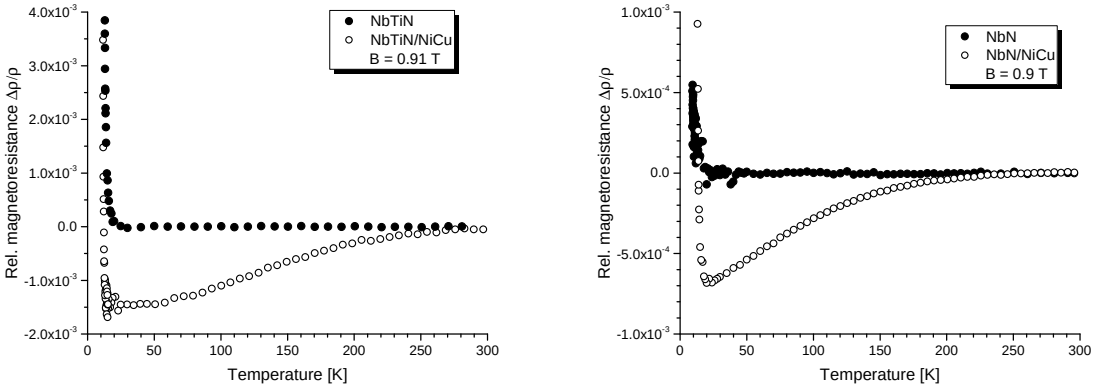

(a) Magnetoresistance of NbTiN and NbTiN/NiCu (b) Magnetoresistance of NbN and NbN/NiCu

Figure 25: Comparison of the relative magnetoresistance of pure S films and S/F bilayers. The nominal strip width was $w_N = 1.6$ μm for NbTiN, NbTiN/NiCu and NbN, but $w_N = 0.8$ μm for NbN/NiCu.

All S/F bilayers exhibit a negative magnetoresistance at temperautes above T_c. That the magnetoresistance is negative means that the conductivity of the sample is higher when a magnetic field is applied. At T_c the superconducting behaviour dominates and the magnetoresistance becomes positive, because the conductivity without field is very high and superconductivity is (at least partially) suppressed in the magnetic field.
For the analysis of the magnetoconductivity, which is shown in the following graphs, all the $\Delta\sigma_B$ curves, which had been obtained for S/F bilayers, were shifted up the way that all values are positive to compensate for the ferromagnet's negative contribution that is not related to superconducting fluctuations.

		Fits with $KF = 1$			Fits with variable KF			
Sample	$\boldsymbol{w_N}$	$\boldsymbol{T_c}$	$\boldsymbol{\xi}$	**Shift of** $\boldsymbol{\Delta\sigma_B}$	$\boldsymbol{KF}$	$\boldsymbol{T_c}$	$\boldsymbol{\xi}$	**Shift of** $\boldsymbol{\Delta\sigma_B}$
	μm	K	nm	$\Omega^{-1}\mathrm{m}^{-1}$		K	nm	$\Omega^{-1}\mathrm{m}^{-1}$
NbTiN	0.8	9.75	5.5		1.77	9.7	4.6	
	1.2	9.7	5.45		1.54	9.6	5	
	1.6	11.05	4.8		1.16	11.05	4.55	
	2.4	11.1 / 10.89	4.9					
NbTiN/NiCu	0.8	10.54	4.3	8	0.63	10.8	3.95	5.5
	1.0	10.77	3.3	740				
	1.6	10.75	3.75	750				
NbN	0.6	5.6			3.02			
	0.8	8.04			1.48			
	1.2	8.15						
	1.6	8.17						
	2.4	8.25						
NbN/NiCu	0.8	11.6	4.5	590	1.45	11.55	3.95	586
	2.4	10.93	4.2	670				

Table 7: Fit parameters of the paraconductivity and magnetoconductivity fits. The parameters were adapted in the way that the measurement data and the theoretical curves correspond to each other. Since this process was only made "by eye", no values for the uncertainty can be given.

7.2.1 NbTiN - Paraconductivity and Magnetoconductivity

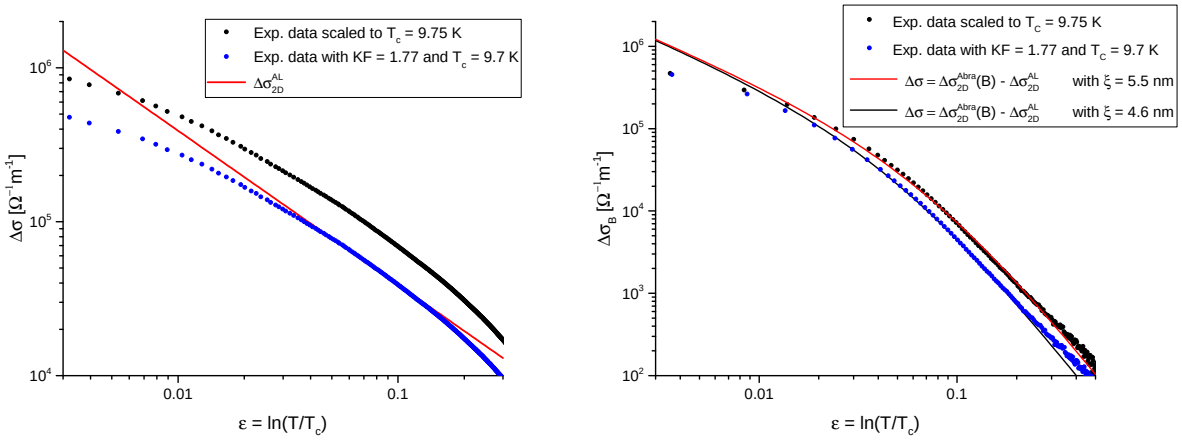

(a) Paraconductivity $\Delta\sigma(\epsilon)$ (b) Magnetoconductivity $\Delta\sigma_B(\epsilon)$

Figure 26: Paraconductivity and Magnetoconductivity of NbTiN (nominal stripe width: 0.6 μm, by SEM $\approx$ 0.7 μm). Note that for the data multiplied by the correction factor KF a different T_c was used. The $KF = 1.77$ relative to the SEM data would correspond to a $KF_n = 2.005$ relative to the nominal data.

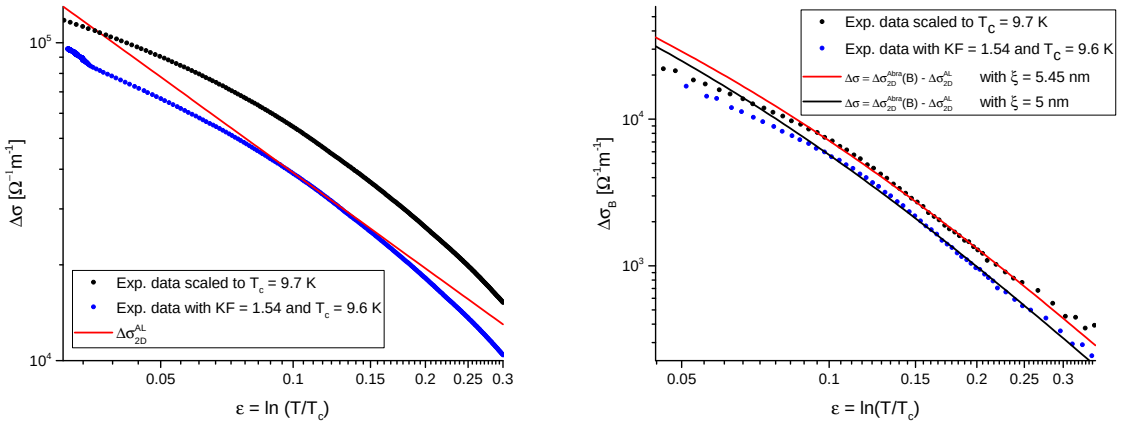

(a) Paraconductivity $\Delta\sigma(\epsilon)$ (b) Magnetoconductivity $\Delta\sigma_B(\epsilon)$

Figure 27: Paraconductivity and Magnetoconductivity of NbTiN (nominal stripe width: 1.2 μm, by SEM $\approx$ 1.5 μm). Note that $T_c = 9.7$ K was used for the fits without and $T_c = 9.6$ K for the fits with the correction factor $KF = 1.54$ (which correspnds to $KF_n = 1.65$ relative to the nominal geometries).

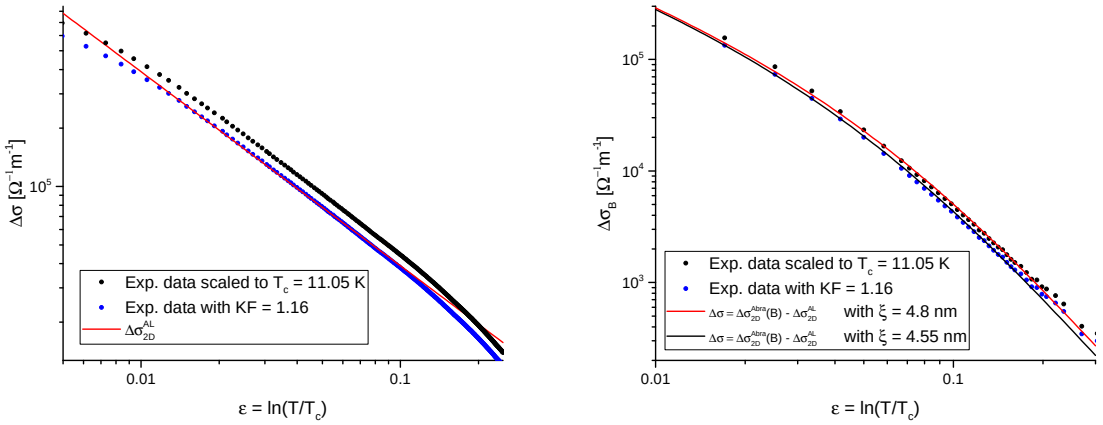

(a) Paraconductivity $\Delta\sigma(\epsilon)$ (b) Magnetoconductivity $\Delta\sigma_B(\epsilon)$

Figure 28: Paraconductivity and Magnetoconductivity of NbTiN (nominal stripe width: 1.6 μm, by SEM $\approx$ 2 μm).

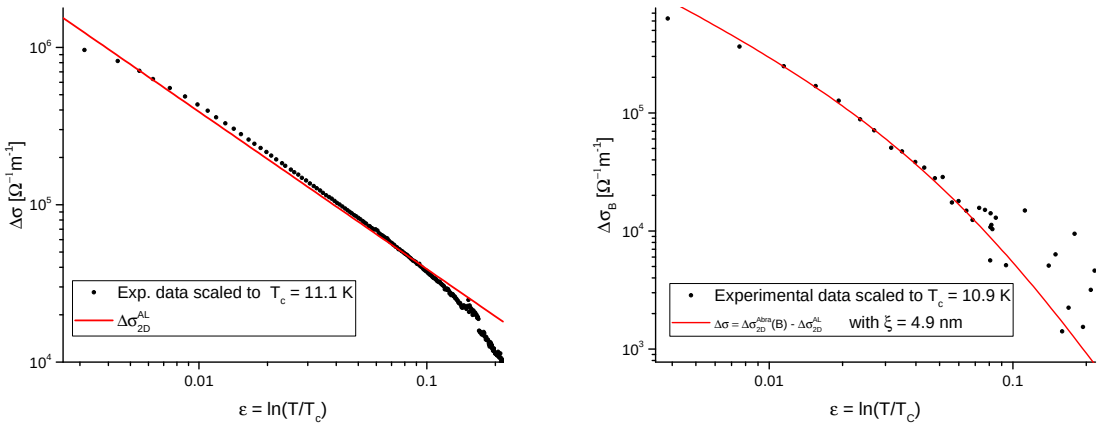

(a) Paraconductivity $\Delta\sigma(\epsilon)$ (b) Magnetoconductivity $\Delta\sigma_B(\epsilon)$

Figure 29: Paraconductivity and Magnetoconductivity of the broadest NbTiN strip with a nominal width of 2.4 μm (and a real width of 2.7 μm according to the SEM measuerement).

For calculation of $\Delta\sigma$ and $\Delta\sigma_B$ SEM data were used. The two measurements of the 2.4 μm-strip used for paraconductivity and magnetoconductivity analysis were performed at different dates and the sample properties had changed in the meantime. Therefore a different T_c had to be used for the evaluation of paraconductivity and magnetoconductivity.
It is remarkable that the broad stripes show a good agreement with theory, whereas for the narrow stripes a correction factor KF has to be used to obtain good fits.

7.2.2 NbTiN/NiCu - Paraconductivity and Magnetoconductivity

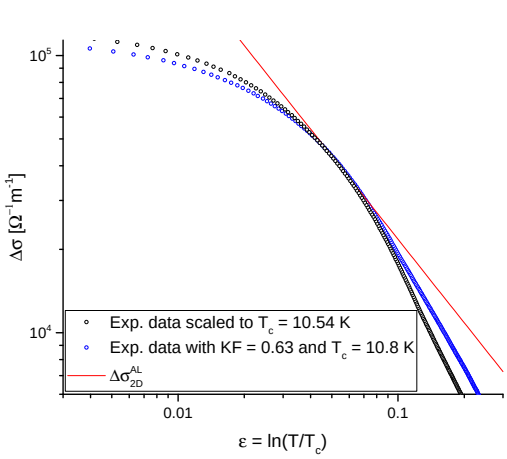

(a) Paraconductivity $\Delta\sigma(\epsilon)$

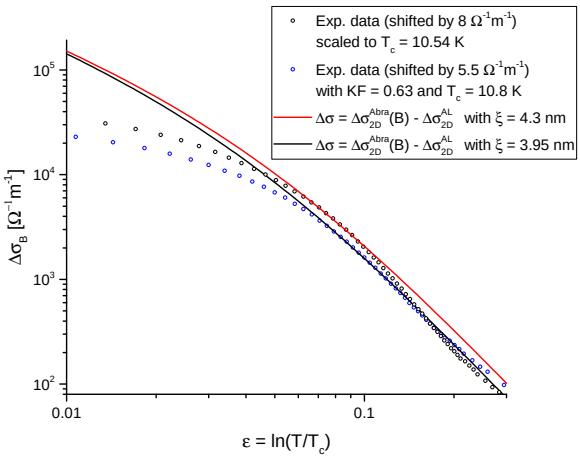

(b) Magnetoconductivity $\Delta\sigma_B(\epsilon)$

Figure 30: Paraconductivity and Magnetoconductivity of NbTiN/NiCu (nominal stripe width: 0.8 μm, by SEM $\approx$ 0.3 μm). The data for $KF = 0.187$ was shifted by 8 $\Omega^{-1}\mathrm{m}^{-1}$, the data with $KF = 0.295$ by 5.5 $\Omega^{-1}\mathrm{m}^{-1}$.

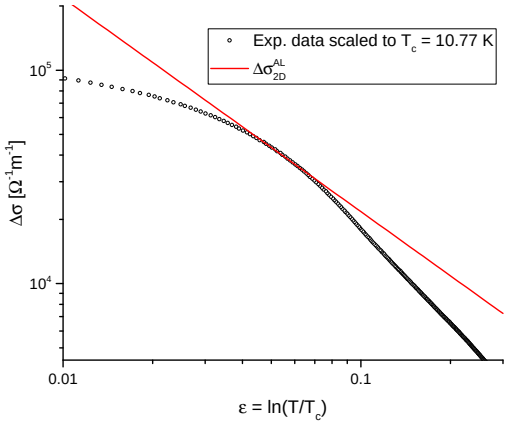

(a) Paraconductivity $\Delta\sigma(\epsilon)$

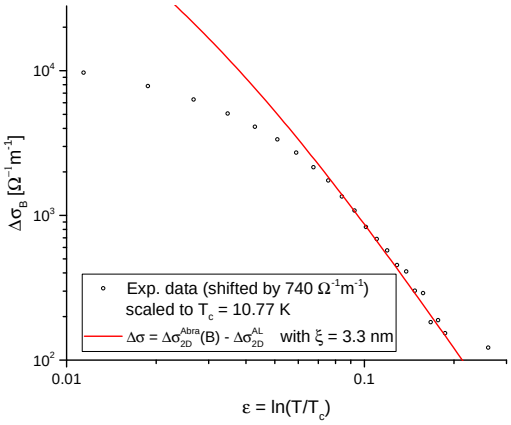

(b) Magnetoconductivity $\Delta\sigma_B(\epsilon)$

Figure 31: Paraconductivity and Magnetoconductivity of NbTiN/NiCu (nominal stripe width: 1.0 μm, by SEM $\approx$ 0.5 μm) as a function of the reduced temperature ϵ. The solid lines represent the fit with the AL-2D function (equation 13) for the paraconductivity and the Abrahams-2D function (equation 19) for the magnetoconductivity, respectively. The data was shifted by 740 $\Omega^{-1}\mathrm{m}^{-1}$.

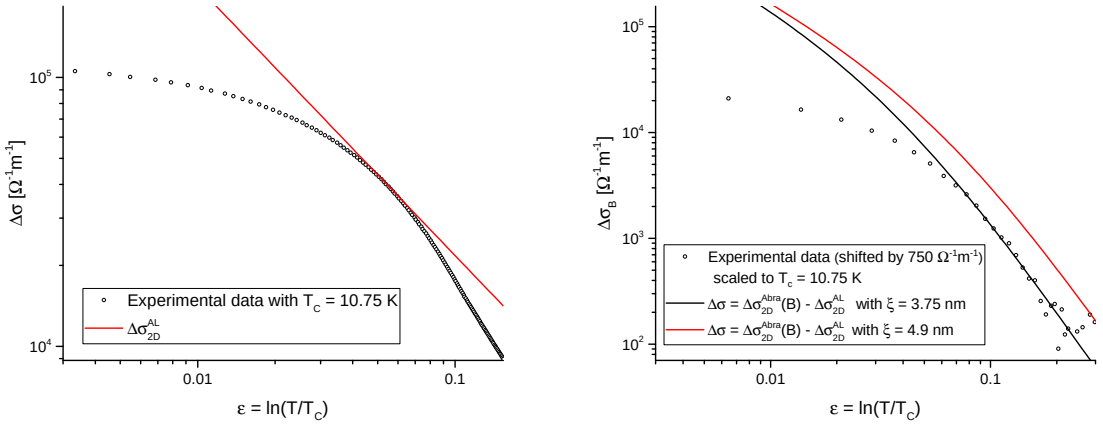

(a) Paraconductivity $\Delta\sigma(\epsilon)$

(b) Magnetoconductivity $\Delta\sigma_B(\epsilon)$

Figure 32: Paraconductivity and Magnetoconductivity of NbTiN/NiCu (nominal strip width: $w = 1.6$ μm, by SEM ≈ 1.2 μm) as a function of the reduced temperature. The measurement data was shifted by 750 $\Omega^{-1}\mathrm{m}^{-1}$.

7.2.3 NbN - Paraconductivity

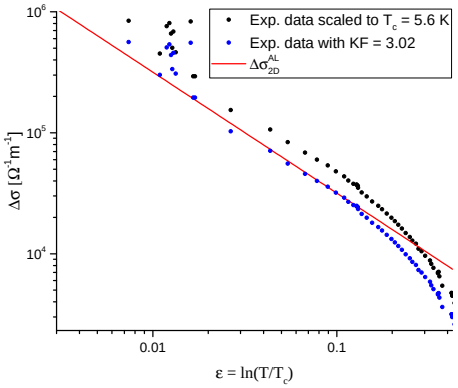

(a) Paraconductivity $\Delta\sigma(\epsilon)$ of the NbN stripe with nominal width $w_N = 0.6$ μm ($w_{\mathrm{SEM}} \approx 0.4$ μm).

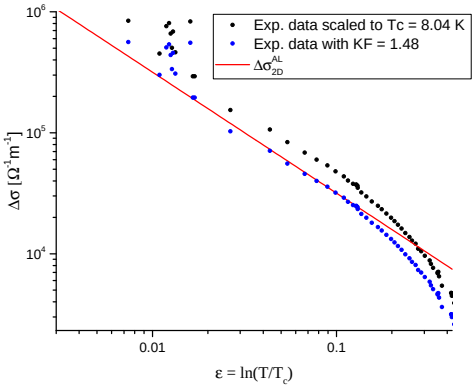

(b) Paraconductivity $\Delta\sigma(\epsilon)$ of the NbN stripe with nominal width $w_N = 0.8$ μm ($w_{\mathrm{SEM}} \approx 0.7$ μm).

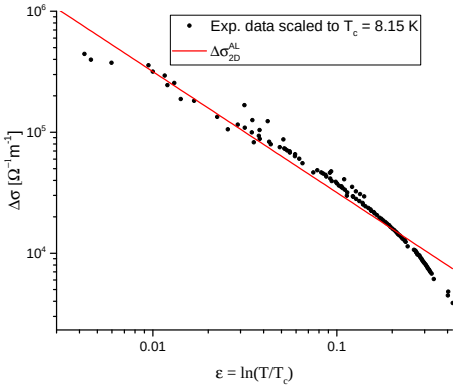

(c) Paraconductivity $\Delta\sigma(\epsilon)$ of the NbN stripe with nominal width $w_N = 1.2$ μm ($w_{\mathrm{SEM}} \approx 1.2$ μm).

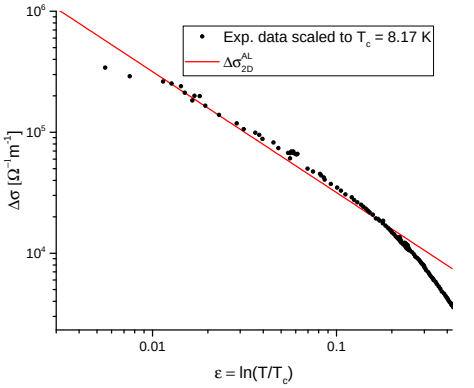

(d) Paraconductivity $\Delta\sigma(\epsilon)$ of the NbN stripe with nominal width $w_N = 1.6$ μm ($w_{\mathrm{SEM}} \approx 1.7$ μm).

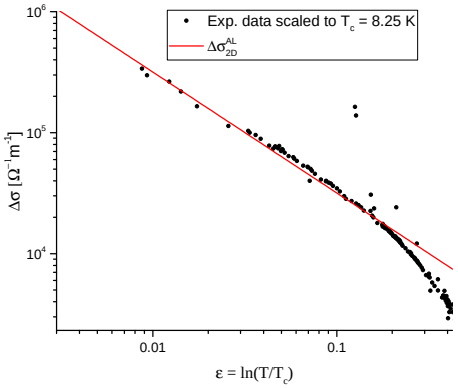

(e) Paraconductivity $\Delta\sigma(\epsilon)$ of the NbN stripe with nominal width $w_N = 2.4$ μm ($w_{\mathrm{SEM}} \approx 2.6$ μm).

Figure 33: Paraconductivity measurements of NbN. The experimental data was collected in the He-dewar.

7.2.4 NbN/NiCu - Paraconductivity and Magnetoconductivity

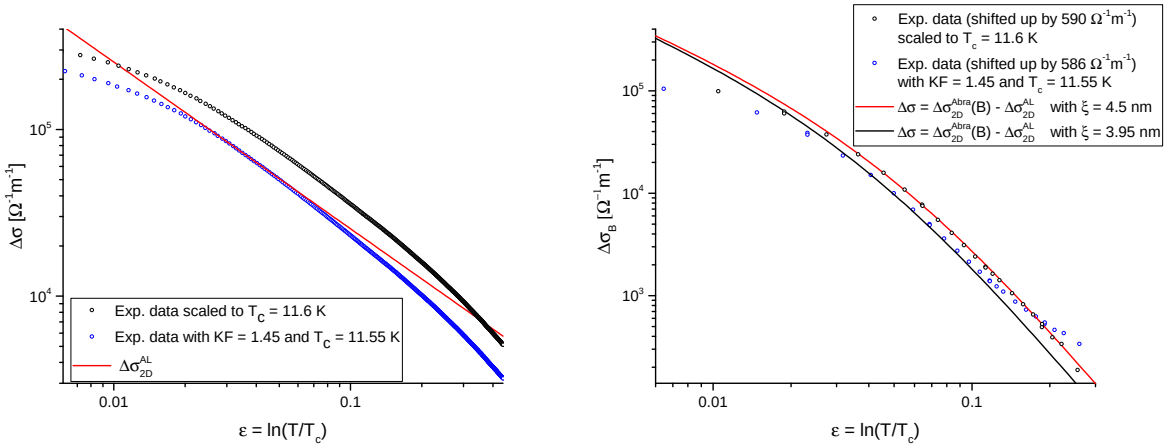

(a) Paraconductivity $\Delta\sigma(\epsilon)$ (b) Magnetoconductivity $\Delta\sigma_B(\epsilon)$

Figure 34: Paraconductivity and Magnetoconductivity of NbN/NiCu (nominal strip width: $w_N = 0.8$ μm, by SEM ≈ 0.2 μm). The magnetoconductivity results scaled by the SEM data were shifted up by 590 $(\Omega\text{m})^{-1}$ the corrected results by 586 $(\Omega\text{m})^{-1}$. The correction factor $KF = 1.45$ relative to the SEM data corresponds to a $KF_n = 0.29$ relative to the nominal data.

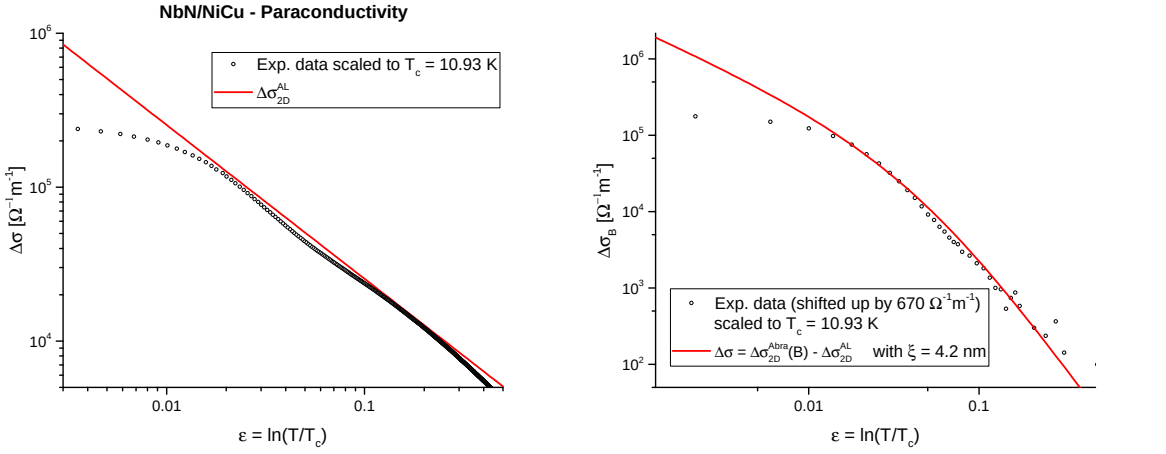

(a) Paraconductivity $\Delta\sigma(\epsilon)$ (b) Magnetoconductivity $\Delta\sigma_B(\epsilon)$

Figure 35: Paraconductivity and Magnetoconductivity of NbN/NiCu (nominal strip width: $w_N = 2.4$ μm, by SEM ≈ 1.8 μm) as a function of the reduced temperature ϵ. The magnetoconductivity data was shifted by 600 $(\Omega\text{m})^{-1}$.

7.3 Current-Voltage characteristics

Current-voltage characteristics were registered at liquid helium temperature by increasing the current through the sample and measuring the voltage. Starting at a current of 1 nA, the current was increased until the IV-characteristic showed a steep rise and then a linear behaviour.
A typical result is shown in figure 36a, which shows the IV-curve of the NbTiN sample (nominal strip width $w_N = 1.2\ \mu$m). The linear region at high currents was attributed to the normal-state resistance of this sample. A linear fit was performed in this region and extrapolated.
The transition to the normal state is very rapid at high currents. Figure 36b contains a detailed plot of the same curve. A linear rise of the voltage with the current can be observed, which is contrary to the behaviour one would expect from a superconductor. This voltage drop along the sample might be caused by the finite resistance of the samples in the "superconducting" state.
To determine the critical current, which marks the transition from the superconducting to the normal-conducting state, typically a voltage criterion of 30 V/m is used, which would correspond to 900 μV for our samples (which have a nominal length of 30 μm). In [55] an even stricter criterion of 1 V/m is used. Such a criterion is not applicable to our samples because the linear contribution leads to higher voltages long before superconductivity is destroyed. However the transition can be seen well in the graphs.

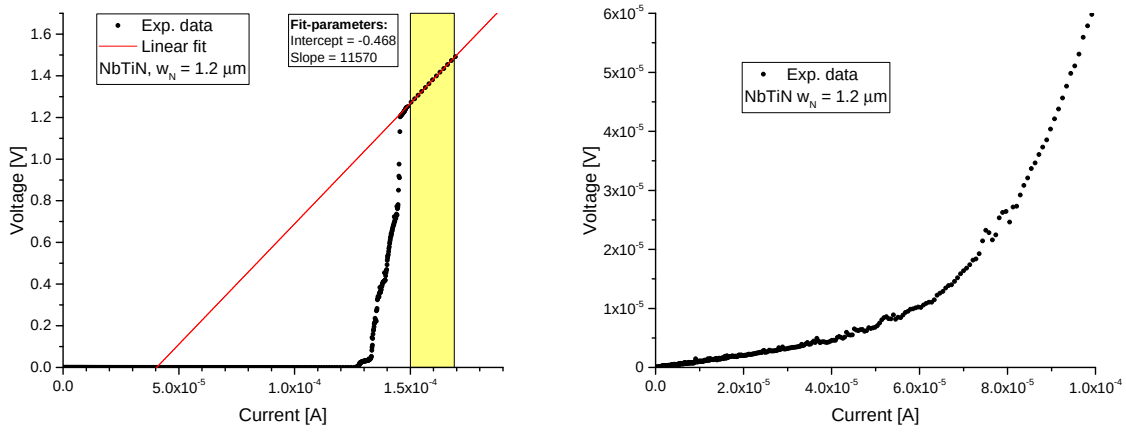

(a) (b)

Figure 36: Current-voltage characteristic of the NbTiN 1.2 μm stripe. The left image shows the entire curve with a linear fit to the normal-conducting region (slope = (11570 ± 38) V/A, intercept = (-0.468 ± 0.006) V). The right graph gives a detailed view of the same graph for low currents.

The following two graphs show the IV-characteristics of NbTiN and NbN as comparison of the single strip widths.
In contrast to the previous graphs, in the following ones the current density is used instead of the current. This gives the possibility to make a comparison between strips of different width. For the calculation of the current density the nominal thickness and the strip width determined from SEM images was used. For the bilayers only the thickness of the superconducting layer was taken into account. The results are given in the commonly used unit A/cm^2.
For NbN the S/F bilayers exhibit a higher critical current density than the superconducting

layers. For NbTiN it is the opposite case that all bilayers have a reduced critical current with respect to the single S layers.

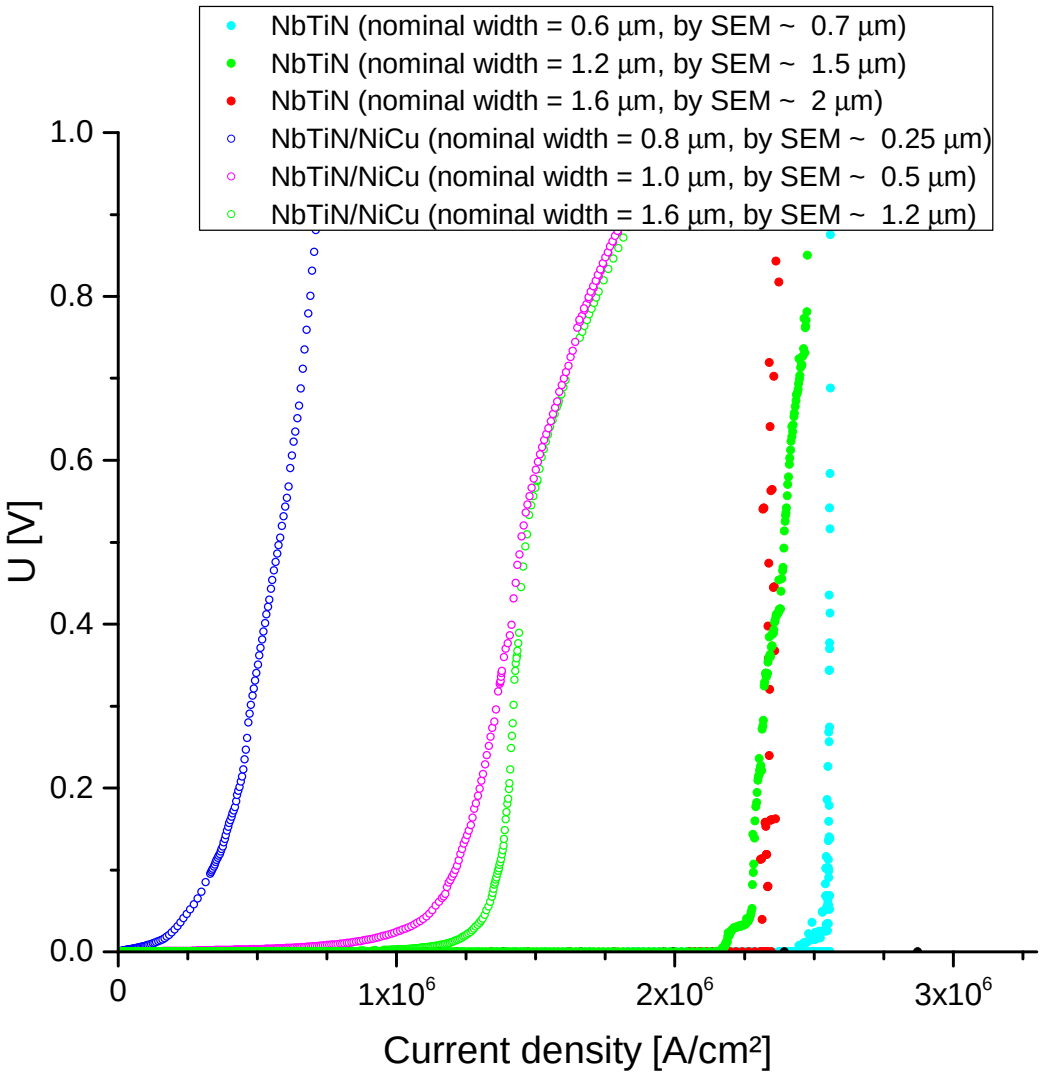

Figure 37: Current-voltage characteristics of NbTiN layers and NbTiN/NiCu bilayers at 4.2 K.

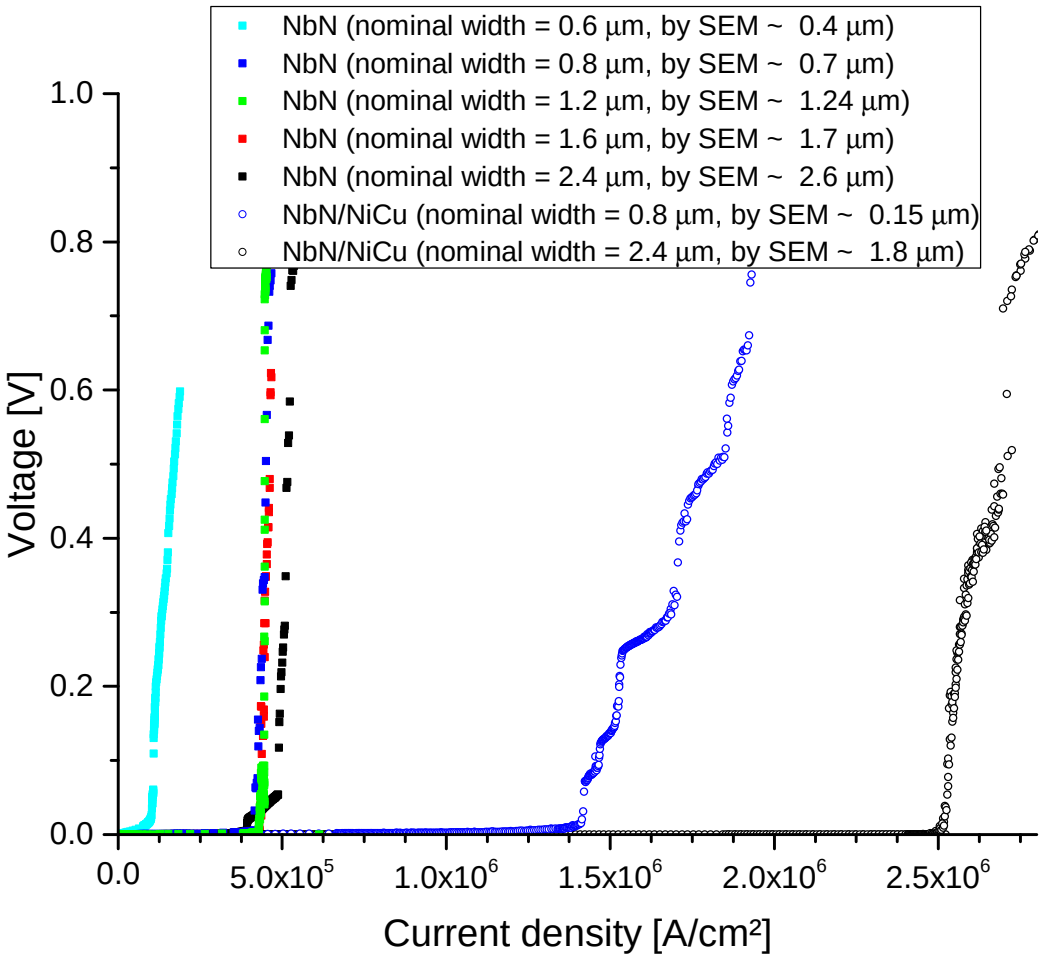

Figure 38: Current-voltage characteristics of NbN layers and NbN/NiCu bilayers at 4.2 K.

In these measurements the current was applied in both polarities to get rid of the thermoelectric voltage. Since in reference [55] it is shown that it makes a difference if the measurement is performed at an increasing or a decreasing current, an additional measurement was done to establish if this phenomenon can also be seen in the current samples. For that purpose the current was changed in a linear staircase sweep from -40 μA to 40 μA and back with voltage measurements in steps of 0.001 μA.
The result is shown in figure 39.

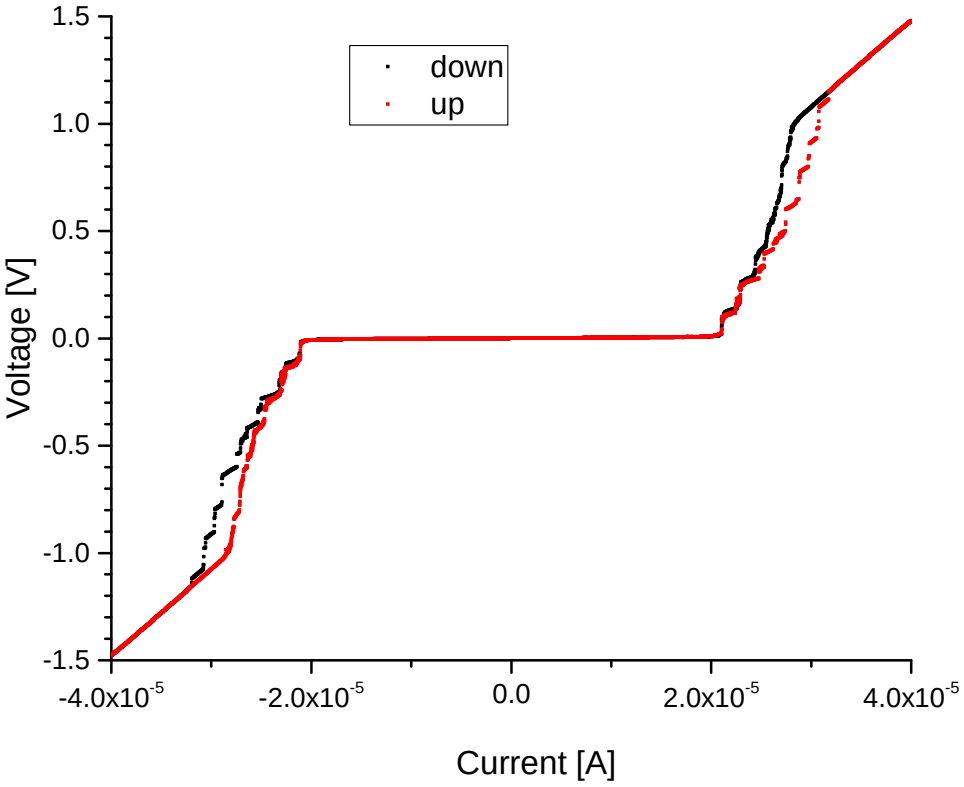

Figure 39: Current-voltage characteristic registered with a linear staircase sweep of the current. The strip with nominal width $w_N = 0.8$ μm of the NbN/NiCu sample was used.

It is interesting to see that there is a difference between the measurement with increasing and decreasing current, and that it does not matter in which direction the current flows through the sample. The deviation between the two curves can only be seen in the transition and is more distinct for higher currents. When the current is increased, higher values are possible with lower voltage drop than at descending current. When the current is decreased the sample rests for a longer time-span in the normal-conducting state (linear range in the graph). Moreover in the rising curve there are jumps in the IV-graph, which could be attributed to phase-slips.

7.4 Critical current

The critical current of the samples should be measured as a function of temperature. As discussed in section 5.4, the measurements were performed in the He-dewar and therefore it was not possible to do these measurements at a constant temperature. As a consequence it was the task to hold the measurement time as short as possible so that the temperature variation during one measurement is small.
The measurements started at the lowest reachable temperature of 4.2 K with the sample totally in the liquid helium and then the temperature was changed by slowly pulling the stick out of the dewar.
Some IV curves showed an ohmic contribution and, thus, significant voltages even at low currents, at which no transition into the normal conducting state could be observed. Hence a quite high voltage criterion of 25 mV had to be used to find the current at which the sample becomes normal conducting. This is an atypically big value and for some of the samples much smaller values would also give reasonable results.
A result of a measurement of the critical current density as a function of the temperature is shown in figure 40. This measurement was performed with the voltage-criterion of 25 mV. The most striking feature in this graph is that the critical current does not reach zero. This is because the voltage criterion is chosen so high that also when the superconductor is in the normal state, a significant current is needed to reach the criterion. Since this is not desirable, for all other measurements a resistance criterion was used. We defined the critical current as that current, at which the resistance reached 1% of the value at 20 K.

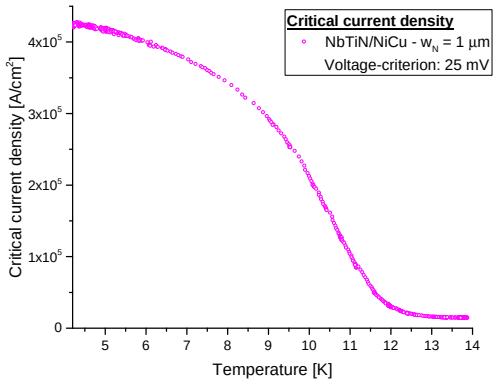

Figure 40: $I_c(T)$ curve for the 1.0 μm strip of the NbTiN/NiCu sample. For this measurement the voltage-criterion of 0.025 V was used. The graph shows the raw data.

Figure 41 shows normalized results for the different strip widths of the NbN sample and the 2.4 μm broad strip of the NbN/NiCu bilayer. The data is normalized to the critical current at 4.2 K, which was estimated from the measurement data. For a better comparison of the stripes the temperature was also normalized to T_c^*, which is the temperature, at which the sample resistance has fallen to 1 % of that at 20 K, analogously to the practise described in [40]. The value of T_c^* was calculated from the resistance versus temperature curves, measured with a current of 1 μA, by interpolation.
The same data is shown in figure 42, but there without normalization. One can see that the S/F bilayer exhibits a much higher j_c than the single NbN films, which was already clear from the IV-curves for 4.2 K and is now shown for the whole temperature range from 4.2 K to T_c^*.

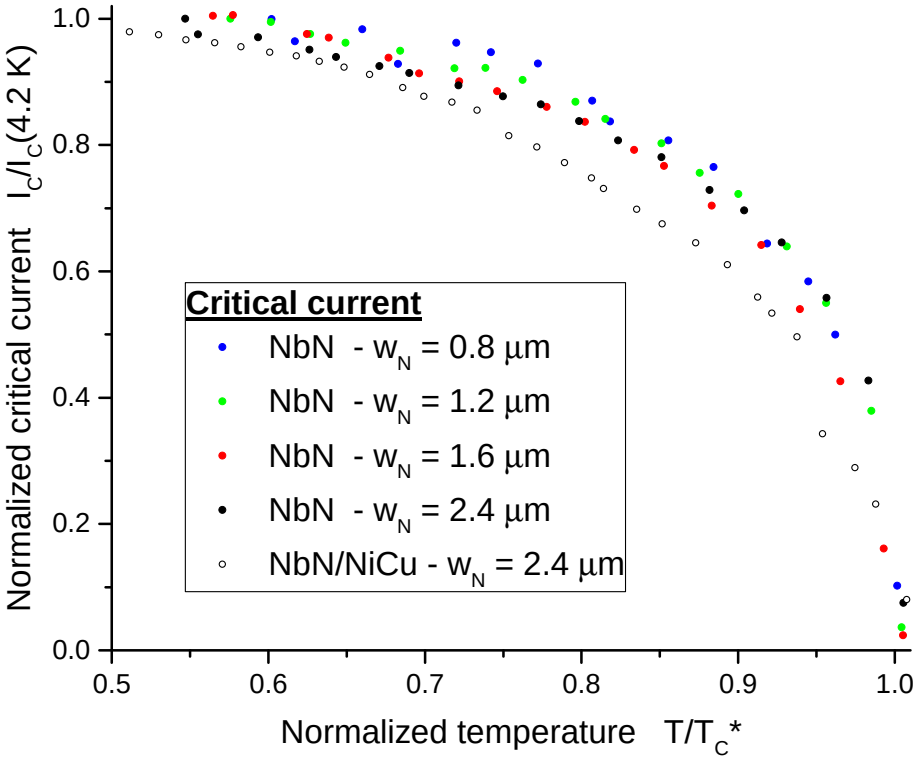

Figure 41: $I_c(T)$-characteristics of NbN films with different strip width w_N and a NbN/NiCu bilayer with $w_N = 2.4\ \mu$m. The data are normalized to the critical current at the boiling point of helium.

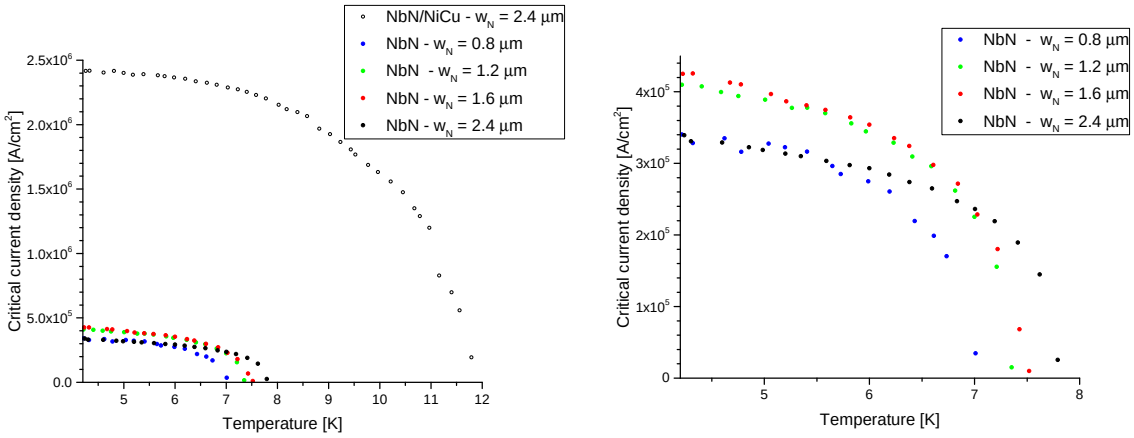

(a) NbN films and NbN/NiCu bilayers

(b) NbN films only

Figure 42: Comparison of the critical current density of NbN films and NbN/NiCu bilayers.

The $I_c(T)$ curves of the single NbN strips have a different shape because of variations in the resistance at the boiling point of helium and in the transition temperature. Therefore it is important for comparison to have the normalized data in figure 41. It points out that all stripes of the NbN sample show similar $I_c(T)$ characteristics, while that of the NbN/NiCu bilayer is somewhat different. The same effect can also be seen in the comparison of the three

analysed samples in figure 43b, where the two curves obtained from bilayers have almost the same shape, while that of the NbN film is different.
This comparison shows that the difference in shape should not be an effect of the low transition temperature of the NbN sample, because there is also a big difference in the transition temperatures of NbN/NiCu and NbTiN/NiCu and this does not result in a different shape of the $I_c(T)$-curves. However, for distinct results an $I_c(T)$ analysis of the NbTiN sample would be necessary.

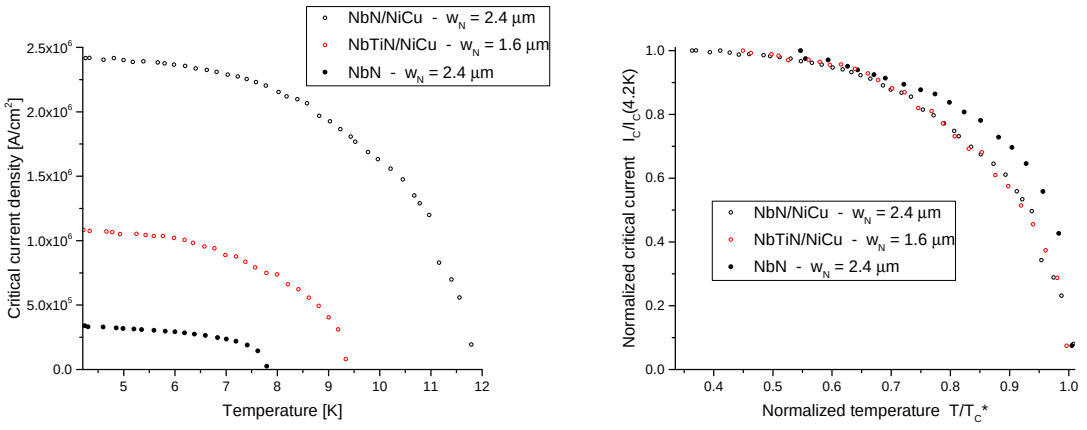

(a) Critical current density j_c

(b) Critical current I_c, normalized to $I_c(4.2\ \mathrm{K})$.

Figure 43: Comparison of critical current of the different samples: NbN, NbN/NiCu and NbTiN/NiCu.

8 Discussion

The investigation of superconducting thin films and superconductor/ferromagnet bilayers revealed quite big differences between the two systems.
A first distinction can be seen in the temperature-dependence of the resistance (see figure 24). Both for NbTiN and NbN (regarding the second set of samples) the S/F bilayers show a reduction of T_c relative to the pure S samples. This could be a signal for the appearance of the proximity effect, since it has been reported that this effect causes a variation of T_c in S/F bilayers [60]. However the effect is rather small and it could also be the case that the lower T_c is caused by impurities in the superconducting layer. Since there are differences in the transition temperature of the single strips of the same sample, it is probable that the superconducting material itself is not homogeneous. Additionally it is possible that atoms from the F layer diffuse into the S film as was previously reported for Nb/NiCu bilayers [61]. This would also explain the broadening of the transition, which can be seen for NbTiN/NiCu bilayers. Moreover the proximity effect could be reduced by the transition layer between the F and the S layer, which can be seen in transmission electron microscopy images of NbN/NiCu bilayers (see figure 44b, taken from reference [57]). The residual resistance in the "superconducting" region could be caused by the fact that in the used sample geometry the current first has to pass through the NiCu layer, before it reaches the superconductor. If the F layer is not fully proximitized, it might give a contribution to the measured resistance. However the contribution should be small, since the measurements have been performed in four-probe technique. Moreover this does not explain why the effect is more pronounced in narrow stripes.
The NbN sample of the first set was not taken in consideration for this discussion because it shows a very low T_c of about 8.5 K, which is much lower than the value for bulk NbN reported in reference [14]. Probably this can be attributed to a problem of the RTA (Rapid Thermal Annealing) process. W. Slysz et al., who prepared our samples, found that NbN samples on various substrates exhibited transition temperatures between 5.5 K and 9.5 K before annealing and T_c between 13 and 14 K after the RTA process [59]. This theory is reinforced by the measurements at the second set of NbN samples, which showed that both for NbN and NbN/NiCu, the samples, which had not been subjected to the RTA process, had a lower transition temperature (between 6 K and 9 K) than the annealed samples, which showed a T_c between 13 K and 14 K.
It was not possible to see a dependence of the transition temperature on the strip width. Probably the measured T_c depends more strongly on the imperfections in the superconducting material than on the width of the superconducting stripe. Furthermore a variation of the samples' T_c between the different measurements was noted, which was attributed to an ageing process of the superconducting material. Since from the aspect of the resistance curves it was not possible to determine, weather the influence of the F layer is only caused by the induction of inhomogeneities into the S material or by magnetic interference, the magnetoresistance of the various samples has been analysed.
NbTiN/NiCu and NbN/NiCu bilayers both show a negative magnetoresistance above T_c, while the single superconducting films do not exhibit this phenomenon. This is a strong signal for the influence of the ferromagnetic layer on the transport properties of the superconducting films.
For a further analysis, paraconductivity and magnetoconductivity of the S films and S/F bilayers were compared. It is noticeable that it is tendentially possible to obtain good fits with the theory for the broader stripes, while a correction factor KF is needed for the narrow ones. The first suggestion to explain this phenomenon would be that the effective width in narrow stripes is smaller because a possibly existing non-superconducting region at the margin of the stripes would have a bigger influence on narrow stripes. However, for most of the stripes the best fits were obtained with a $KF > 1$, which would point out that the

strip is broader, thicker or shorter than it was assumed. None of these explanations seems to be realistic. Since broad stripes lead to better consistency with theory, for the further discussion the measurement data obtained from the thickest stripe of each sample is used, which is that with $w_N = 1.6$ μm for NbTiN/NiCu and that with $w_N = 2.4$ μm for NbTiN, NbN and NbN/NiCu.
For NbTiN it was possible to get quite good fits of the measurement data with the theory of AL for paraconductivity and with the theory of Abrahams et al. for magnetoconductivity in the range of $\epsilon = 0.01$ to $\epsilon = 0.1$ with a value for the coherence length of $\xi = 4.9$ nm. The coherence length is in the same range as the sample thickness ($w_N = 3.9$ nm), which was expected from the fact that the fit with the two-dimensional theory is good.
In contrast to NbTiN, NbTiN/NiCu shows quite bad agreement with theory for both, paraconductivity and magnetoconductivity (see figure 32). For paraconductivity, there is only a small range, where the experimental data corresponds to the theory and for magnetoconductivity a smaller value for ξ has to be used to get an acceptable agreement with theory. In figure 32b both curves are plotted, the curve with $\xi = 3.75$ nm, which fits the data, and for comparison also the curve with $\xi = 4.9$ nm, which is the value for the coherence length obtained from the NbTiN sample. Although the values of ξ obtained for the different strips of NbTiN are wide-spread, the values, which are necessary to get reasonable fits for the NbTiN/NiCu samples are not in this range but considerably smaller (see table 7). A smaller value of the coherence length ξ for the S/F bilayers would imply that these materials have a higher critical field B_{c2}. However we would expect that the ferromagnetic layer on top of the superconducting film disturbs the superconducting properties and thus leads to a reduction of the critical field.
In the following paragraph possible sources of errors, which could lead to the bad coincidence of the measurement data with the theory, are discussed. Since the S/F bilayers exhibit a negative magnetoresistance, the $\Delta\sigma_B$ data was shifted up before the analysis in the way that the minimum of the curve is at zero. The ideal shift-parameter could not be determined because of the big noise of the measurement data in this region, but it seems not to be very crucial because there the curve is quite flat. The noise also prohibits to do fits at big values of the reduced temperature ϵ, but it does not disturb between $\epsilon \approx 0.001$ and $\epsilon \approx 0.1$, which is the most important region for fluctuation analysis. The exact value of ϵ or rather of T_c is not known because of difficulties in temperature measurements in the closed cycle cryostat. Therefore T_c was taken as fit-parameter for the fluctuation analysis. The assumption of a distribution of critical temperatures would make sense from a physical point of view because it is probable that the material contains inhomogeneities and thus regions with different critical temperatures. However this assumption would only influence the behaviour of the curve for small ϵ and can thus not explain the bad coincidence of the measured data with theory.
For the paraconductivity also the attempt to consider the Maki-Thompson contribution was tried, but the fits did not succeed. As expected this contribution can be neglected for the investigated samples, because it is only important for very clean materials. A further possible source of errors in the paraconductivity analysis could be the estimation of the normal resistance. For the NbTiN/NiCu 1.6 μm strip a linear fit in the range where the resistance begins to decrease was made to get such an estimation. For the paraconductivity analysis therefore a normal resistance of $R_N = 8764.65\ \Omega + 0.62\ \Omega/K \cdot T$ was used. In figure 44a the paraconductivity data calculated with two different values for R_N are shown and one can see that the value used for the normal resistance has only an influence on the data at $\epsilon > 0.3$, which is outside the typical interval for paraconductivity fits. All that points out that the bad coincidence of the experimental data with theory we got for the bilayers is not caused by errors, but by a different physical behaviour of these systems. In cooperation with A. Bouzdine and A. Varlamov two approaches to explain this behaviour were developed.

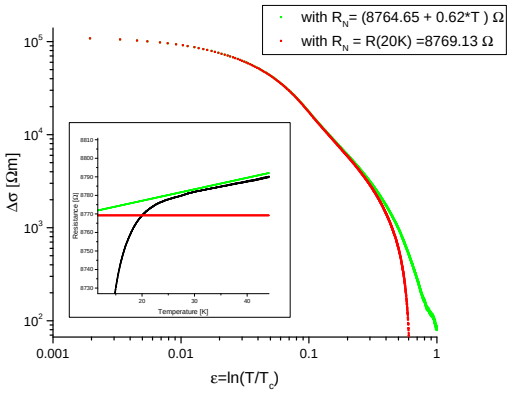

(a) Influence of R_N

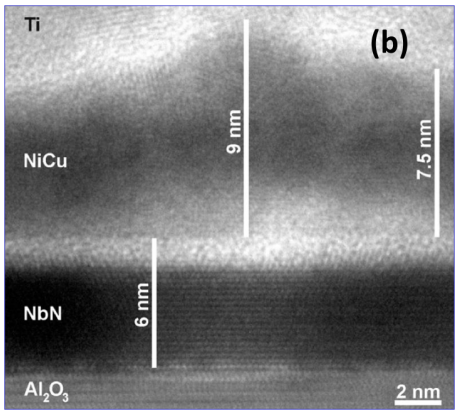

(b) TEM image of a NbN/NiCu bilayer.

Figure 44: Left image: Estimate of the influence of the normal resistance on the paraconductivity curve of NbTiN/NiCu.
Right image: Transmission electron microscopy image of a NbN/NiCu bilayer. Figure taken from [57]. Copyright 2015 Society of Photo Optical Instrumentation Engineers.

The first possibility is to consider the S and the F films as two independent neighbouring layers, which are isolated from each other. This theory is supported by the TEM image of a NbN/NiCu bilayer in figure 44b (taken from reference [57]), which shows that there exists a transition layer between superconductor and ferromagnet, where the material is disturbed. Under this assumption the F film can be treated as an independent system, which shows a magnetic hysteresis and thus creates an additional field B_{FM} (for FerroMagnetic), which is also existent when no external field is applied. To take this into consideration in the fitting process, it is necessary to replace the formula of Aslamazov and Larkin $\Delta\sigma_{2D}^{AL}$ by that of Abrahams et al. $\Delta\sigma_{2D}^{Abra}(B_{FM})$ both for paraconductivity and magnetoconductivity. This leads to the green curves shown in figure 45.
For NbTiN/NiCu this approach allows to create good fits with a value for ξ in the range of that found for single films and $B_{FM} = 0.6$ T. For NbN/NiCu the agreement between the experimental data and the theory is worse, the values used for the fit are $\xi = 4.2$ nm and $B_{FM} = 0.2$ T. The value of the coherence length is far away from the nominal value of $\xi_{NbN} = 7$ nm reported in reference [14] (But note that in [14] 120 nm thick NbN single crystals were investigated.) It was not possible to compare the value obtained for ξ with a value of the NbN film because no magnetoconductivity analysis could be done for the NbN films. Therefore the further discussion will concentrate on NbTiN. The value for B_{FM} seems too high. In reference [57] measurements of the magnetic moment of a 6 nm thick NiCu film and a NbTiN/NiCu bilayer (where both layers are 6 nm thick) are presented, whereby the magnetic field was oriented parallel to the film during the measurements. It is reported that the film showed a hysteresis loop with saturation between 5 and 10 kOe and a coercivity field of about 700 Oe for NiCu films and 400 Oe for NbTiN/NiCu bilayers. Even tough these measurements can not be compared directly to the fluctuation measurements presented in this thesis, because in the fluctuation measurements the field was applied perpendicular to the film, it can give an idea for the magnitude of the coercitivity field caused by the NiCu film. The value of B_{FM}, obtained from fluctuation analysis of the NbTiN/NiCu bilayer, is by a factor of ten bigger than the coercivity field reported in [57]. However, in the SQUID (Superconducting QUantum Interference Device) measurements presented in the mentioned article, a mean value for the coercivity field is determined, but maybe there exist magnetic domains in the material, which exhibit a much higher field.
I. Veshchunov et al. observed magnetic domains in NiCu thin films [62]. They investigated

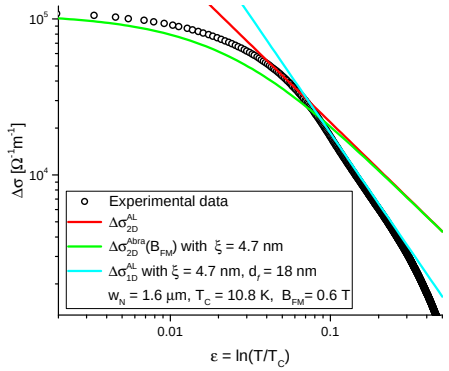

(a) Paraconductivity $\Delta\sigma$ of NbTiN/NiCu

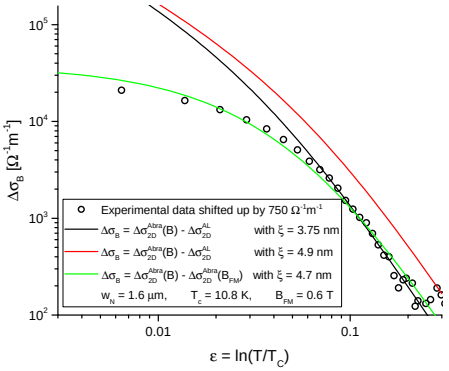

(b) Magnetoconductivity $\Delta\sigma_B$ of NbTiN/NiCu

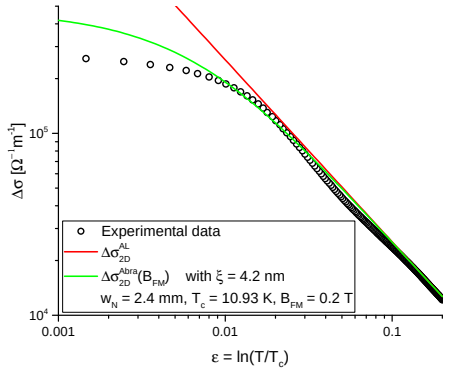

(c) Paraconductivity $\Delta\sigma$ of NbN/NiCu

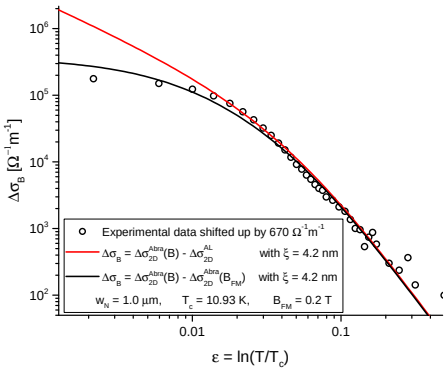

(d) Magnetoconductivity $\Delta\sigma_B$ of NbN/NiCu

Figure 45: Different approaches for paraconductivity and magnetoconductivity fits of S/F bilayers.

films with a thickness between 5 nm and 30 nm and found a coercive field in the range of 50 to 150 Oe at 4.2 K with the magnetic field perpendicular to the films. The domains were seen in decoration experiments, which revealed that they form maze-like structures with a domain width of about 100 nm.

The second approach to fit the fluctuation data is based on magnetic domains, too. It is based on the assumption that magnetic domain walls can locally modulate the critical temperature of the superconducting material and create thus one-dimensional structures along the domain walls, which contribute to the conductivity. This gave the impulse to fit the paraconductivity data with the formula found by Aslamazov and Larkin for 1D structures $\Delta\sigma_{1D}^{AL}$ (see equation 12). This theory considers all fluctuation components, independently of their direction whereas the measurement only reveals those which are parallel to the strip axis. Therefore the theoretical curve has to be multiplied with a pre-factor of $2/\pi$ to compensate this issue[6]. The measurement data of the NbTiN/NiCu sample exhibits a 1D critical

[6] When the filament does not go straight along the strip's axis, but with an angle φ relative to it, only the portion along the axis contributes to the measured conductivity $\Delta\sigma^{meas}$. Using trigonometric functions this can be described by $\Delta\sigma^{meas} = \Delta\sigma \cdot \cos\varphi$. Since we assume that all values for φ from $-\pi/2$ to $\pi/2$ have the same probability, we can calculate a medium value for $\Delta\sigma^{meas}/\Delta\sigma$ by integrating from $-\frac{\pi}{2}$ to $\frac{\pi}{2}$ and dividing the result by π:

$$\Delta\sigma^{meas}/\Delta\sigma = \frac{1}{\pi}\int_{-\frac{\pi}{2}}^{\frac{\pi}{2}} \cos(\varphi)d\varphi = \frac{1}{\pi}\Big[\sin\varphi\Big]_{-\frac{\pi}{2}}^{\frac{\pi}{2}} = \frac{2}{\pi} \tag{29}$$

exponent for $\epsilon > 0.1$ and allows a reasonable fit with $\Delta\sigma_{1D}^{AL}$. In a first step the diameter of these one-dimensional filaments d_f (with the cross-section area $A = (d_f/2)^2 \cdot \pi$) was taken as fitting parameter, since it is not known, how thick the superconducting filaments are. The adjustment of the curve thus led to a filament diameter $d_f = 18$ nm. A value of 18 nm for the diameter would be contradictory to the assumption that the filament is one-dimensional because it is much bigger than the superconducting coherence length. However this value can not be interpreted as real filament radius, because the theory assumes that only one filament with this radius contributes to the conductivity, while the measurement data are scaled as if the whole strip cross-section would contribute. In reality there is a number of small filaments with a diameter d_f. Since we assume that the filaments can be found between the magnetic domains, we estimate their number by the ratio between the strip width w and the diameter of one magnetic domain d_{dom}. This would lead to a re-scaling of the measurement data, which we avoid by scaling the theory [7]. Assuming a domain diameter of 100 nm (as found in [62]), this procedure gives a filament diameter of $d_f \approx 3.3$ nm.
The fact that the measurement data fits good to the 1D AL theory for $\epsilon > 0.1$ and to the 2D Abrahams theory for smaller values of ϵ, could be interpreted in the way that this system changes dimensionality with temperature.
In contrast to NbTiN/NiCu, for NbN/NiCu the paraconductivity data does not fit at all to the 1D AL theory. The effect of the ferromagnetic layer on the fluctuation behaviour of the NbN layers seems to be smaller than on that of NbTiN layers. Abrahams theory with a (relative to NbTiN) small backgroud field $B_{FM} = 0.2$ T describes the paraconductivity from $\epsilon \approx 0.001$ up to $\epsilon > 0.1$ and also AL theory, which does not take into account any magnetic field, fits the measurement data well over an order of magnitude. For the magnetoconductivity the impression is similar. It would be necessary to do further measurements of the paraconductivity and the magnetoconductivity of NbN films and NbN/NiCu bilayers to have the possibility to compare the data of S/F bilayers with that of single S films and with values from literature.

Apart from fluctuation analysis a further possibility to investigate the influence of the ferromagnetic layer on the superconducting properties is to determine the critical current of the different systems. The IV-curves in the figures 37 and 38 show that for NbN the bilayers show enhanced critical current densities relative to the pure S layers, whereas for NbTiN the critical current of the bilayers is lower than that of the single S layers. This effect can be seen for all examined strips.
All strips show remarkable critical current densities between 0.5 and 2.5 MA/cm^2, which is in the same range as the values reported in [57] for NbN and NbN/NiCu, but essentially higher for NbTiN and NbTiN/NiCu. This shows that the sample preparation process (the samples measured in the mentioned article were prepared by the same group) has been improved. However in [55] for both, NbN films and NbN/NiCu bilayers, values for the critical current are reported, which are by an order of magnitude higher than those measured by us.
In accordance to the mentioned article hysteretic behaviour of the current-voltage-characteristics was observed (see figure 39). Moreover especially in the rising branch of the current-voltage characteristics jumps can be noticed, a phenomenon, which can be seen for both, pure S films

[7] Since only a small fraction of the strip's cross-section contributes to the conductivity for calculating $\Delta\sigma$ the width w should be replaced by the factor $w/d_{dom} \cdot d_f$.

$$\Rightarrow \Delta\sigma = \frac{l}{\frac{w}{d_{dom}} d_f d}\left(\frac{1}{R} - \frac{1}{R_N}\right) = \frac{2}{\pi}\frac{\pi e^2 \xi}{16\hbar (d_f/2)^2 \pi \epsilon^{3/2}} \tag{30}$$

To avoid this, both sides of equation 30 are multiplied by d_f/d_{dom}, which leads to

$$\frac{l}{wd}\left(\frac{1}{R} - \frac{1}{R_N}\right) = \frac{e^2 \xi}{2\pi\hbar d_f d_{dom} \epsilon^{3/2}} \tag{31}$$

The right side of this equation was then used to fit the experimental data.

and S/F bilayers. These jumps may originate from phase-slips [8]. It is remarkable that for none of the samples a distinct point could be determined, at which superconductivity breaks down, but that the measured voltage rises in a number steps.
It should be taken in consideration that the measurement temperature of 4.2 K corresponds to $T_c/2$ for NbN (because of the low T_c of this sample), but only to about 1/3 of T_c for NbN/NiCu and the NbTiN or NbTiN/NiCu samples. One could argue that the higher values for I_c in NbTiN/NiCu bilayers are only caused by the bigger difference of the measurement temperature to the transition temperature for bilayers, but the $I_c(T)$ measurements (see figure 42a) show that the critical current only weakly depends on the temperature for $T \leq \frac{1}{2}T_c$ and that also at $T = \frac{1}{2}T_c$ the NbN/NiCu bilayer exhibits a much higher critical current density than the NbN film. The temperature dependence of the critical current shows a different behaviour of S films and S/F bilayers, too, which can be seen in figure 43b, where the critical current is normalized to the value at 4.2 K for all samples. Unfortunately the only measurements for single S films were made with the NbN sample with the reduced T_c, which makes it difficult to draw a definite conclusion from these results. Neither the measurement results for the bilayers nor those for the single NbN layer could be fitted with the $j_c(T)$ curves from GL theory or the approximations suggested by Bardeen (see equation 37). Since GL theory is only valid in the vicinity of the transition temperature, it is clear that it can not be used to fit the measurement data at low temperatures, but one would expect that it should lead to good fits near T_c. However, the accuracy of the measured values for j_c near T_c can be doubted since it was very difficult to get measurement points in this range because of small currents and the lack of temperature stability.
The fact that NbN/NiCu and NbTiN/NiCu bilayers show similar $I_c(T)$ characteristics, while that of NbN films is different, shows that the ferromagnetic layer has an influence on the critical current of the superconducting layers. The enhanced critical current densities in NbN/NiCu bilayers relative to NbN films could be explained by the diffusion of atoms from the F layer into the superconductor, which act as pinning centres. Another possible explanation is the existence of a magnetic domain structure in the NiCu layer, which could also lead to flux-pinning and thus to an enhancement of the critical current density. However it rests an open question why this effect could not be seen for NbTiN/NiCu bilayers, although this system seems to exhibit a stronger influence of the ferromagnetic layer in fluctuation analysis.
All in all the measurements performed in the framework of this thesis also showed that the quality of the superconducting samples and thus the sample preparation process plays a crucial role for the properties of S/F bilayers. The importance of the RTA process on the superconducting properties has been shown in the comparison of annealed and not annealed samples. Moreover in reference [62] it is reported that the Ni content in the ferromagnetic layer is an important parameter. For example in the mentioned article a Curie-temperature $T_{Curie} \approx 60$ K was measured for $Ni_{0.53}Cu_{0.47}$films, whereas in reference [55] a Curie-temperature of $T_{Curie} \approx 20$ K is reported for $Ni_{0.39}Cu_{0.61}$ films. For our samples with a nominal Ni content of about 54 % the Curie temperature is estimated to be above 30 K as claimed by Klimov et al. [57].
The fact that S/F bilayers showed reduced fluctuations near T_c and the enhancement of the critical current in bilayers are both important for a possible application of these materials in SSPDs. The strong dependence of the measurement results on the sample properties and the fact that the sample properties change with time makes it more difficult to interpret the measurement results.
In conclusion one can say that in the framework of this thesis a difference in the behaviour

[8] According to reference [46] in a superconducting nanowire the phase difference over the wire can be changed by 2π by a phase-slip. In this process the energy of $I\Phi_0$ (where I denotes the current and Φ_0 is the flux quantum) is dissipated.

of S films and S/F bilayers has been observed, which could be attributed to the influence of the ferromagnetic layer on the superconducting properties. For both superconducting alloys, namely NbN and NbTiN, this influence was seen, but the two materials behave in a different way. Since for both, fluctuation analysis and current-voltage-measurements, only one sample was used for each system and the sample properties are strongly dependent on the preparation process, further measurements with other samples and theoretical considerations are necessary to understand the dynamics in S/F systems.

Appendices

A The kinetic inductance

A short deduction of the formula for L_k can be made by simple algebraic calculations[9]. If we consider a wire with length l and cross-section-area $A = wd$ (with w and d the nanowire width and thickness), the current I through this wire is given by

$$I = Anv(2e) \tag{32}$$

with n the density of Cooper-pairs (the electron density thus would be $2n$), v the carrier velocity and $2e$ the charge of one Cooper-pair. By taking the carrier velocity from this formula and inserting it into the classical relation for kinetic energy, we get the kinetic energy of one Cooper pair $E_{kin}^{2e^-}$

$$E_{kin}^{2e^-} = \frac{1}{2}(2m)v^2 = \frac{1}{2}(2m)\left(\frac{I}{2eAn}\right)^2 \tag{33}$$

with $2m$ being the mass of a Cooper-pair. Thus the kinetic energy for the whole wire is given by

$$E_{kin} = Aln \cdot E_{kin}^{2e^-} = \frac{1}{2}\frac{l}{A}\frac{2m}{(2e)^2 n}I^2 \tag{34}$$

Since the relation between energy and inductance is given by $E = \frac{1}{2}LI^2$ we see by comparison with equation 34 that the kinetic inductance is given by

$$L_k = \frac{l}{A}\frac{2m}{(2e)^2 n} \tag{35}$$

In [64] the temperature dependence of is calculated using Ginzburg-Landau-theory:

$$L_k(T) = L_k(0)\left(\frac{1}{1-\frac{T}{T_c}}\right) \tag{36}$$

$L_k = L_k(0)$ is the kinetic inductance at zero temperature. Since equation 36 is deduced by using GL-theory, and by usage of approximations, it is only valid near T_c and for low currents, but in this range, A. Annunziata et al. found a very good agreement of their experimental data with the one calculated by equation 36 and a relative strong dependence of the kinetic inductance on the temperature[64].
From equation 36, one can see that the kinetic inductance is most pronounced in the vicinity of the transition temperature.

[9]The deduction of the formula for the kinetic inductance has been showed in the Youtube-video [63]. Here it has been modified to be applied to Cooper pairs ($2e$ and $2m$). The result is identical to the formula given in [42]. Note that the notation in the above-mentioned article is different!

B The minimal hotspot radius

Let us consider a cylindrical hotspot with radius r in a superconducting stripe with a width w and a thickness d. The requirement for a transition to the normal state is, that the current density j in the sidewalks around the hotspot exceeds the critical current density j_c.
The critical current density is given by 37, the current density in the sidewalks by 38.

$$j_c = \frac{I_c}{dw} \tag{37}$$

$$j = \frac{I_B}{d(w-2r)} \tag{38}$$

The condition $j > j_c$ gives now

$$\frac{I_B}{d(w-2r)} > \frac{I_c}{dw} \tag{39}$$

Simple algebraic calculations now lead to the result as shown in equation 20 and in Ref. [65].

$$r \geq \frac{w}{2}\left(1 - \frac{I_B}{I_c}\right) \tag{40}$$

C The samples - photographs and schematic pictures

C.1 1^{st} set of samples: NbTiN and NbTiN/NiCu

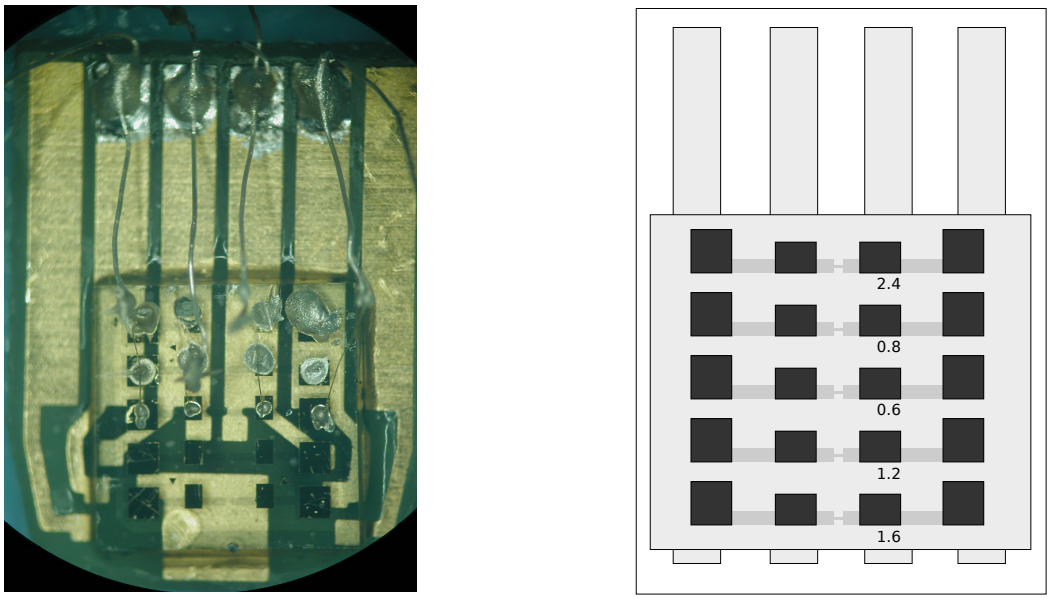

Figure 46: Photograph and schematic picture of the NbTiN sample. The stripes with nominal width $w = 0.6$ μm, $w = 1.2$ μm, $w = 1.6$ μm, and $w = 2.4$ μm are functional.

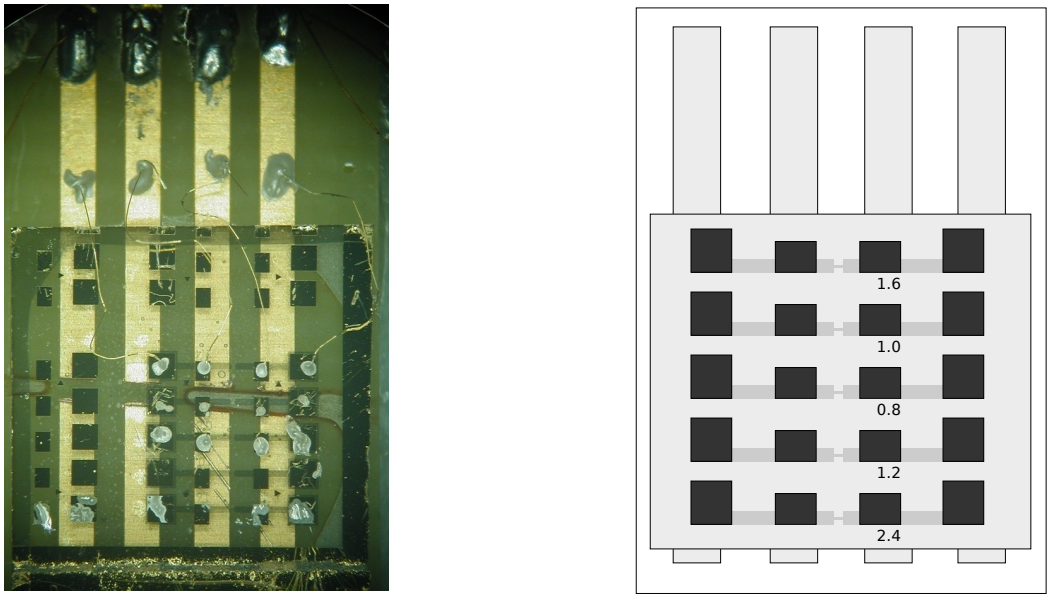

Figure 47: Photograph and schematic picture of the NbTiN/NiCu sample. The stripes with nominal width $w = 0.8$ μm, $w = 1$ μm and $w = 1.6$ μm are functional.

C.2 1^{st} set of samples: NbN and NbN/NiCu

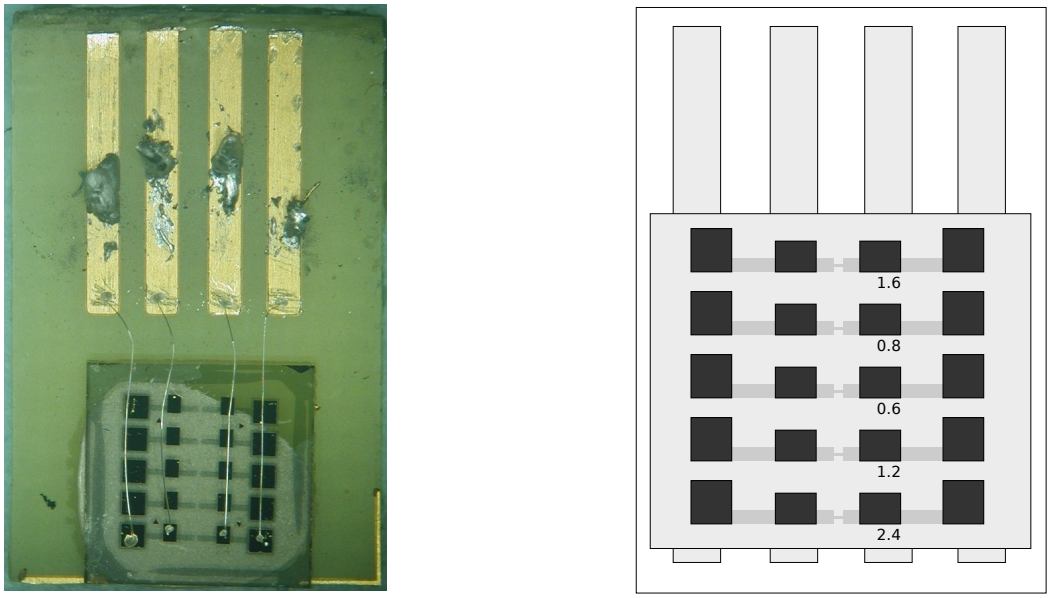

Figure 48: Photograph and schematic picture of the NbN sample. All stripes are functional.

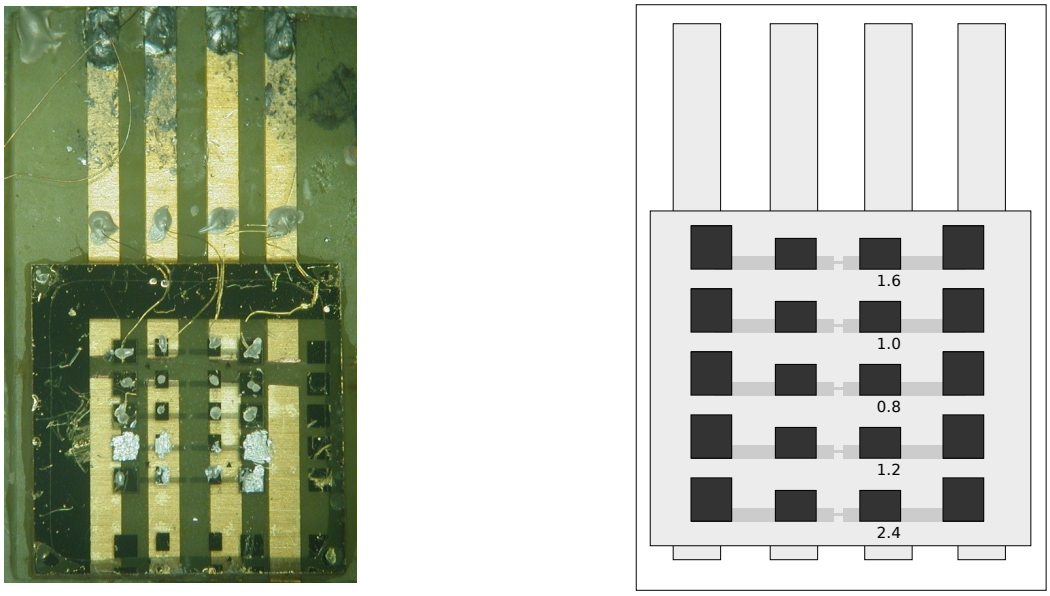

Figure 49: Photograph and schematic picture of the NbN/NiCu sample. The stripes with nominal width $w = 0.8$ μm and $w = 2.4$ μm are functional.

C.3 2^{nd} set of samples: NbN and NbN/NiCu - without RTA

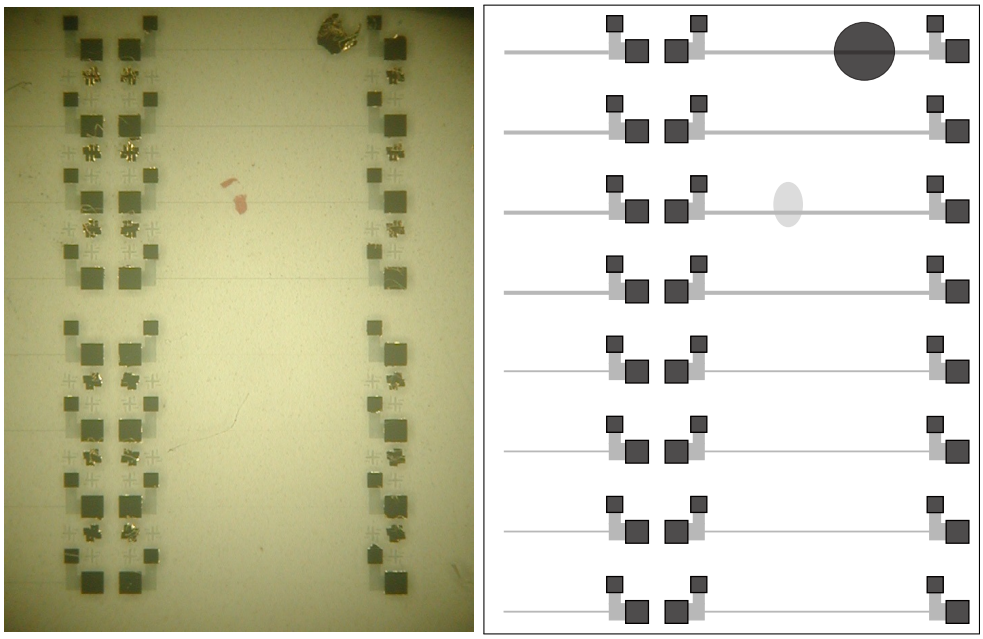

Figure 50: Photograph and schematic picture of the NbN sample without RTA. There are four stripes with a nominal width of 4 μm and four with a nominal width of 12 μm. The stripes 1 and 7 (counted bottom-up) were used for measurements.

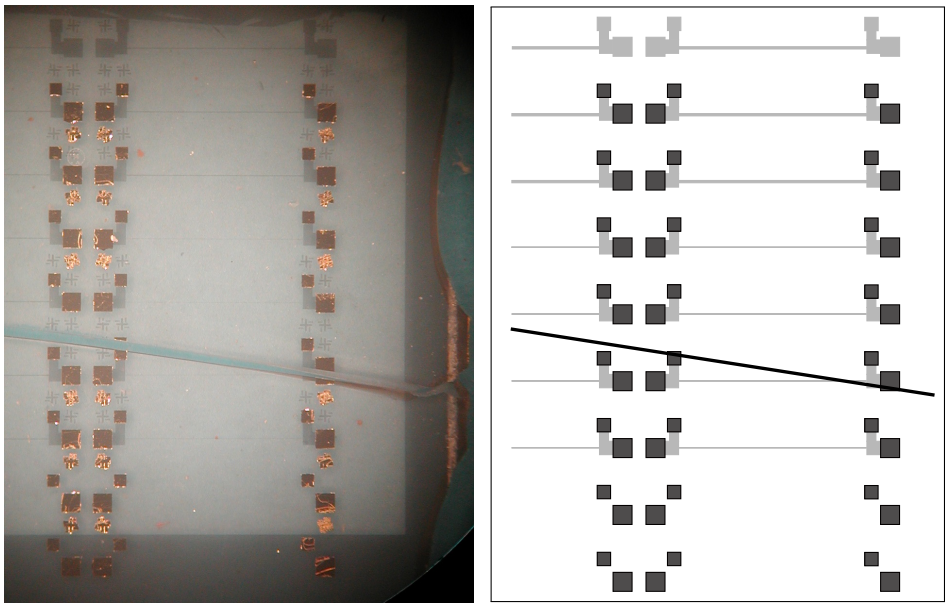

Figure 51: Photograph and schematic picture of the NbN/NiCu sample without RTA. There are four stripes with a nominal width of 4 μm (one of them is destroyed by the crack in the substrate) and two with a nominal width of 12 μm. The sixth stripe (counted bottom-up) was used for measurements. The substrate is broken at the position of stripe number two, but this does not influence the functions of the other stripes.

C.4 2^{nd} set of samples: NbN and NbN/NiCu - with RTA

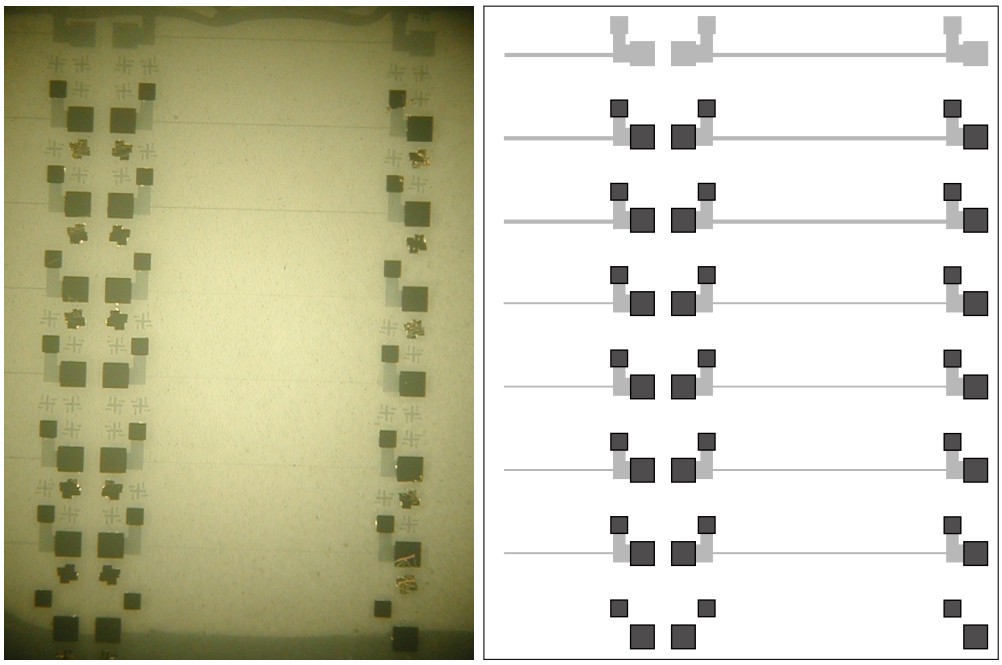

Figure 52: Photograph and schematic picture of the NbN sample produced with RTA. There are four stripes with a nominal width of 4 μm and two with a nominal width of 12 μm. The sixth stripe (counted bottom-up) was used for measurements.

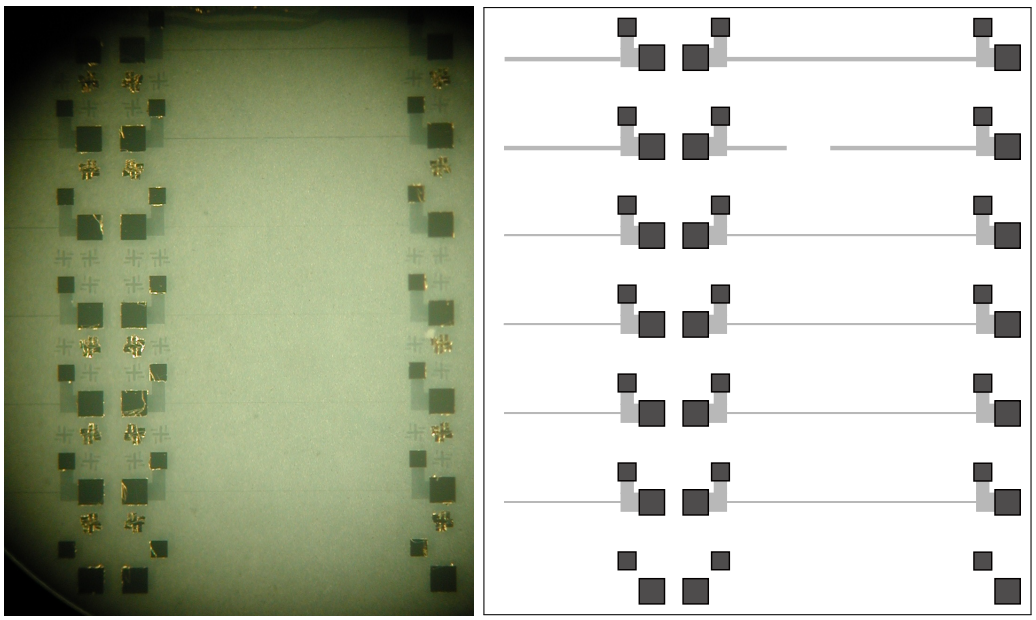

Figure 53: Photograph and schematic picture of the NbN/NiCu sample produced with RTA. There are four stripes with a nominal width of 4 μm and two with a nominal width of 12 μm. The fifth stripe (counted bottom-up) is interrupted and can not be used. The sixth stripe was used for measurements.

D Test of the RhFe-sensor in the closed-cycle cryostat

The rhodium iron temperature sensor of the closed-cycle cryostat was tested with a RhFe calibration sensor (R10627 of LakeShore). The calibration sensor was mounted on a sample-holder like a sample and fixated with aluminum foil and Teflon tape (see figure 54). Cryogenic high vacuum grease Apiezon was used to provide better thermal contact. The sensor has four wires, which were connected the same way as the wires of a sample.
A measurement was performed with a measurement current of $I = 0.1$ mA, a settle time (time between switching on the current and measuring the voltage) of 0.3 s and 1 s time delay between the measurements. Such the resistance of the calibration sensor was measured. During the measurement the temperature was swept from 300 K to 10 K at a rate of 0.3 K/min. The calibration file of the calibration sensor gave us the possibility to calculate the temperature from the resistance data by interpolation.
We see that the difference of the two sensors is about 0.05 K at high temperatures, but it rises to about 0.25 K in the region of temperatures lower than 25 K. This could be due to problems in heat conduction through the sample holder.

Figure 54: The calibration sensor mounted on the sample-holder (left) and in the cryostat (right).

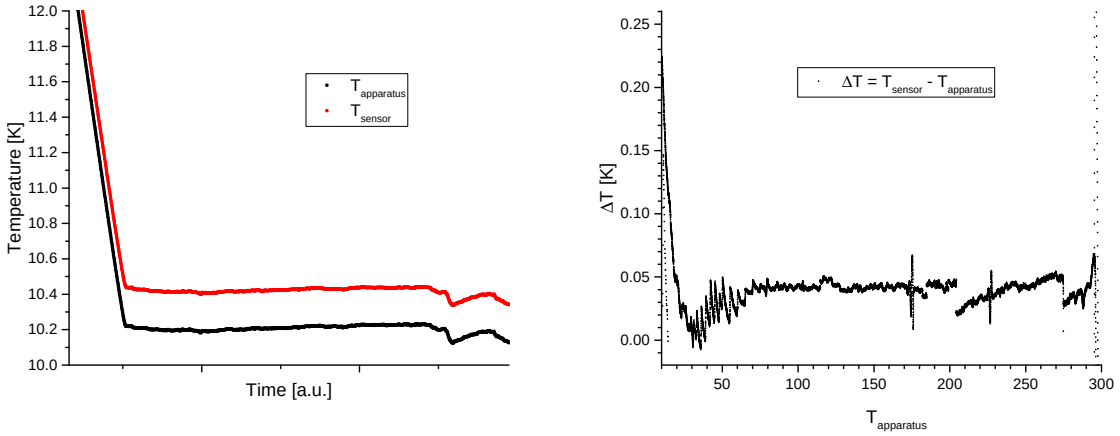

Figure 55: Test of the rhodium-iron sensor (A) of the closed-cycle cryostat. $T_{apparatus}$ denotes the temperature measured by the internal temperature sensor (sensor A), T_{sensor} the tenperature measured by the calibration sensor. In the left image the temperature is plotted versus time, the right plot shows the difference of the two sensors at various temperatures.

E Electrical connections in the closed-cycle cryostat

The connections inside the cryostat are shown in figure 56. Additionally there are cables for the temperature sensors (four wires for each sensor) and for the heating elements (two wires per heating element).
The electrical connections are realized via thin coaxial cables. Additionally there is a wire for grounding the copper stick, on which the sample is mounted and a cable, which can be used to supply an optional pre-amplifier-chip with electrical power. This pre-amplifier-chip can be inserted at the plug connection (big dashed rectangle in the circuit). The sample-holder is connected to the pin-socket (small dashed rectangle).
Figure 56 shows the standard constellation. However, because of problems with the inner wires of the coaxial cables, the connections were changed during the measurements for this thesis and actually the outer wires of the coaxial cables are used for voltage and Hall-voltage connections.

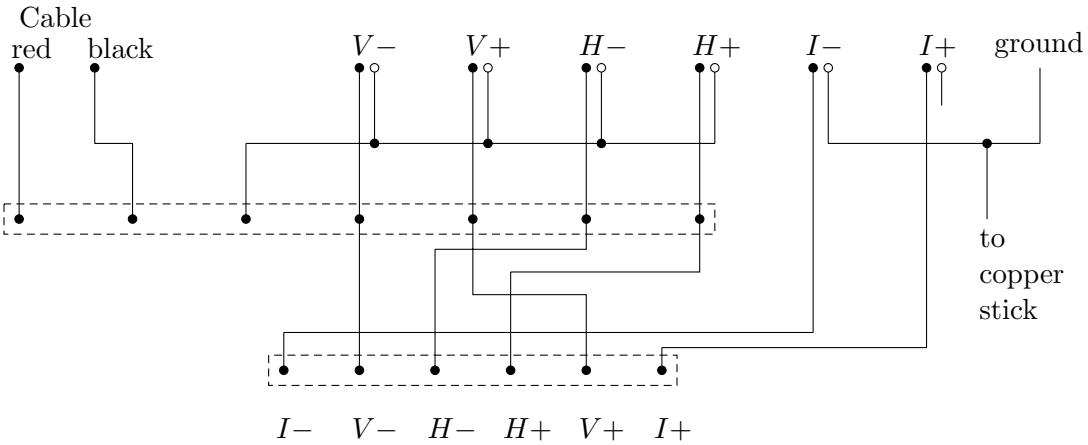

Figure 56: Scheme of the connections inside the cryostat. The bigger dashed rectangle stands for the plug connection, the smaller one for the pin socket. For the coaxial cable the inner wire is represented by a dot, the outer wire by an open circle at the beginning. I+/I- are the current-contacts, V+ and V- are used for the voltage and H+/H- for Hall voltage.

F Controlling the magnet

The magnet controlling unit has a socket with seven pins, which are labelled with letters from A to G. Since the user manual of the magnet controlling unit was not available the function of the single pins had to be understood from the fact to which inputs of the old DAC/ADC card they were connected.

A gives a voltage, which is proportional to the current through the magnet's coils
B digital switch for the magnet's polarity B=1, C=0 → positive polarity
C digital switch for the magnet's polarity B=0, C=1 → negative polarity
D digital mass
E controls the current through the magnet (needs a voltage between 0 V and 7.5 V).
F analogue mass
G (function not known)

The magnet controlling unit has two digital inputs (B and C). They are used to switch the polarity of the current through the coils. The amplitude of the current is controlled by a DC voltage between the pins E and F. The current through the magnet is proportional to this voltage, the absence of a voltage results in no current passing through the magnet and at the maximal voltage of 7.5 V a current of 30 A is set. Moreover the magnet controlling unit returns a voltage signal at pin A, which is proportional to the current through the coils. It is useful to register this signal during the measurements to see if the current through the magnet is the desired one. If, for example, the magnet becomes hot, the current through it is interrupted and no magnetic field is produced although the computer sends a voltage signal to the magnet controlling unit. The response signal provided at pin A is useful to detect such errors.

The *4861B - GPIB ↔ analog interface* of ICS electronics was used to connect the magnet controlling unit to the computer. For the magnet's current control the Analog Out 1 (Pin 42) of the DAC was used, for the return signal the Analog input 1 (Pin 11). For the control of the polarity the digital outputs 1 (pin 6) and 2 (pin 5) were used. The digital mass pin of the magnet controlling unit was connected to the digital out return pin (pin 7) of the DAC. The "digital out V Com" pin (pin 2) was connected to the +5V power (pin 1) and pull-up resistors of 10 kΩ were set between the digital outputs and the "digital out V Com" pin. A scheme of these connections is given in figure 57.

In the following the most important commands for controlling the magnet from the computer via the *4861B - GPIB ↔ analog interface* are listed.

- **MEAS:VOLT? 1** → Measures the voltage at the analog input 1. This command is used to acquire the response signal of the magnet controlling unit.
- **C 1** → Selects the analog output 1.
- **D 4.2** → Sets the voltage of the selected analog output to 4.2 V.
- **L 7.5** → Sets the voltage limit for the selected analog output to 7.5 V.
- **Inst 1** → Selects the digital output 1.
- **OUTput ON** → Switches the selected digital output on (sets it to ≈0.6 V).
- **OUTput OFF** → Switches the selected digital output off (sets it to ≈5 V).

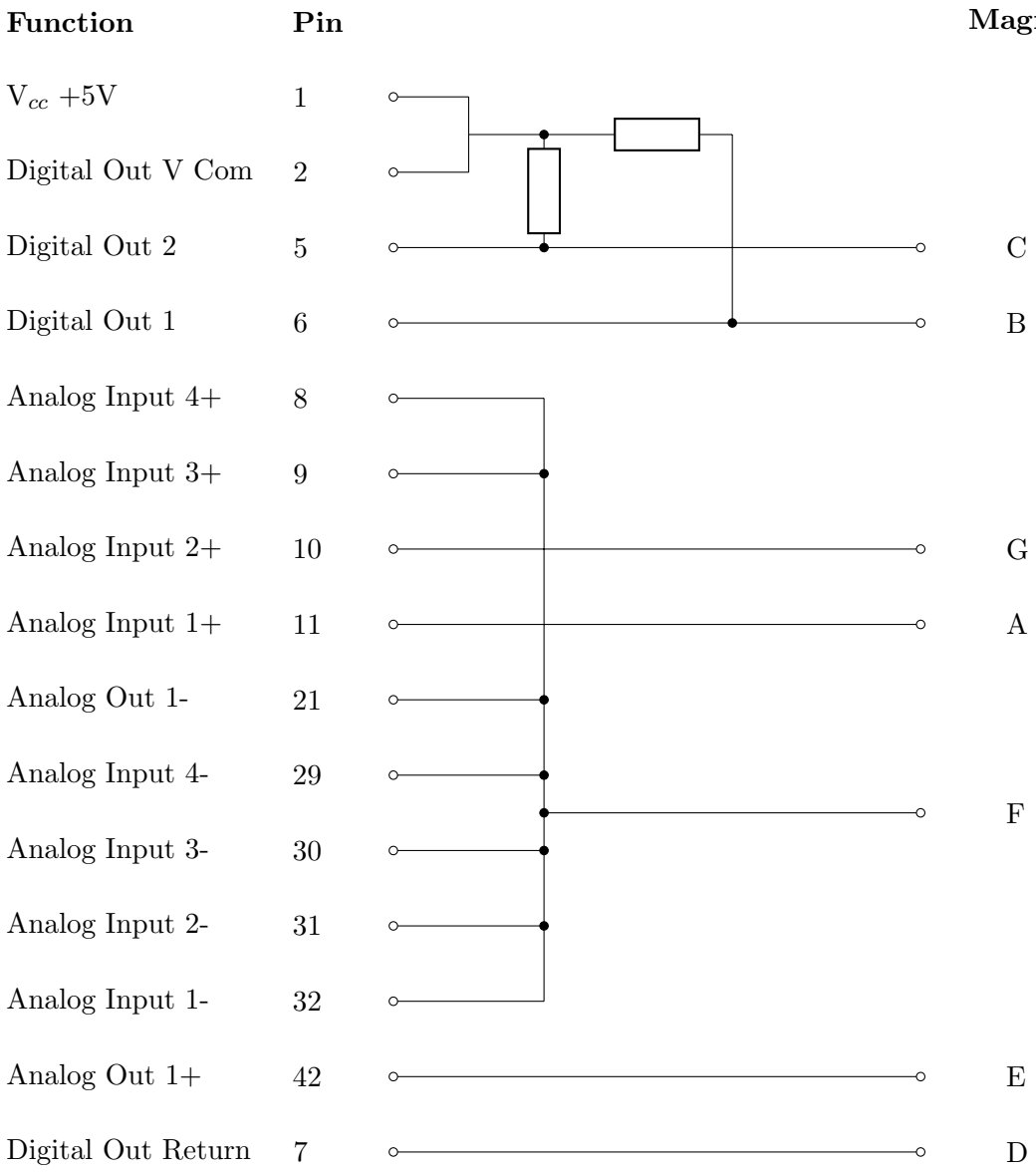

Figure 57: Connection of the magnet controlling unit to the *4861B - GPIB ↔ analog interface*. The numbers at the left side refer to the pins at the DAC, the letters at the right side to the socket of the magnet controlling unit. Both resistors have a resistance of 10 kΩ.

G Characteristics of the magnet

The field produced by the magnet at various currents was measured using a *Bell 620* gaussmeter. The gap was kept at the constant level of 50 mm during the measurement. Between every single measurement the current was first increased to 30 A and then set to the desired value.
The magnet was controlled via the *4861B - GPIB ↔ analog interface*.

Current [A]	**Magnetic field [mT]**
30	920
29.5	910
25	825
20	700
15	530
10	350
5	180
4	145
3	108
2	73
1	38

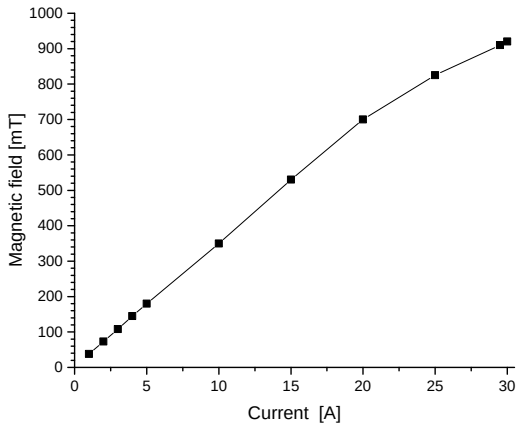

Figure 58: Magnetic field in dependence on the current through the magnet coils. The gap between the coils was kept at 50 mm during the measurement. List and plot of the measured values for the magnetic field. The solid line in the graph should serve as guide for the eye.

H Details of the (new) distribution box (for measurements in the He dewar)

The distribution box has the task to connect the measurement devices with the 10-pin connector on the dip-stick. The pins on the 10-pin connector are signed with letters from A to L. A plug, which matches to the 10-pin connector on the dipstick was soldered to a custom LAN cable with eight wires, which are twisted in pairs. In the box the wires are connected to the sockets by screws. Photographs of the new box can be seen in figure 59. The function of the single connections in the box or given in table 8.

Function	Pin of the 10-pin connector on the dipstick	Wire color
$I+$	C	brown
$I-$	J	brown/white
$V+$	L	orange/white
$V-$	K	orange
$T+$	D	blue
$T-$	E	blue/white
$T+$	H	green/white
$T-$	F	green

Table 8: Function of the single pins in the socket on the dip-stick. Additionally the color of the wires, which are connected, is listed. The contacts for the sample in the copper-cylinder at the end of the stick are (from left to right): $I-$, $V-$, $V+$, $I+$.
$I+$ and $I-$ are used as current contacts, $V+$ and $V-$ as voltage contacts. $T+$ and $T-$ are connected to the RhFe temperature sensor in the stick.

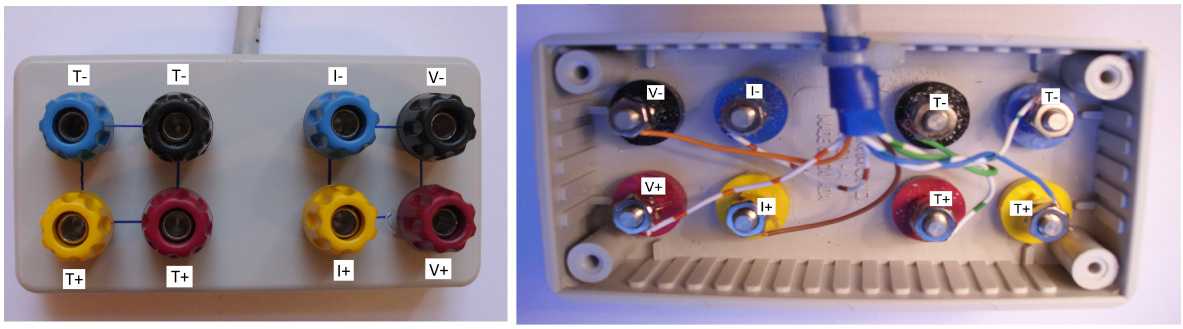

Figure 59: Pictures of the distribution box. On the right picture, one can see, which wire is connected to which pin. The letters explain the connections: $I+$ and $I-$ are the current contacts, $V+$ and $V-$ the voltage contacts. The temperature sensor has two positive ($T+$) and two negative contacts $T-$. It does not matter, which of them is used as current and which as voltage contact.

List of Figures

List of Tables

References

[1] H. K. Onnes *Commmun. Phys. Lab. Univ. Leiden*, no. 120b, 1911.

[2] W. Meissner and R. Ochsenfeld, "Ein neuer Effekt bei Eintritt der Supraleitfähigkeit," *Naturwissenschaften*, vol. 21, pp. 787–788, Nov 1933.

[3] J. R. Waldram, *Superconductivity of metals and cuprates*. Bristol [u.a.]: Inst. of Physics Publ., 1996.

[4] F. London and H. London, "The Electromagnetic Equations of the Supraconductor," *Proceedings of the Royal Society A: Mathematical, Physical and Engineering Sciences*, vol. 149, pp. 71–88, Mar 1935.

[5] V. L. Ginzburg and L. D. Landau *Zh. Eksperim. Theor. Fiz.*, vol. 20, p. 1064, 1950.

[6] L. P. Gor'kov, "Microscopic derivation of the Ginzburg-Landau equations in the theory of superconductivity," *Soviet Physics JETP*, vol. 36(9), p. 1364, December 1959.

[7] J. Bardeen, L. N. Cooper, and J. R. Schrieffer, "Microscopic theory of superconductivity," *Physical Review*, vol. 106, pp. 162–164, Apr 1957.

[8] J. Bardeen, L. N. Cooper, and J. R. Schrieffer, "Theory of superconductivity," *Physical Review*, vol. 108, pp. 1175–1204, Dec 1957.

[9] J. G. Bednorz and K. A. Müller, "Possible high T_c superconductivity in the Ba-La-Cu-O system," *Z. Physik B - Condensed Matter*, vol. 64, pp. 189–193, Jun 1986.

[10] R. Gross and A. Marx, *Festkörperphysik*. München: Oldenbourg, 2012.

[11] J. Bardeen, "Critical fields and currents in superconductors," *Rev. Mod. Phys.*, vol. 34, pp. 667–681, Oct 1962.

[12] M. Y. Kupriyanov and V. F. Lukichev, "Temperature dependence of pair-breaking current in superconductors," *Fizika Nizkikh Temperatur*, vol. 6, no. 4, pp. 445–453, 1980.

[13] P. Hilsch, "Zum Verhalten von Supraleitern im Kontakt mit Normalleitern," *Zeitschrift für Physik*, vol. 167, no. 5, pp. 511–524, 1962.

[14] A. Shoji, S. Kiryu, and S. Kohjiro, "Superconducting properties and normal-state resistivity of single-crystal NbN films prepared by a reactive rf-magnetron sputtering method," *Applied Physics Letters*, vol. 60, no. 13, p. 1624, 1992.

[15] T. Matsunaga, H. Maezawa, and T. Noguchi, "Characterization of NbTiN thin films prepared by reactive DC-magnetron sputtering," *IEEE Transactions on Applied Superconductivity*, vol. 13, pp. 3284–3287, Jun 2003.

[16] Pierre Villars, Material Phases Data System (MPDS), CH-6354 Vitznau, Switzerland (ed.) SpringerMaterials, "δ-NbN (NbN ht2) Crystal Structure." (Springer-Verlag GmbH, Heidelberg, © 2014) Accessed: 26-01-2016.

[17] Pierre Villars, Material Phases Data System (MPDS), CH-6354 Vitznau, Switzerland (ed.) SpringerMaterials, "NbTiN (Ti0.5Nb0.5N) Crystal Structure." (Springer-Verlag GmbH, Heidelberg, © 2014) Accessed: 26-01-2016.

[18] T. C. Ozawa and S. J. Kang, "Balls & Sticks: easy-to-use structure visualization and animation program," *J Appl Crystallogr*, vol. 37, pp. 679–679, Jul 2004.

[19] W. Skocpol and M. Tinkham, "Fluctuations near superconducting phase transitions," *Reports on Progress in Physics*, vol. 38, no. 9, pp. 1049–1097, 1975.

[20] A. Larkin and A. Varlamov, *Theory of Fluctuations in Superconductors*. Clarendon Press, Oxford, 2005.

[21] R. E. Glover, "Ideal resistive transition of a superconductor," *Physics letters*, vol. 25A, pp. 542–543, October 1967.

[22] L. Aslamazov and A. Larkin, "The influence of fluctuation pairing of electrons on the conductivity of normal metal," *Physics letters A*, vol. 26A, pp. 238–239, 1968.

[23] E. Abrahams and J. Woo, "Phenomenological theory of the rounding of the resistive transition of superconductors," *Physics Letters A*, vol. 27, pp. 117–118, Jun 1968.

[24] K. Maki, "Critical fluctuation of the order parameter in a superconductor. I," *Progress of Theoretical Physics*, vol. 40(2), pp. 193–200, 1968.

[25] R. Thompson, "Microwave, flux flow, and fluctuation resistance of dirty type-II superconductors," *Physical Review B*, vol. 1, no. 1, pp. 327–333, 1970.

[26] W. Göb, "Magnetotransport-Effekte und Fluktuationen im sauerstoffreduzierten Hochtemperatursupraleiter $YBa_2Cu_3O_{7-\delta}$," Master's thesis, Universität Wien, 1997.

[27] W. Lang, "Influence of a distribution of critical temperatures on the paraconductivity and the fluctuation magnetoconductivity in high-temperature superconductors," *Physica C (Amsterdam, Neth.)*, vol. 226, pp. 267–278, 1994.

[28] E. Abrahams, R. Prange, and M. Stephen, "Effect of a magnetic field on fluctuations above T_c," *Physica*, vol. 55(C), pp. 230–233, October 1971.

[29] B. Serin, R. Smith, and T. Mizusaki, "Fluctuation effects in the conductivity of lead films," *Physica*, vol. 55, pp. 224–229, October 1971.

[30] C. Sekirnjak, W. Lang, S. Proyer, and P. Schwab, "Novel approach for the analysis of the fluctuation magnetoconductivity in $YBa_2Cu_3O_7$ thin films," *Physica C*, vol. 243, pp. 60–68, 1995.

[31] L. R. Testardi, "Destruction of superconductivity by laser light," *Phys. Rev. B*, vol. 4, pp. 2189–2196, Oct 1971.

[32] C. S. Owen and D. J. Scalapino, "Superconducting state under the influence of external dynamic pair breaking," *Phys. Rev. Lett.*, vol. 28, pp. 1559–1561, Jun 1972.

[33] A. M. Kadin and M. W. Johnson, "Nonequilibrium photon-induced hotspot: A new mechanism for photodetection in ultrathin metallic films," *Applied Physics Letters*, vol. 69, no. 25, pp. 3938–3940, 1996.

[34] A. D. Semenov, G. N. Gol'tsman, and A. A. Korneev, "Quantum detection by current carrying superconducting film," *Physica C: Superconductivity*, vol. 351, pp. 349–356, Apr 2001.

[35] J. Yang, A. Kerman, E. Dauler, V. Anant, K. Rosfjord, and K. Berggren, "Modeling the electrical and thermal response of superconducting nanowire single-photon detectors," *IEEE Transactions on Applied Superconductivity*, vol. 17, pp. 581–585, Jun 2007.

[36] G. N. Gol'tsman, O. Okunev, G. Chulkova, A. Lipatov, A. Semenov, K. Smirnov, B. Voronov, A. Dzardanov, C. Williams, and Roman Sobolewski, "Picosecond superconducting single-photon optical detector," *Applied Physics Letters*, vol. 79, no. 6, pp. 705–707, 2001.

[37] C. M. Natarajan, M. G. Tanner, and R. H. Hadfield, "Superconducting nanowire single-photon detectors: physics and applications," *Supercond. Sci. Technol.*, vol. 25, p. 063001, Apr 2012.

[38] J. J. Renema, R. Gaudio, Q. Wang, Z. Zhou, A. Gaggero, F. Mattioli, R. Leoni, D. Sahin, M. J. A. de Dood, A. Fiore, and M. P. van Exter, "Experimental test of theories of the detection mechanism in a nanowire superconducting single photon detector," *Phys. Rev. Lett.*, vol. 112, p. 117604, Mar 2014.

[39] A. Engel, A. Semenov, H.-W. Hübers, K. Il'in, and M. Siegel, "Fluctuation effects in superconducting nanostrips," *Physica C: Superconductivity and its Applications*, vol. 444, pp. 12–18, Sep 2006.

[40] M. Hofherr, D. Rall, K. Ilin, M. Siegel, A. Semenov, H.-W. Hübers, and N. A. Gippius, "Intrinsic detection efficiency of superconducting nanowire single-photon detectors with different thicknesses," *Journal of Applied Physics*, vol. 108, no. 1, pp. –, 2010.

[41] A. D. Semenov, P. Haas, H.-W. Hübers, H.bers, K. Ilin, M. Siegel, A. Kirste, T. Schurig, and A. Engel, "Vortex-based single-photon response in nanostructured superconducting detectors," *Physica C: Superconductivity and its Applications*, vol. 468, pp. 627–630, Apr 2008. (DOI: http://dx.doi.org/10.1016/j.physc.2007.11.028).

[42] H. A. Atikian, B. G. Ghamsari, S. M. Anlage, and A. H. Majedi, "Ultrafast linear kinetic inductive photoresponse of $YBa_2Cu_3O_{7-\delta}$ meander-line structures by photoimpedance measurements," *Applied Physics Letters*, vol. 98, Feb 2011.

[43] G. P. Pepe, D. Pan, V. Pagliarulo, L. Parlato, N. Marrocco, C. D. Lisio, G. Peluso, A. Brone, U. Scotti di Uccio, A. Casaburi, F. Tafuri, M. Khafizov, T. Taneda, and Roman Sobolewski, "Ultrafast photoresponse of superconductor/ferromagnet nano-layered hybrids," *IEEE Transactions on Applied Superconductivity*, vol. 19, pp. 376–381, June 2009. (DOI: 10.1109/TASC.2009.2018251).

[44] A. J. Kerman, E. A. Dauler, W. E. Keicher, J. K. W. Yang, K. K. Berggren, G. Gol'tsman, and B. Voronov, "Kinetic-inductance-limited reset time of superconducting nanowire photon counters," *Applied Physics Letters*, vol. 88, no. 11, p. 111116, 2006.

[45] A. Engel, A. Semenov, H.-W. Hübers, K. Il'in, and M. Siegel, "Fluctuations and dark count rates in superconducting NbN single-photon detectors," *Physica status solidi (c)*, vol. 2, no. 5, pp. 1668–1673, 2005.

[46] J. E. Mooij and Y. V. Nazarov, "Superconducting nanowires as quantum phase-slip junctions," *Nature Physics*, vol. 2, no. 3, pp. 169–172, 2006.

[47] A. Bezryadin, "Quantum suppression of superconductivity in nanowires," *J. Phys.: Condens. Matter*, vol. 20, p. 043202, Jan 2008.

[48] H. Bartolf, A. Engel, A. Schilling, K. Il'in, M. Siegel, H.-W. Hübers, and A. Semenov, "Current-assisted thermally activated flux liberation in ultrathin nanopatterned NbN superconducting meander structures," *Physical Review B*, vol. 81, p. 024502, Jan 2010.

[49] L. You, X. Yang, Y. He, W. Zhang, D. Liu, W. Zhang, L. Zhang, L. Zhang, X. Liu, S. Chen, Z. Wang, and X. Xie, "Jitter analysis of a superconducting nanowire single photon detector," *AIP Advances*, vol. 3, no. 7, 2013.

[50] K. Inderbitzin, A. Engel, A. Schilling, K. Il'in, and M. Siegel, "An ultra-fast superconducting Nb nanowire single-photon detector for soft x-rays," *Applied Physics Letters*, vol. 101, 162601, p. 162601, 2012.

[51] A. Verevkin, J. Zhang, Roman Sobolewski, A. Lipatov, O. Okunev, G. Chulkova, A. Korneev, K. Smirnov, G. N. Gol'tsman, and A. Semenov, "Detection efficiency of large-active-area NbN single-photon superconducting detectors in the ultraviolet to near-infrared range," *Applied Physics Letters*, vol. 80, no. 25, p. 4687, 2002.

[52] M. Ejrnaes, R. Cristiano, O. Quaranta, S. Pagano, A. Gaggero, F. Mattioli, R. Leoni, B. Voronov, and G. Gol'tsman, "A cascade switching superconducting single photon detector," *Applied Physics Letters*, vol. 91, no. 26, pp. –, 2007.

[53] A. Engel, A. Aeschbacher, K. Inderbitzin, A. Schilling, K. Il'in, M. Hofherr, M. Siegel, A. Semenov, and H.-W. Hübers, "Tantalum nitride superconducting single-photon detectors with low cut-off energy," *Applied Physics Letters*, vol. 100, no. 6, p. 062601, 2012.

[54] N. Marrocco, G. P. Pepe, A. Capretti, L. Parlato, V. Pagliarulo, G. Peluso, A. Barone, R. Cristiano, M. Ejrnaes, A. Casaburi, N. Kashiwazaki, T. Taino, H. Myoren, and Roman Sobolewski, "Strong critical current density enhancement in NiCu/NbN superconducting nanostripes for optical detection," *Applied Physics Letters*, vol. 97, no. 9, 2010. (DOI: http://dx.doi.org/10.1063/1.3479529).

[55] U. Nasti, L. Parlato, M. Ejrnaes, R. Cristiano, T. Taino, H. Myoren, Roman Sobolewski, and G. Pepe, "Thermal fluctuations in superconductor/ferromagnet nanostripes," *Physical Review B*, vol. 92, p. 014501, Jul 2015.

[56] W. H. Umrath, R. M. Bahnen, and K. Leybold Vakuum GmbH, *Grundlagen der Vakuumtechnik*. Köln: Leybold Vakuum, 08/2002 ed., 2002.

[57] A. Klimov, R. Puźniak, B. Aichner, W. Lang, E. Joon, R. Stern, W. Słysz, M. Guziewicz, M. Juchniewicz, M. A. Borysiewicz, R. Kruszka, M. Wegrzecki, A. Łaszcz, A. Czerwinski, and Roman Sobolewski, "Superconducting and ferromagnetic properties of NbN/NiCu and NbTiN/NiCu bilayer nanostructures for photon detection," *Proc. SPIE, Photon Counting Applications 2015*, vol. 9504, pp. 950405–950405–10, May 2015. (DOI: 10.1117/12.2179697).

[58] M. Guziewicz, W. Słysz, M. A. Borysiewicz, R. Kruszka, Z. Sidor, M. Juchniewicz, K. Golaszewska, Z. Domagala, Jaroslaw, W. Rzodkiewicz, J. Ratajczak, J. Bar, M. Wegrzecki, and Roman Sobolewski, "Technology of Ultrathin NbN and NbTiN Films for Superconducting Photodetectors," *Acta Physica Polonica, A*, vol. 120, no. 6-A, pp. 76–79, 2011.

[59] W. Słysz, M. Guziewicz, M. Borysiewicz, Z. Domagała, Jaroslaw, I. Pasternak, K. Hejduk, W. Rzodkiewicz, J. Ratajczak, J. Bar, M. Wegrzecki, P. Grabiec, R. Grodecki, I. Wegrzecka, and Roman Sobolewski, "Ultrathin NbN Films for Superconducting Single-Photon Detectors," *Acta Physica Polonica, A*, vol. 120, no. 1, pp. 200–203, 2011.

[60] A. I. Buzdin, "Proximity effects in superconductor-ferromagnet heterostructures," *Rev. Mod. Phys.*, vol. 77, pp. 935–976, Sep 2005.

[61] T. Taneda, G. P. Pepe, L. Parlato, A. A. Golubov, and Roman Sobolewski, "Time-resolved carrier dynamics and electron-phonon coupling strength in proximized weak ferromagnet-superconductor nanobilayers," *Physical Review B*, vol. 75, p. 174507, May 2007.

[62] I. S. Veshchunov, V. A. Oboznov, A. N. Rossolenko, A. S. Prokofiev, L. Y. Vinnikov, A. Y. Rusanov, and D. V. Matveev, "Observation of the magnetic domain structure in $Cu_{0.47}Ni_{0.53}$ thin films at low temperatures," *JETP Letters*, vol. 88, pp. 758–761, Feb 2008.

[63] K. Berggren, "kinetic inductance explained." YouTube, January 2011. https://www.youtube.com/watch?v=MAHkYROmriY; Accessed: 21-07-2015.

[64] A. J. Annunziata, D. F. Santavicca, L. Frunzio, G. Catelani, M. J. Rooks, A. Frydman, and D. E. Prober, "Tunable superconducting nanoinductors," *Nanotechnology*, vol. 21, p. 445202, Oct 2010.

[65] A. Engel, A. Semenov, H. Hübers, H. W. Wbers, K. Il'in, and M. Siegel, "Superconducting single-photon detector for the visible and infrared spectral range," *Journal of Modern Optics*, vol. 51, pp. 1459–1466, Jun 2004.

Explanation of the Abbreviations

Abra	Abrahams et al.
AL	Aslamazov-Larkin
BCS	Bardeen-Cooper-Schrieffer
DCR	Dark Count Rate (of an SSPD)
DDE	Device Detection Efficiency
F	Ferromagnet
GF	Geometry Factor ($GF = wd/l \cdot KF$ with w width, d thickness and l length of a stripe)
GL	Ginzburg-Landau
IV	current-Voltage
KF	correction Factor
MT	Maki-Thompson
RTA	Rapid Thermal Annealing
S	Superconductor
SDE	System Detection Efficiency
SEM	Scanning Electron Microscopy
SSPD	Superconducting single photon detector
TEM	Transmission Electron Microscopy
VAP	Vortex-Antivortex-Pair
VH	Vortex-Hopping